

**UCC Library and UCC researchers have made this item openly available.
Please [let us know](#) how this has helped you. Thanks!**

Title	Theory of the electronic and optical properties of germanium-tin alloys
Author(s)	O'Halloran, Edmond J.
Publication date	2020-04-22
Original citation	O'Halloran, E. J. 2020. Theory of the electronic and optical properties of germanium-tin alloys. PhD Thesis, University College Cork.
Type of publication	Doctoral thesis
Rights	© 2020, Edmond J. O'Halloran. https://creativecommons.org/licenses/by-nc-nd/4.0/
Item downloaded from	http://hdl.handle.net/10468/10024

Downloaded on 2021-11-27T12:20:40Z



UCC

University College Cork, Ireland
Coláiste na hOllscoile Corcaigh

Theory of the electronic and optical properties of germanium-tin alloys

Edmond James O'Halloran



Thesis submitted in partial fulfilment of the requirements
of the degree of Doctor of Philosophy

at the
School of Chemistry,
University College Cork,
National University of Ireland

Supervisor: Prof. Eoin P. O'Reilly
Head of Department: Dr. Humphrey Moynihan

April 2020

Contents

Declaration of Authorship	vii
Dedication	viii
Preface	ix
Acknowledgements	x
Abstract	xi
List of Publications	xiii
1 Introduction and overview	1
1.1 Background and Motivation	1
1.2 Group-IV alloys	2
1.3 Structure of the thesis and overview of primary results	4
2 Theoretical Methods	9
2.1 Electronic band structure	9
2.2 Density Functional Theory	11
2.2.1 Time independent Schrödinger Equation	12
2.2.2 Observables	12
2.2.3 Born-Oppenheimer approximation	13
2.2.4 Variational Principle	14
2.3 Kohn-Sham DFT	14
2.4 Exchange-correlation Functionals	16
2.4.1 Local density approximation	16
2.4.2 General Gradient Approximation	18
2.4.3 Modified Becke-Johnson approximation	18
2.4.4 Hybrid functionals	19
2.4.5 Heyd-Scuseria-Ernzerhof hybrid functionals	20
2.5 Pseudopotentials	21
2.5.1 Projector augmented-wave method	22
2.6 The Vienna ab initio Simulation Package	23
2.7 Band Unfolding	24
3 Experimental and theoretical investigation of GeSn alloys	27

3.1	Overview	27
3.2	Introduction	28
3.3	Experimental methods	31
3.3.1	Sample Fabrication	31
3.3.2	Experimental Setup	32
3.3.3	Surface Photovoltage	32
3.4	Theoretical Framework	32
3.4.1	Density Functional Theory	33
3.4.2	Hydrostatic pressure coefficients	34
3.5	Experimental Results	34
3.5.1	Sample synthesis	34
3.5.2	Absorption Coefficient and absorption edge	35
3.5.3	Pressure coefficients	37
3.6	Density Functional Theory analysis	38
3.6.1	Band structure calculations: Pressure dependence of band gap	38
3.6.2	Band structure calculations: Band mixing effects	41
3.6.2.1	Band structure calculations: Band mixing effects at low Sn contents	42
3.6.2.2	Band structure calculations: Band mixing effects at higher Sn contents	43
3.7	Chapter Summary	43
4	Electronic and optical properties of GeSn alloys	47
4.1	Overview	47
4.2	Theoretical Models	48
4.2.1	Summary of theoretical methods	48
4.2.2	First principles: hybrid functional and modified Becke-Johnson DFT	49
4.2.3	Semi-empirical: valence force field potential and tight-binding Hamiltonian	51
4.2.4	Primitive Ge, Sn and zincblende-GeSn DFT benchmarks	53
4.2.5	Choice of alloy supercells	53
4.2.6	Generation of special quasi-random structures	54
4.2.7	Hydrostatic pressure coefficients	55
4.3	Ordered and disordered alloy supercells	55
4.3.1	Summary of content	55
4.3.2	Structural relaxation - Alloy lattice constant	55
4.3.3	Internal relaxation: ordered supercells	57
4.3.4	Internal relaxation: disordered supercell	59
4.4	Supercell band structure	61
4.4.1	Band gap and spin-orbit splitting energy	61
4.4.2	Impact of Sn incorporation on conduction band structure	63
4.4.3	Sn-induced band mixing: band gap pressure coefficient	65
4.5	Impact of Sn local environment on germanium-tin alloy electronic structure	67
4.6	Disordered alloys: electronic structure evolution in germanium-tin special quasi-random structures	75
4.7	Conclusions	78
5	Electronic and optical properties of GePb alloys	81
5.1	Overview	81

5.1.1	Review of existing literature for GePb alloys	83
5.2	Theoretical models	83
5.2.1	Density Functional Theory	84
5.2.2	Choice of supercells	86
5.2.3	Special quasi random structures	86
5.3	Electronic properties of germanium-lead alloys	87
5.3.1	Conduction band structure and Pb-induced band mixing in ordered germanium-lead supercells	87
5.3.2	Impact of Pb local environment on germanium-lead alloy electronic structure	92
5.3.3	Disordered alloys: electronic structure evolution in germanium-lead special quasi-random structures	94
5.3.4	Comparison to electronic structure evolution in GeSn	98
5.4	Chapter Summary	100
6	Final Summation, conclusions, and outlook	103
6.1	Group-IV Optoelectronics	103
6.2	Optoelectronic properties of GeSn alloys	104
6.3	Outlook, ongoing work and future work	106
6.4	Optoelectronic properties of GePb alloys	107
6.4.1	Outlook, ongoing work and future work	108
	Bibliography	111

Declaration

I, Edmond James O'Halloran (student no. 110356185) hereby declare that, unless otherwise stated, this work is my own, and that it has not been submitted for another degree, either at University College Cork or elsewhere.

Signed:

Date:

For my parents

Preface

This thesis consists, for the most part, of a collection of manuscripts both published and unpublished, which have acted as the subject of my work as a PhD student in the Tyndall National Institute for the past 4 years from October 2015 until December 2019, under the supervision of Prof Eoin O'Reilly and Dr Stefan Schulz. In the formulation of this thesis the published papers have been revised and reformatted with minor corrections and alterations made with respect to the journal versions including the replotting of some of the figures, restructuring of the sections of text, etc., as appropriate to bring those papers in line with the thesis layout, but remain in content basically the same.

The unpublished manuscripts have been included in a format more appropriate for a work of this kind than for a final journal paper, and will likely undergo further modifications that are normal to the peer-reviewing process.

In addition to the research chapters, this thesis also contains the standard introductory chapter, Chapter 1, where the work is motivated and outlined, a theoretical methods chapter, Chapter 2, which provides a basic introduction to some of the fundamental theory and techniques utilised in this work but not appropriate to include within individual chapters and a conclusions chapter, Chapter 6, where I attempt to detail the relevance of the work and to outline the important results, and future avenues of study which relate to this project.

At the beginning of each chapter there is a short abstract in the style of journal papers which summarises the contents of the chapter and acts to preface the work contained therein. An overall outline of the thesis layout is given at the end of the introduction in Chapter 1.

Acknowledgements

I would like to begin by thanking all of the members, past and present, of the Photonics Theory Group (PTG) at Tyndall National Institute. It has been a pleasure to work with them over the past 4 years. I have learned so much from them over my four years in with the group. I wish all of them the best of luck in their future endeavours.

I thank my collaborators both within the Photonics Theory group at Tyndall and externally with Prof. Stephen Sweeney and Dr. Tim Eales from the University of Surrey whose expertise I benefited immensely from and who contributed experimental evidence for the evolution of the germanium- tin band gap under hydrostatic pressure.

I thank Science Foundation Ireland for providing the funding which supported this research, under the project 14/IA/2513, Physics of Novel SiGeSn Alloys.

I thank the members of my thesis committee, Prof. Stephen Fahy and Prof. Justin Holmes, for their efforts in reviewing my progress throughout my studies and for providing helpful feedback on my work at various stages. Similarly, I thank my examiners, both internal and external, for taking time out of their busy schedules to read and examine this thesis.

I would like to thank also my friends and family for their constant support and encouragement throughout my research. In particular I'd like to thank my parents, Michael and Ursula, for always supporting me in my studies and instilling in me from an early age the value of perseverance and hard work and my partner Ciara for her love, support and patience over the past four years. Thank also is due to my aunt Geraldine and grandaunt Shiela both for their support and encouragement, and for all of the tasty meals and lively conversations I enjoyed with them over the course of my research.

Finally, I would like to express my sincere thanks to my supervisor, Prof. Eoin O'Reilly for his guidance and patience throughout the duration of my research. I have benefited greatly from working with Eoin, both directly through his instruction and indirectly through his influence. I hope that my contribution to the ongoing research programme of the Photonics Theory Group has justified the trust he placed in me in taking me on as a research student.

Abstract

The key aim of silicon (Si) photonics is the development of photonic components which are compatible with established complementary metal-oxide semiconductor (CMOS) processing infrastructure, to deliver step-changes in device performance and capabilities, either via on-chip integration with microelectronics or by facilitating optical interconnection between optoelectronic chips. While significant progress has been made in the development of passive photonic components such as waveguides and modulators, the development of Si photonics is currently limited by the lack of direct-gap materials suitable for application as CMOS-compatible semiconductor lasers and light-emitting diodes.

While elemental group-IV semiconductors silicon and germanium (Ge) form a mainstay of current microelectronics, their indirect band gaps makes them intrinsically inefficient emitters and absorbers of light. The alloying of germanium with other group IV elementary materials such as carbon, tin or lead, holds the potential to bring about a direct band gap, in a material which can be grown directly on silicon substrates, and would allow for the realization of active Si-based components such as light emitting diodes and lasers.

Due primarily to the small difference of ≈ 150 meV between the indirect (fundamental) L_{6c} - Γ_{8v} and direct Γ_{7c} - Γ_{8v} band gaps of Ge, there has recently been a strong surge of interest in engineering the conduction band (CB) structure of Ge via strain or alloying in order to bring about a direct fundamental band gap. Much of this attention has focused on $\text{Ge}_{1-x}\text{Sn}_x$ alloys, where it has been predicted that incorporation of 6 – 11% Sn is sufficient to bring about a direct band gap. Experimental confirmation of the emergence of a direct band gap in $\text{Ge}_{1-x}\text{Sn}_x$ – culminating in initial demonstrations of optically and electrically pumped lasing - has stimulated more intense interest in this alloy. In addition to applications in CMOS-compatible light-emitting devices, research interest in (Si) $\text{Ge}_{1-x}\text{Sn}_x$ alloys has been driven by potential applications in tunneling field-effect transistors and in multi-junction solar cells.

In this thesis we use density functional theory calculations in the Vienna Ab-initio Simulation Package framework to investigate the mechanism by which the Ge band structure evolves from indirect to direct gap with the addition of small quantities of Sn to the alloy. By investigating a series of ordered and disordered supercells with varying % Sn contents we attempt to quantify band mixing and ordering effects in such alloys and the implications they hold for the materials optical and transport properties. Through these calculations we explicitly demonstrate that Sn atoms act when incorporated in small % quantities to germanium strongly perturb the electronic structure of the alloy conduction band while having a much lesser impact on the valence band structure of the alloy. We identify and quantify the mechanism by which the germanium band structure evolves from indirect to direct gap with the addition of small %

quantities of Sn to the alloy. Our analysis is reinforced by detailed comparisons to the results of experimental measurements.

From these density functional calculations a tight-Binding model has been parameterised allowing for extension of the investigation of the alloy supercells from the order of 10^3 atoms up to scales of $10^5 - 10^6$ atoms and providing a multiscale modelling approach which is ideally suited to the study of the electronic and optical properties of these $\text{Ge}_{1-x}\text{Sn}_x$ alloys

Finally in the latter part of this thesis we utilise the models which were developed in the investigation of GeSn alloys to investigate the electronic and optical properties and mixing effects of another less explored Group-IV alloy $\text{Ge}_{1-x}\text{Pb}_x$, from which we deduce a transition to direct gap emission for $x \approx 3 - 4 \%$.

Publications

The following is a list of published work in which aspects of the research presented in this thesis have featured.

1. Refereed journal articles

- “Comparison of first principles and semi-empirical models of the structural and electronic properties of $\text{Ge}_{1-x}\text{Sn}_x$ alloys”, Edmond J. O’Halloran, Christopher A. Broderick, Daniel S. P. Tanner, S. Schulz and E. P. O’Reilly, Optical and Quantum Electronics 51 (9), pg. 314 (2019)
- “First principles analysis of electronic structure evolution and the indirect- to direct-gap transition in $\text{Ge}_{1-x}\text{Pb}_x$ group-IV alloys”, Christopher A. Broderick, Edmond J. O’Halloran and Eoin P. O’Reilly, arXiv: 1911.05679 (2019) Submitted to Phys. Rev. Materials
- “ $\text{Ge}_{1-x}\text{Sn}_x$ alloys: Consequences of band mixing effects for the evolution of the band gap Γ -character with Sn concentration”, Tim D. Eales, Igor Marko, Stefan Schulz, Edmond J. O’Halloran, Seyed A. Ghetmiri, Wei Du, Yiyin Zhou, Shui-Qing Yu, Joe Margetis, John Tolle, Eoin P. O’Reilly and Stephen J. Sweeney, Scientific Reports, 9, Article number: 14077 (2019)

2. Conference proceedings

- “Comparative analysis of electronic structure evolution in GeSn and GePb alloys”, Christopher A. Broderick, Edmond J. O’Halloran and Eoin P. O’Reilly, Proceedings of the 19th International Conference on Numerical Simulation of Optoelectronic Devices (NUSOD), Ottawa, Canada pg. 117-118 (2019) DOI: 10.1109/NUSOD.2019.8806886
- “Multi-Scale Electronic Structure Analysis of Direct-Gap Group-IV Alloys: Implications for Device Applications”, Christopher A. Broderick, Edmond J. O’Halloran, Amy C. Kirwan, Michael D. Dunne, Daniel S P. Tanner, Stefan Schulz, and Eoin P. O’Reilly; Proceedings of IEEE International Conference on Group IV Photonics, Singapore, (2019) DOI: 10.1109/GROUP4.2019.8925787
- “Towards Direct Gap Emission in $\text{Ge}_{1-x}\text{Sn}_x$ and $\text{Ge}_{1-x}\text{C}_{1-x}$: a Hybrid Functional DFT Analysis”, Amy C. Kirwan, Edmond J. O’Halloran, Christopher A. Broderick, Stefan Schulz and Eoin P. O’Reilly, Proceedings of the 18th International Conference on Nanotechnology (IEEE Nano 2018), Cork, Ireland (2018) DOI: 10.1109/NANO.2018.8626242
- “The nature of the band gap of GeSn alloys”, Stefan Schulz, Christopher A. Broderick, Edmond J. O’Halloran and Eoin P. O’Reilly, Proceedings of the International Conference on Numerical Simulation of Optoelectronic Devices (NUSOD), pg 39-40 (2018) DOI: 10.1109/nusod.2018.8570230
- “Atomistic analysis of localisation and band mixing effects in $\text{Ge}_{1-x}(\text{C},\text{Sn})_x$ group-IV alloys”, Christopher A. Broderick, Michael D. Dunne, Daniel S. P. Tanner, Amy C. Kirwan, Edmond J. O’Halloran, Stefan Schulz, and Eoin P. O’Reilly, Proceedings of IEEE 18th International Conference on Nanotechnology (IEEE Nano 2018), Cork, Ireland (2018) DOI: 10.1109/nano.2018.8626255
- “New experimental evidence for nature of the band gap of GeSn alloys”, Timothy D. Eales, Igor P. Marko, Seyed A. Ghetmiri, Wei Du, Yiyin Zhou, Shui-Qing Yu, Joe Margetis, John Tolle, Stefan Schulz, Edmond J. O’Halloran, Eoin P. O’Reilly, and Stephen J. Sweeney, Proceedings of the SPIE Photonics West, Silicon Photonics XII, 101080F San Francisco, California, United States (2017) DOI: <https://doi.org/10.1117/12.2252724>

3. Conference talks

During the course of my doctoral research I have personally presented the following conference talks:

- “Theory of the electronic structure of direct-gap $\text{Ge}_{1-x}(\text{Sn,Pb})_x$ group-IV alloys”, [Edmond J. O’Halloran](#), Christopher A. Broderick and Eoin P. O’Reilly; [UK Semiconductors](#), Sheffield Hallam University, Sheffield, England (2019)
- “Direct band gaps from GeSn alloys: A hybrid functional DFT based analysis”, [Edmond J. O’Halloran](#), Stefan Schulz and Eoin P. O’Reilly; [Photonics Ireland](#), NUI Galway, Galway, Ireland (2017)

In addition to these talks I have also contributed to, and have had aspects of my work presented in the following conference talks, which were presented by my colleagues and collaborators:

- “Theory of the electronic structure of direct-gap $\text{Ge}_{1-x}(\text{C,Sn})_x$ group-IV alloys”, Christopher A. Broderick, Michael D. Dunne, Daniel S. P. Tanner, [Edmond J. O’Halloran](#), Amy C. Kirwan, Stefan Schulz, and Eoin P. O’Reilly; [UK Semiconductors](#), Sheffield Hallam University, Sheffield, England (2019)
- “Group-IV semiconductor alloys: electronic structure evolution and the indirect- to direct-gap transition”, Christopher A. Broderick, [Edmond J. O’Halloran](#), Michael D. Dunne, Amy C. Kirwan, Daniel S. P. Tanner, Stefan Schulz and Eoin P. O’Reilly; [10th International Workshop on Bismuth-Containing Semiconductors](#), LAAS, Toulouse, France, (2019)
- “Towards direct-gap emission in $\text{Ge}_{1-x}\text{Sn}_x$ and $\text{Ge}_{1-x}\text{C}_x$: a hybrid density functional theory analysis”, Amy C. Kirwan, [Edmond J. O’Halloran](#), Christopher A. Broderick, Stefan Schulz, and Eoin P. O’Reilly; [IEEE Nano 2018](#), University College Cork, Ireland, (2018)
- “Theory of localisation and band mixing effects in direct-gap $\text{Ge}_{1-x}(\text{C,Sn})_x$ group-IV alloys”, Christopher A. Broderick, Michael D. Dunne, Daniel S. P. Tanner, [Edmond J. O’Halloran](#), Amy C. Kirwan, Stefan Schulz, and Eoin P. O’Reilly; [IEEE Nano 2018](#), University College Cork, Ireland, (2018)
- “The nature of the band gap of GeSn alloys”, Stefan Schulz, Christopher A. Broderick, [Edmond J. O’Halloran](#), and Eoin P. O’Reilly; [NUSOD: 18th International Conference on Simulation of Optoelectronic Devices](#), University of Hong Kong, (2018)

- “Band Mixing and Localization Effects in Semiconductor Alloys”, E.P. O’Reilly, C.A. Broderick, S. Schulz, M.A. Caro, D. Tanner, Edmond J. O’Halloran and A. Kirwan; 8th International Workshop on Bismuth-Containing Semiconductors, University of Marburg, Germany (2017)

4. Conference posters

During the course of my doctoral research I have personally presented the following conference posters:

- “Band Mixing and Disorder Effects in $\text{Ge}_{1-x}(\text{C},\text{Sn},\text{Pb})_x$ Alloys”, Edmond J. O’Halloran, Christopher A. Broderick, Amy C. Kirwan and Eoin P. O’Reilly, Spring Meeting of the European Materials Research Society (E-MRS), Nice, France, (2019)
- “Direct band gaps from GeSn alloys: A hybrid functional density functional theory based analysis”, Edmond J. O’Halloran, Stefan Schulz and Eoin P. O’Reilly; Euro-TMCS II, University College Cork, Cork, Ireland, 2016
- “The role of localisation and band mixing effects in direct-gap $\text{Ge}_{1-x}(\text{C},\text{Sn})_x$ group-IV alloys”, Christopher A. Broderick, Michael D. Dunne, Amy C. Kirwan, Edmond J. O’Halloran, Daniel S. P. Tanner, Stefan Schulz, and Eoin P. O’Reilly; 34th International Conference on the Physics of Semiconductors (ICPS), Montpellier, France, (2018)

In addition I have also contributed to, and have had aspects of my work presented, in the following conference posters, which were presented by my colleagues and collaborators:

- “Multi-scale electronic structure analysis of direct-gap group-IV alloys: implications for device applications”, Christopher A. Broderick, Edmond J. O’Halloran, Amy C. Kirwan, Michael D. Dunne, Daniel S. P. Tanner, Stefan Schulz, and Eoin P. O’Reilly; IEEE International Conference on Group IV Photonics, Singapore, (2019)
- “Indirect- to direct-gap transition in $\text{Ge}_{1-x}(\text{C},\text{Sn})_x$ semiconductor alloys: mechanisms and implications”, Christopher A. Broderick, Michael D. Dunne, Amy C. Kirwan, Edmond J. O’Halloran, Daniel S. P. Tanner, Stefan Schulz, and Eoin P. O’Reilly; IOP Photonics, Aston University, England, (2018)
- “Theory of the electronic structure of direct-gap $\text{Ge}_{1-x}(\text{C},\text{Sn})_x$ group-IV alloys”, Michael D. Dunne, Christopher A. Broderick, Daniel S. P. Tanner, Edmond J. O’Halloran, Amy C. Kirwan, Stefan Schulz, and Eoin P. O’Reilly, Photonics Ireland Cork, Ireland, (2018)

Chapter 1

Introduction and overview

In this introductory chapter we begin in Section 1.1 and 1.2 by giving a brief overview of the background of and motivation for our research on germanium-tin and related alloys. Following this, in Section 1.3 we outline the structure of the remaining chapters of this thesis, describing the content of those chapters and providing an overview of the primary results that have been achieved during the course of this work.

1.1 Background and Motivation

The worldwide consumption of data is growing exponentially, driven by an assortment of applications ranging from social and streaming media to cloud based computing and data storage as well as an ever expanding range of connected devices within the "Internet of Things". While these new services and technologies offer the means for people to connect and interact worldwide on an unprecedented level, the increased data usage comes with the expense of increased power consumption. In 2018 it was estimated that the world's data centres were consumed an estimated 198 TWh or $\approx 1\%$ of the global demand for electricity [1]. As data consumption continues to rise and new data centres are built to meet demand, this power consumption must be addressed. Additionally, other difficulties are beginning to arise from the increased data rates offered by new technologies which are now meeting or exceeding the limits of conventional interconnect technologies. The major limiting factor for conventional interconnects is that data transmission requires the system be charged and discharged, using up both time and energy. While the amount of energy consumed in a single cable may be quite small, such costs quickly begin to stack up in server farms where thousands of cables are connected across multiple devices. Keeping temperatures down in such systems is both a source of major expense and energy consumption ($\approx 40\%$ of total energy used in a data centre [2]), and originates from

this charging and discharging of wires. Many of these issues could be resolved or mitigated if cables and switches could be replaced with optical rather than electronic components.

The vast complementary metal-oxide-semiconductor framework, developed to support the silicon microelectronics industry offer unparalleled levels of fabrication complexity and high manufacturing volumes and yield. However the seamless integration of optoelectronics on to a silicon based platform remains one of the outstanding goals of photonics. Many of the passive components needed for optoelectronic integrated circuits have already been developed including avalanche photodiodes (APDs), modulators [3–8], waveguides [8–10], vertical couplers and wavelength-division multiplexers [11]. The development of silicon compatible active photonic components (including electrically pumped lasers and LEDs) however, remains a challenge. The development of active photonics components from silicon is hindered by the fundamentally indirect nature of the silicon band gap [12] which renders it a poor emitter and absorber of light. There have been multiple attempts to engineer the band gap of silicon to bring about a direct band gap including through defect engineering [13–16], through nanostructures including porous silicon [17, 18] and nanostructured crystalline silicon [19–22] and through Si and SiO₂ superlattices [23]. To date however, the output power and efficiency of active components developed from Si with these methods remains too low to meet the requirements of CMOS photonics.

Realisation of the vast potential of CMOS technologies therefore requires that new materials be developed. To leverage the advanced manufacturing infrastructure of existing CMOS technologies and to integrate monolithically with existing CMOS chipsets these new materials must be silicon compatible and feature a growth process that is compatible with the existing CMOS workflow.

1.2 Group-IV alloys

Given the requirement that new materials must be compatible with existing CMOS chipsets, the ideal solution would be to use materials which already exist within the CMOS workflow. As such there has in recent years been a growing interest in germanium and other group-IV elements which are already in wide usage in existing CMOS device workflows. The lattice parameters and band gaps of some of these group-IV elements are shown in Table 1.1. Of the group-IV elements Ge in particular is of note as it has been predicted to offer the benefit of significantly higher hole mobility than Si, and while Ge is an indirect band gap material, the direct band gap in Ge lies only ≈ 150 meV above the indirect conduction band minimum at L. As a result it is possible to engineer the band gap of Ge so as to bring about a direct gap in a material that is compatible with existing CMOS technologies. Recent research efforts on the band engineering of Ge to bring about a direct band gap have focused primarily on two

Element	a_0 (Å)	E_g^Γ (eV)	E_g^L (eV)
Si	5.431	4.20	1.12
Ge	5.648	0.89	0.74
α -Sn	6.489	-0.41	0.18

TABLE 1.1: Lattice constants and band gap energies for the group-IV elementary materials Si, Ge, α -Sn. Values of lattice constant and band gap for Si and Ge and lattice constant of α -Sn are from Ref. [32] while the band gap of α -Sn is taken from [33].

methods, the tensile straining of bulk Ge and the alloying of Ge with other group-IV elementary materials.

It has been reported that tensile straining of germanium reduces the energy of the Γ valley more rapidly than the L valley [24–28] and at sufficiently high strain brings about a fundamentally direct band gap semiconductor. Small amounts of biaxial tensile strain, as low as 0.25% tensile strain have been noted to decrease the energy difference between the Γ and L valleys compared to unstrained Ge, but are insufficient to bring about a fundamentally direct band gap [29]. To achieve a direct gap n-type doping is then used to compensate for the energy difference between the Γ and L valleys [25]. For high biaxial tensile strain of 2% or greater, theoretical calculations suggest that the band gap should transition from indirect to direct gap [26–28]. High tensile strain in Ge-on-Si materials has been demonstrated as a proof of concept using suspended Ge microstructures, which were grown through multi-step lithography [30, 31]. The low-throughput of the fabrication process and the complex device structure, have however made these materials difficult to use for practical applications. Finally while lasing has been reported for highly strained Ge, optical excitation is currently limited to cryogenic temperatures with heat dissipation in the material proving a particular challenge.

Alloying of Ge with other group IV elements such as tin (Sn) or lead (Pb) at sufficiently high levels, reduces the Γ valley below the L valley and holds the potential to bring about a tunable direct band gap, in a material which can be grown directly on silicon substrates [34, 35], and would allow for the realization of active Si-based components such as light emitting diodes and lasers. Significantly GeSn alloys also offer the potential to realise an efficient infrared light source on Si [25, 36, 37] with applications in optical interconnects [38] and lab-on-chip trace gas detection [39, 40].

Recent research efforts have suggested that incorporation of 6–11% Sn [41–44] or compositions of $\approx 3.5\%$ Pb [45] is sufficient to bring about a direct band gap. Experimental confirmation of the emergence of a direct band gap in $\text{Ge}_{1-x}\text{Sn}_x$ which culminated in initial demonstrations of optically and electrically pumped lasing [46–48] has stimulated more intense interest in this alloy. In addition to applications in CMOS-compatible light-emitting devices, research interest in (Si) $\text{Ge}_{1-x}\text{Sn}_x$ alloys has been driven by potential applications in tunneling field-effect transistors [49, 50] and in multi-junction solar cells [51].

1.3 Structure of the thesis and overview of primary results

The remainder of the thesis focuses on developing the theory of the electronic structure of the group-IV alloys germanium-tin, which is the focus of chapters 3 and 4, and germanium-lead alloys, which chapter 5 is focused on, using ab-initio density functional theory methods. In Chapter 2 of this thesis we detail and develop the relevant theoretical background for the work that follows in the remaining chapters. This background primarily focuses on developing the fundamental theoretical framework for density functional theory including detailed descriptions of the functionals which are utilised in later chapters to simulate the electronic band structures of group-IV alloys. Also included in Chapter 2 are details of the fundamental theory of electronic band structure and relevant fundamental theory relating to group-IV optoelectronics.

The investigation of the electronic optical and material properties of germanium tin alloys begins in Chapter 3 where we develop the theory of the electronic structure of $\text{Ge}_{1-x}\text{Sn}_x$ alloys and provide an investigation of the implications of band mixing effects on the evolution of the electronic band structure of $\text{Ge}_{1-x}\text{Sn}_x$ alloys with increasing Sn composition using a series of ab-initio density functional theory calculations. Recent theoretical and experimental investigations of $\text{Ge}_{1-x}\text{Sn}_x$ alloys have indicated that incorporation of Sn into bulk Ge causes a strong reduction in the direct band gap of the alloy, bringing about an indirect to direct band gap transition for $\approx 10\%$ Sn content [52]. Existing literature would suggest that this transition from an indirect to a direct band gap in $\text{Ge}_{1-x}\text{Sn}_x$ alloys should be sharp in nature. This is to say that up to a certain critical composition of Sn the band gap will be purely indirect (L-like) in nature, while at this critical Sn composition and above it the band gap will be purely direct (Γ -like) in nature.

In Chapter 3 we challenge this existing assertion of the nature of the band gap transition in $\text{Ge}_{1-x}\text{Sn}_x$ alloys, using a combination of experimental photovoltage measurements carried out by collaborators on a series of $\text{Ge}_{1-x}\text{Sn}_x$ photodiodes of varying compositions of x between 0 and 10% and a theoretical density functional theory (DFT) based investigation of the alloy electronic band structure. Rather than a sharp transition from an indirect to a direct band gap, results from experimental photovoltage measurements and theoretical hydrostatic pressure calculations of the electronic alloy band structure indicate a continuous evolution of Γ character at the conduction band gap edge, as the band gap narrows as a function of Sn concentration. This monotonic increase of Γ character at the conduction band edge, whose pressure coefficient appears to asymptotically approach that of Γ in pure Ge, is indicative of band mixing effects in the alloy which have not generally been accounted for in the contemporary literature. This presence of band mixing effects in the alloy causes the distinction between direct and indirect band gaps to break down. As such, we conclude that simple models like the virtual crystal approximation (VCA), which neglects effects related to band mixing and alloy disorder are insufficient to accurately describe the electronic band structure of $\text{Ge}_{1-x}\text{Sn}_x$ alloys. Atomistic

calculations which explicitly account for the differences in size and chemical properties between Ge and Sn are required to provide quantitative insight into the properties of real $\text{Ge}_{1-x}\text{Sn}_x$ alloys.

Having performed a preliminary investigation of the band structure of $\text{Ge}_{1-x}\text{Sn}_x$ alloys in Chapter 3 with hybrid functional Heyd-Scuseria-Ernzerhof (HSE) DFT, we expand our investigation in chapter 4 using valence force field (VFF), modified Becke Johnson (mBJ) DFT and a tight binding (TB) model parameterised by collaborators. Using hybrid functional calculations as a reference, we quantify the accuracy of structural relaxations and electronic structure calculations carried out for a series of ordered and disordered $\text{Ge}_{1-x}\text{Sn}_x$ alloy supercells using the LDA + mBJ and VFF + TB models. Our results suggest that (i) Sn incorporation can be expected to primarily impact the CB structure in $\text{Ge}_{1-x}\text{Sn}_x$ alloys while leaving the valence band relatively unperturbed, (ii) the LDA + mBJ model offers first principles calculations of the alloy properties which are in good quantitative agreement with, and come at significantly reduced computational cost and time compared to HSEsol calculations, and (iii) the semi-empirical VFF + TB model offers an accurate and computationally inexpensive approach to calculate the structural and electronic properties, describing well the alloy electronic structure close in energy to the CB and valence band (VB) edges. That is, in the regions of the band structure which are typically of interest to calculate technologically relevant material properties such as optical transition strengths, carrier mobility and band-to-band tunneling rates.

VFF structural relaxations are found to be in excellent quantitative agreement with the results of full HSEsol calculations. This suggests that the valence force field potential can be used to circumvent the requirement to carry out first principles structural relaxations – i.e. the relaxed positions obtained from a VFF structural relaxation can be reliably used as input to first principles electronic structure calculations, thereby offering significant reductions in computational expense and time. For equivalent system sizes we typically find that the computational expense associated with mBJ calculations is reduced by approximately an order of magnitude compared to equivalent HSEsol calculations, while semi-empirical VFF + TB calculations come at negligible computational expense. mBJ calculations allow access to larger system sizes in first principles calculations than those accessible to HSEsol hybrid functional methods due to their reduced computational expense but are still limited in scope to systems containing $\lesssim 10^3$ atoms. The semi-empirical VFF + TB model parameterised from the HSEsol DFT is highly scalable, and can readily be extended to systems containing $\sim 10^5$ atoms, with potential applications including direct atomistic calculations of the electronic structure of disordered $\text{Ge}_{1-x}\text{Sn}_x$ alloys and realistically-sized nanostructures.

Having benchmarked the mBJ-DFT approach and ascertained its accuracy by comparison with HSEsol DFT, we turn our attention to the investigation of disordered alloy supercells and the impact of ordering of Sn atoms on the alloy electronic band structure. Investigations of the

electronic band structure of $\text{Ge}_{14}\text{Sn}_2$ ($x = 12.5\%$) and $\text{Ge}_{62}\text{Sn}_2$ ($x = 3.125\%$) supercells as Sn atoms are moved from fourth, to third, to second and finally to first nearest neighbour show the dependence of the calculated values of E_g and $\frac{dE_g}{dP}$ respectively on the relative position of the two Sn atoms to one another in the supercell. Overall the results indicate the important impact of disorder effects on the electronic band structure. We note that the impact of these effects is likely overestimated due to long range periodic ordering effects arising from the small size of the supercells investigated and so anticipate that as the supercell increases the impact of disorder effects will be lessened.

Finally having established the important role short-range Sn-related structural disorder plays in influencing the details of the alloy electronic structure for 16 and 64 atom supercells, we turn our attention to investigate how the electronic structure evolves with x in realistic, disordered $\text{Ge}_{1-x}\text{Sn}_x$ special quasi-random structures. Hydrostatic pressure calculations of 128 atoms SQS supercells with x varied between 0 and 15% indicate an uptake in Gamma character in the lowest conduction band state at compositions of $\approx 5.5\%$ Sn content. At this $\approx 5.5\%$ Sn content the pressure coefficient of the conduction band edge remains primarily composed of band character arising from the Ge L_{6c} states having strong s -like orbital character at the Sn lattice sites, but also contains an admixture of Ge Γ_{7c} character. The level of Gamma character in the conduction band edge pressure coefficient continues to increase monotonically with conduction band edge, becoming primarily Gamma-like at $\approx 7\%$ Sn, and continuing to increase until $\approx 10\%$ Sn content at which point the pressure coefficient begins to level off. The band gap at 7.% Sn, when the alloy is anticipated to become direct gap in nature has a value of $E_g = 0.499\text{eV}$ indicating that the alloy remains a semiconducting material at the point of indirect- to direct-gap transition.

Overall, our results indicate that electronic structure calculations for $\text{Ge}_{1-x}\text{Sn}_x$ alloys must explicitly include band mixing and disorder effects to allow for accurate analysis of the impact of Sn incorporation on key material parameters, including optical transition strengths, electron mobility and band-to-band tunneling rates. Given the expected importance of these effects in determining technologically relevant material properties, the development of appropriate theoretical models enable predictive theoretical analysis of proposed $\text{Ge}_{1-x}\text{Sn}_x$ -based photonic, electronic and photovoltaic devices. The theoretical models we have presented allow for the treatment of larger systems than those accessible to hybrid functional DFT with minimal loss of accuracy, providing a basis for direct atomistic calculations of the electronic, optical and transport properties of disordered $\text{Ge}_{1-x}\text{Sn}_x$ alloys and realistically-sized nanostructures.

Having investigated the optical and electronic properties of $\text{Ge}_{1-x}\text{Sn}_x$ alloys in chapter 3 and chapter 4, we shift our attention in chapter 5 to the investigation of another group-IV alloy $\text{Ge}_{1-x}\text{Pb}_x$. What little literature exists for $\text{Ge}_{1-x}\text{Pb}_x$ alloys suggests that incorporation of lead (Pb) into bulk Ge will cause a reduction of the direct band gap of Ge which is similar, but

more pronounced than that seen with equivalent % Sn incorporation. Using the HSE DFT and mBJ DFT models which we parameterised for $\text{Ge}_{1-x}\text{Sn}_x$ alloys in chapter 4 we investigate a series of ordered and disordered $\text{Ge}_{1-x}\text{Pb}_x$ alloy supercells which vary in size from 16 to 128 atoms. Beginning with ordered alloy supercells, we demonstrate that Pb incorporation in a $\text{Ge}_{15}\text{Pb}_1$ or $\text{Ge}_{63}\text{Pb}_1$ supercell split the degeneracy of the Ge L_{6c} CB edge states, giving rise to a (Kramers degenerate) singlet state, and to a (Kramers degenerate) triplet state lying slightly higher in energy, with these singlet and triplet states respectively having purely s - and p -like orbital character at the Pb lattice site. Calculated pressure coefficients demonstrate that this singlet state which emerges at the conduction band edge retains primarily indirect (Ge L_{6c}) character and so does not represent the emergence of a direct band gap for Pb compositions as low as $x = 1.56\%$.

This result supports the requirement for more detailed calculations on disordered supercells, both (i) to quantify the nature of the indirect- to direct-gap transition and (ii) seek to identify the composition x at which $\text{Ge}_{1-x}\text{Pb}_x$ becomes a direct-gap semiconductor. To quantify the impact of Pb-related alloy disorder we tracked the evolution of the alloy CB edge in a $\text{Ge}_{62}\text{Pb}_2$ supercell as the separation between the Pb atoms was reduced from fourth- to first-nearest neighbours. Substituting two Pb atoms at successively closer lattice sites, we find strong dependence of the alloy band gap and spin orbit splitting energy on the distance between the two Pb atoms. As a result, we determine that disorder effects must be explicitly considered to quantitatively analyse the alloy electronic structure, suggesting that as is the case for $\text{Ge}_{1-x}\text{Sn}_x$ alloys, simple models such as the VCA are ill-suited to accurate analysis of $\text{Ge}_{1-x}\text{Pb}_x$ alloys. Having established the importance of disorder effects in determining the details of the electronic properties, we then analyse the evolution from an indirect to a direct band gap with increasing x in the case of a randomly disordered alloy.

The calculated electronic structure evolution for disordered 128-atom $\text{Ge}_{128-M}\text{Pb}_M$ SQSs again showed a (Kramers degenerate) singlet state at the CB edge, for even the lowest Pb composition considered ($x = 0.78\%$). Calculated pressure coefficients associated with the band gaps between the VB edge and the five lowest energy (Kramers degenerate) CB states again show that the CB edge retained primarily Ge L_{6c} character until $x \approx 6 - 7\%$, at which composition the lowest energy CB state acquired predominantly direct (Ge Γ_{7c}) character. The SQS calculations therefore indicate an indirect- to direct-gap transition in $\text{Ge}_{1-x}\text{Pb}_x$ alloys for $x \approx 6 - 7\%$, near which composition the CB edge also passes through the VB edge, to give a zero-gap semimetallic alloy.

Accounting however for finite-size effects in the SQSs considered, evidenced by a large ≈ 150 meV splitting of the four Ge L_{6c} -derived states, which may lead to an overestimation of the composition at which $\text{Ge}_{1-x}\text{Pb}_x$ becomes direct-gap, our results indicate that the CB state with the greatest Ge Γ_{7c} character passes through the weighted average energy of the four

Ge_{6c} -derived states in our SQS calculations for $x \approx 3 - 4\%$. This weighted average may provide a more realistic estimate of the composition range in which $\text{Ge}_{1-x}\text{Pb}_x$ starts to become a direct-gap semiconductor, at which composition the calculated alloy band gap is in the range $0.3 - 0.4$ eV. Due to similarities in the impact of Pb and Sn incorporation on the Ge band structure, we then compare and contrast results of equivalent 128 atom SQS investigations of the $\text{Ge}_{1-x}(\text{Sn}/\text{Pb})_x$ alloy electronic band structure. In so doing we demonstrate that the electronic structure evolution in $\text{Ge}_{1-x}\text{Pb}_x$ admits important quantitative differences compared to that in $\text{Ge}_{1-x}\text{Sn}_x$.

In an overall sense results in this chapter indicate the emergence of a direct band gap in response to substitutional Pb incorporation in Ge, suggesting that binary $\text{Ge}_{1-x}\text{Pb}_x$ alloys are potentially of interest for applications as active photonic devices operating at mid-infrared wavelengths. However, the potential for application of $\text{Ge}_{1-x}\text{Pb}_x$ alloys in such devices may in practice be limited by the presence of a low fundamental band gap.

Finally in Chapter 6 we summarise and conclude. We recapitulate the main results and findings of the research presented in this thesis and provide an outlook of potential future research directions which arise from the work detailed in this thesis, pertaining to group-IV optoelectronics.

Chapter 2

Theoretical Methods

In this chapter we review and detail some of the fundamental principles and methodologies which underline the objectives and methodologies of the research presented in later chapters of this thesis. We begin in Section 2.1 by providing a general overview of the electronic band structure and its features including high symmetry points and the atomic band character of the conduction and valence bands. Then in Sections 2.2–2.4 we provide an overview of density functional theory. We first introduce the density functional in Sec. 2.2 and then Kohn-Sham theory in Sec. 2.3. Sec. 2.4 then provides details of a number of different functionals which will be employed throughout this thesis in the investigation of the electronic band structure and the optical and electronic properties of germanium based group – IV alloys. Section 2.5 provides a brief overview of pseudopotential methods, focusing primarily on the projector augmented-wave method which we will use in subsequent chapters. Finally in Sections 2.6 – 2.7 we provide a brief overview of the VASP and BandUP software packages which we use to investigate the electronic band structure of group-IV alloys in this thesis.

2.1 Electronic band structure

A major successes of quantum theory was its ability to explain the properties of bulk crystalline semiconducting materials. Bloch’s theorem [53] establishes that the wave function $\psi_{n\mathbf{k}}(\mathbf{r})$ for a bulk crystalline material can be expressed as the product of a plane wave and a function of the same periodicity as the lattice:

$$\psi_{n\mathbf{k}}(\mathbf{r}) = e^{i\mathbf{k}\cdot\mathbf{r}} u_{n\mathbf{k}}(\mathbf{r}), \quad (2.1)$$

where \mathbf{r} is the position, n is the n^{th} state associated with wavevector \mathbf{k} , $e^{i\mathbf{k}\cdot\mathbf{r}}$ is a phase factor which describes the extended nature of the state and $u_{n\mathbf{k}}$ denotes a periodic function of the same periodicity as the crystal:

$$u_{n\mathbf{k}}(\mathbf{r}) = u_{n\mathbf{k}}(\mathbf{r} + \mathbf{R}), \quad (2.2)$$

where \mathbf{R} is a Bravais lattice vector. Electron wave functions of the form in Eq. 2.1 are known as Bloch states. A full proof of Bloch's theorem can be found in Ashcroft and Mermin [54]. In cases which satisfy Bloch's theorem, as bulk crystalline materials do, any \mathbf{k} -state which possesses a wave vector which lies outside the first Brillouin zone can be translated back into the Brillouin zone by adding a suitable reciprocal lattice vector \mathbf{G} , so that all of the unique crystal Bloch states are located within the first Brillouin zone.

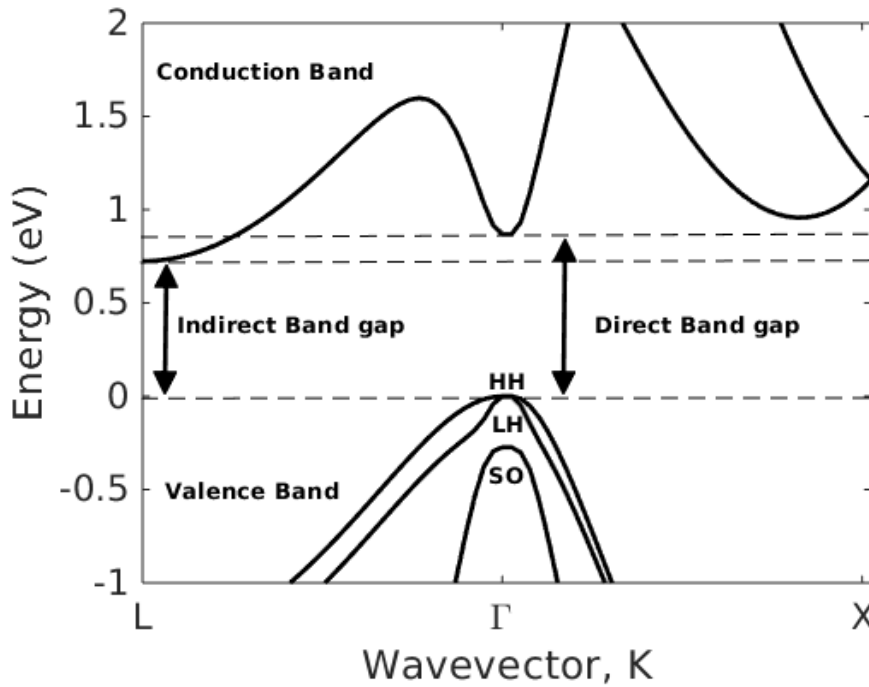


FIGURE 2.1: The band structure of bulk germanium (Ge) for states which are close in energy to the energy gap between the highest filled (valence) and lowest empty (conduction) bands, calculated using density functional theory methods. The zero of energy here is taken at the valence band edge.

Band theory indicates that in solids, electrons do not have discrete energy as is the case of free atoms, but rather have values of energy only within certain specific ranges known as allowed bands, which are separated by forbidden energy gaps. The behaviour of electrons in a solid relates closely to the position of the atoms surrounding it and the band of energies permitted in a solid is related to the discrete allowed energies (energy levels) of single, isolated atoms. In bringing the atoms together to form a solid, these discrete energy levels become perturbed, and the electrons occupy a band of levels in the solid called the valence band. The empty states

also broaden into a band of levels that is called the conduction band. Just as electrons at one energy level in an individual atom can move to higher empty energy levels, so too can electrons in a solid become excited and transfer from the valence band to the conduction band, crossing the intervening band gap. Using band theory, solids can be divided into three distinct groups (i) metals where the conduction and valence bands overlap, (ii) semiconductors which feature a small band gap which may be either indirect or direct in nature and (iii) insulators where the gap between the conduction and valence bands is quite large.

Returning to Bloch's theorem, we can associate a wavevector \mathbf{k} with each energy state $E_{n\mathbf{k}}$ of a periodic solid. If we then plot a diagram of these energies $E_{n\mathbf{k}}$ as a function of the wavevector \mathbf{k} we get the band structure of the solid.

Fig. 2.1 shows the band structure of bulk germanium and shows how energy bands may be represented in \mathbf{k} - (momentum) space, where \mathbf{k} relates both to the plane wave modulation in the Bloch equation and to the momentum of each state $\mathbf{p} = \hbar\mathbf{k}$, where \mathbf{p} is the momentum and \hbar is the reduced Planck's constant. The critical symmetry points of the conduction band shown in Fig. 2.1 at Γ , L and X represent $\mathbf{k} = [0, 0, 0]$, $[\frac{\pi}{a}, \frac{\pi}{a}, \frac{\pi}{a}]$ and $[\frac{2\pi}{a}, 0, 0]$ in \mathbf{k} -space respectively, where a denotes the lattice constant of bulk Ge [55].

As denoted in Fig 2.1 the valence band is split into three sub-bands near the valence band maximum, referred to as the heavy hole (HH) band, the light hole (LH) band and the spin-orbit split-off (SO) band. In an unstrained semiconductor the heavy hole and light hole bands will be degenerate and the spin-orbit split-off band will be separated from them by the spin-orbit splitting energy Δ_{SO} as a result of the spin-orbit interaction.

Throughout this thesis we will be concerned with calculations of the electronic band structure of group-IV elements and diamond structured semiconductor alloys formed from them, which are characterised by a fourfold tetrahedral coordination and sp^3 -hybridised covalent bonding. In the next section of this chapter we will demonstrate how the electronic band structure of these group-IV materials may be investigated.

2.2 Density Functional Theory

Density functional theory (DFT) is an extremely useful methodology which allows for computational quantitative calculation of many properties of materials in an ab initio manner, that is to say without experimental inputs. As such DFT methods allow for the modelling of materials that are either difficult to measure experimentally or for which no growth conditions have yet been developed. Due to the ab initio nature of DFT methods they may also be used to independently check and verify new experimental results in less developed material systems as we detail for $\text{Ge}_{1-x}\text{Pb}_x$ alloys in chapter 5 of this thesis.

2.2.1 Time independent Schrödinger Equation

Our goal in using DFT is to solve the time-independent Schrödinger equation to determine the total energy of a system:

$$\hat{H}|\Psi\rangle = E|\Psi\rangle, \quad (2.3)$$

where E is a constant equal to the energy level of the system. For a non-relativistic system of n interacting electrons and N nuclei, which are subject to a potential, the Hamiltonian operator can be expressed as:

$$\hat{H} = -\frac{\hbar^2}{2m} \sum_i^n \nabla_i^2 - \frac{1}{4\pi\epsilon_0} \sum_i^n \sum_I^N \frac{Z_I e^2}{|\mathbf{r}_i - \mathbf{R}_I|} + \frac{1}{8\pi\epsilon_0} \sum_i^n \sum_{j \neq i}^n \frac{e^2}{|\mathbf{r}_i - \mathbf{r}_j|} - \frac{\hbar^2}{2M_I} \sum_I^N \nabla_I^2 + \frac{1}{8\pi\epsilon_0} \sum_I^N \sum_{J \neq I}^N \frac{Z_I Z_J e^2}{|\mathbf{R}_I - \mathbf{R}_J|}, \quad (2.4)$$

where \hat{H} is the single electron Hamiltonian, m denotes the mass of an electron, M denotes the mass of the nucleus, Z is the charge of the nucleus expressed in units of the elementary charge e and \hbar is the reduced Planck's constant, with $\hbar = \frac{h}{2\pi}$. In this equation lower case i and j subscripts denote electrons while uppercase I and J are used to denote nuclei. Following Martin's example [56], the Hamiltonian can then be rewritten in the simpler form of:

$$\hat{H} = \hat{T} + \hat{V}_{ext} + \hat{V}_{int} + \hat{T}_{nuc} + E_{II}, \quad (2.5)$$

where in Eq. 2.5 the first term \hat{T} describes the kinetic energy of the electrons, the second term \hat{V}_{ext} describes the attractive electrostatic interaction between the nuclei and the electrons, the third term \hat{V}_{int} describes the repulsive potential due to the electron-electron interactions, the fourth term is the kinetic energy of the nuclei and the fifth term describes repulsive nucleus-nucleus interactions.

2.2.2 Observables

The time-independent expression for any observable of an eigenstate, is the expectation value of the operator \hat{O} , which involves an integral over all coordinates.

$$\langle \hat{O} \rangle = \frac{\langle \Psi | \hat{O} | \Psi \rangle}{\langle \Psi | \Psi \rangle} \quad (2.6)$$

By taking the expectation value of the density operator $\hat{n}(\mathbf{r})$ the density of particles $n(\mathbf{r})$, which is central to a lot of the theory of electronic band structure, can be obtained. Here $\hat{n}(\mathbf{r})$ is defined as:

$$\hat{n}(\mathbf{r}) = \sum_{I,N} \delta(\mathbf{r} - \mathbf{r}_i), \quad (2.7)$$

and so the density of particles is:

$$n(\mathbf{r}) = \frac{\langle \Psi | \hat{n}(\mathbf{r}) | \Psi \rangle}{\langle \Psi | \Psi \rangle} = N \frac{\int d^3r_2 \dots d^3r_N \sum |\Psi(\mathbf{r}_1, \mathbf{r}_2, \mathbf{r}_3, \dots, \mathbf{r}_N)|^2}{\int d^3r_1, d^3r_2 \dots d^3r_N |\Psi(\mathbf{r}_1, \mathbf{r}_2, \mathbf{r}_3, \dots, \mathbf{r}_N)|^2} \quad (2.8)$$

2.2.3 Born-Oppenheimer approximation

Using the Born–Oppenheimer or adiabatic approximation [57] we can approximate the mass of the nuclei relative to the mass of the electrons as being infinite. This results in the kinetic energy of the nuclei which is proportional to $\frac{1}{M_I}$ becoming zero. In effect we are saying that relative to the speed of the electrons the movement of the nuclei is negligible. Hence, we treat the electrons as moving in a field of fixed nuclei. In relation to Eq. 2.5 use of the Born–Oppenheimer approximation results in the the fourth term \hat{T}_{nuc} which describes the kinetic energy of the nuclei becoming zero and the fifth term E_{II} which describes repulsive nucleus–nucleus interactions becoming a constant term. As such the Hamiltonian of the system reduces to:

$$\hat{H} = \hat{T} + \hat{V}_{ext} + \hat{V}_{int} + E_{nuc} \quad (2.9)$$

The total energy of the system described in Eq. 2.9 can then be calculated as the expectation value of the Hamiltonian,

$$E = \frac{\langle \Psi | \hat{H} | \Psi \rangle}{\langle \Psi | \Psi \rangle} \equiv \langle \hat{H} \rangle = \langle \hat{T} \rangle + \langle \hat{V}_{int} \rangle + \int d\mathbf{r} V_{ext}(\mathbf{r}) n(\mathbf{r}) + E_{II}, \quad (2.10)$$

where $\langle \hat{T} \rangle$ is the kinetic energy of the electrons, \hat{V}_{int} is the potential energy due to the electron–nucleus interaction and the third term, the expectation value of V_{ext} which is the attractive external potential, has been written as an integral over the density function.

2.2.4 Variational Principle

The variational principle states that the total energy for a system calculated using a guessed wavefunction Ψ is an upper bound of the true ground-state energy of the system E_0 . The true ground state wavefunction Ψ_0 and energy E_0 of the system can then be calculated by fully minimizing the functional $E[\Psi]$ with respect to all allowed electron wave functions.

$$E_0 = \min_{\Psi} E[\Psi] = \min_{\Psi} \hat{T} + \langle \Psi | \hat{V}_{ext} + \hat{V}_{int} + E_{nuc} | \Psi \rangle \quad (2.11)$$

2.3 Kohn-Sham DFT

The primary objective of most of the rest of the calculation, is the solution of $\langle \hat{V}_{int} \rangle$. In classical mechanics this would be achieved by taking a space integral involving the electron charge density for the system. In the quantum picture however the quantum nature of electrons complicates solution of \hat{V}_{int} . In order to simplify the problem therefore we split $\langle \Psi | \hat{V}_{int} | \Psi \rangle$ into the sum of the classical electrostatic energy and the difference between the energies of the quantum-mechanical and classical electron-electron interactions, which we term the exchange-correlation energy. Denoting the electronic charge density $n(\mathbf{r})$ as:

$$n(\mathbf{r}) = |\psi(\mathbf{r})|^2, \quad (2.12)$$

the total energy can be expressed as a function of the integrals of the density as:

$$E = \langle \hat{T} \rangle + \int d\mathbf{r} V_{ext}(\mathbf{r})n(\mathbf{r}) + \underbrace{\frac{1}{8\pi\epsilon_0} \int \int d\mathbf{r} d\mathbf{r}' \frac{n(\mathbf{r})n(\mathbf{r}')}{|\mathbf{r} - \mathbf{r}'|}}_{\langle \hat{V}_{int} \rangle} + E_{XC} + E_{II}, \quad (2.13)$$

where the energy of the classical electrostatic electron-electron interaction is given as the double integral over the charge density. Thomas [58] and Fermi [59] attempted to solve Eq. 2.13 by assuming the kinetic energy of the electrons was a functional of the density $\langle \hat{T} \rangle = T[n(\mathbf{r})]$, the explicit form of which was described by the kinetic energy of a non-interacting homogeneous electron gas as:

$$T_{TF} = \frac{3\hbar^2}{10m_e} (3\pi^2)^{\frac{2}{3}} \int d\mathbf{r} [n(\mathbf{r})]^{\frac{5}{3}}, \quad (2.14)$$

Unfortunately the Thomas-Fermi model provides a poor approximation for the kinetic energy, which ultimately leads to a larger error than simply neglecting the exchange correlation term

entirely would. To solve this problem, and overcome the limitations imposed by the approximation of the kinetic energy functional, Kohn and Sham [60], building on the work of Hohenberg and Kohn [61], proposed to calculate the exact kinetic energy of a non-interacting reference system of the same density as the real interacting one. In this approach the density is calculated as a set of independent wave functions:

$$n(\mathbf{r}) = \sum_{i=1}^N |\psi_i(\mathbf{r})|^2, \quad (2.15)$$

where i runs over all occupied states from 1 to N and ψ_i are the eigenstates of the non-interacting system. As the many body effects in the Kohn-Sham approach are all contained in the exchange correlation functional, the kinetic energy can then be expressed using Eq. 2.15 as:

$$T_{KS} = -\frac{\hbar^2}{2m_e} \sum_{i=1}^N \langle \psi_i | \nabla_i^2 | \psi_i \rangle, \quad (2.16)$$

The overall energy of the system using the Kohn-Sham formalism can then be expressed as:

$$E_{KS} = -\frac{\hbar^2}{2m_e} \sum_{i=1}^N \langle \psi_i | \nabla_i^2 | \psi_i \rangle + \int d\mathbf{r} V_{ext}(\mathbf{r}) n(\mathbf{r}) + \frac{1}{8\pi\epsilon_0} \int \int d\mathbf{r} d\mathbf{r}' \frac{n(\mathbf{r})n(\mathbf{r}')}{|\mathbf{r} - \mathbf{r}'|} + E_{XC}[n(\mathbf{r})] + E_{II}, \quad (2.17)$$

As E_{II} is a constant there is an explicit solution to each term in Eq. 2.17 except for the exchange correlation energy E_{XC} . Solution of the exchange correlation is non-trivial and acts in practice to limit the accuracy of DFT methods. Expressing E_{XC} as the difference between the many-body interacting system and the non-interacting reference system we get:

$$E_{XC} = \langle \hat{T} \rangle - T_{KS} + \langle V_{int} \rangle - E_{Hartree} \quad (2.18)$$

By now applying the variational principle to the energy E_{KS} and asking what condition must the orbitals ψ_i fulfill so as to minimize the energy under the constraint of orthonormality for the wave functions $\langle \psi_i | \psi_j \rangle = \delta_{ij}$, one arrives at the Kohn-Sham equations:

$$\hat{H}_{KS} \psi_i = \epsilon_i \psi_i(\mathbf{r}), \quad \hat{H}_{KS} = -\frac{\hbar^2}{2m_e} \nabla^2 + \hat{V}_{KS}(\mathbf{r}), \quad (2.19)$$

where the effective Kohn-Sham potential \hat{V}_{KS} is given by:

$$\widehat{V}_{KS} = \widehat{V}_{ext}(\mathbf{r}) + \frac{\delta E_{Hartree}}{\delta n(\mathbf{r})} + \frac{\delta E_{XC}}{\delta n(\mathbf{r})} \quad (2.20)$$

2.4 Exchange-correlation Functionals

It is clear from Eq. 2.18 that accurate solution of the Kohn-Sham Hamiltonian is largely reliant on finding accurate functionals for the exchange correlation energy. In this section we will detail three of the main approaches to approximating the exchange correlation energy of a system. These approaches are the local density approximation, the general gradient approximation and Heyd-Scuseria-Ernzerhof hybrid functionals.

2.4.1 Local density approximation

The local density approximation (LDA) is the most straightforward approximation for the exchange correlation energy of a system. In the local density approximation the exchange correlation per particle at each spatial point is approximated as the exchange correlation per particle from a homogeneous electron gas (HEG) with a density equivalent to the density at this same point. To begin we write the exchange-correlation energy of the LDA in the form:

$$E_{XC}^{LDA}[n(\mathbf{r})] = \int d\mathbf{r} n(\mathbf{r}) \epsilon_{XC}^{HEG}(n(\mathbf{r})), \quad (2.21)$$

where $\epsilon_{XC}^{HEG}(n(\mathbf{r}))$ is the exchange-correlation energy per particle of a homogeneous electron gas of density $n(\mathbf{r})$. The $\epsilon_{XC}^{HEG}(n(\mathbf{r}))$ here contains a weighted probability $n(\mathbf{r})$ that there exists an electron at position (\mathbf{r}) . Separating this exchange-correlation energy into exchange and correlation contributions then gives:

$$\epsilon_{XC}^{HEG}(n(\mathbf{r})) = \epsilon_X^{HEG}(n(\mathbf{r})) + \epsilon_C^{HEG}(n(\mathbf{r})) \quad (2.22)$$

A HEG consists of N_e interacting electrons in a volume, V , which has a positive background charge which keeps the overall charge of the system neutral. Usefully the homogeneous gas approach allows for representation of effects in solids that arise from the mutual repulsive interactions of electrons without needing to explicitly introduce the atomic lattice and structure making up a real solid. For a homogeneous electron gas of charge density n , the Wigner-Seitz radius r_S , can be expressed as the radius of a sphere whose volume is equal to the volume for a single electron:

$$\frac{V}{N_e} = \frac{4\pi}{3} r_s^3 = \frac{1}{n}, \quad (2.23)$$

which can then be re-expressed as:

$$r_s = \left(\frac{3}{4\pi n} \right)^{\frac{1}{3}} \quad (2.24)$$

Using Eq. 2.24, for a system of N_e electrons, the exchange energy per electron for the HEG ϵ_X^{HEG} can then be expressed as:

$$\frac{E_X^{HEG}}{N_e} = \epsilon_X^{HEG} = -\frac{1}{4\pi\epsilon_0} \frac{3e^2}{4\pi} \left(\frac{9\pi}{4} \right)^{\frac{1}{3}} \frac{1}{r_s}, \quad (2.25)$$

where E_x^{HEG} is the exchange energy for the HEG. By replacing the constant charge density n of the HEG in Eq. 2.25 with the local charge density $n(\mathbf{r})$ the LDA Exchange Energy can then be determined as:

$$E_X^{LDA}[n(\mathbf{r})] = \int d\mathbf{r} n(\mathbf{r}) \epsilon_X^{HEG}(n(\mathbf{r})) = -\frac{3}{4} \left(\frac{3}{\pi} \right)^{\frac{1}{3}} \int n(\mathbf{r})^{\frac{4}{3}} d\mathbf{r} \quad (2.26)$$

While the integrand in Eq. 2.26 allows for an analytic solution of the exchange energy contributions ϵ_X , no such explicit expression exists for the correlation contributions ϵ_C . Instead ϵ_C is typically parameterised using numerical data from highly accurate numerical quantum Monte-Carlo simulations of the homogeneous electron gas. The most common parametrisation in use for ϵ_C is that of Perdew and Zunger [62], implemented by Ceperley and Alder [63] on homogeneous electron gases at various densities.

Returning to Eq. 2.21 and Eq. 2.22 the total exchange correlation energy E_{XC}^{LDA} , of the LDA can be expressed as:

$$E_{XC}^{LDA}[n(\mathbf{r})] = \int d\mathbf{r} n\mathbf{r} (\epsilon_X^{HEG}(n(\mathbf{r})) + \epsilon_C^{HEG}(n(\mathbf{r}))) \quad (2.27)$$

The analytic solution of $\epsilon_X^{HEG}(n(\mathbf{r}))$ is given in Eq. 2.26 while $\epsilon_C^{HEG}(n(\mathbf{r}))$ has no analytic solution it can be parameterised using numerical quantum Monte-Carlo simulations.

2.4.2 General Gradient Approximation

Using the LDA approach equation 2.27 gives the exact exchange correlation energy for a system of constant charge density. In a real system however the charge density will not remain constant but will change with position. The logical progression from the LDA therefore, is to make use of not only the density $n(\mathbf{r})$ at a particular point, but also the successive spatial derivatives of the density, starting with the gradient $\nabla n(\mathbf{r})$, in order to account for the non-homogeneity of electron density in a real material.[64, 65] By assuming that $\epsilon_{XC}(r)$ is a functional of both $n(\mathbf{r})$ and the first order gradient $|\nabla n(\mathbf{r})|$ we can write the exchange-correlation energy in the following form, which is termed the generalized gradient approximation (GGA) [66]:

$$E_{XC}^{GGA}[n(\mathbf{r})] = \int d\mathbf{r} n(\mathbf{r}) \epsilon_{XC}^{GGA}(n(\mathbf{r}), |\nabla n(\mathbf{r})|) \quad (2.28)$$

Many GGAs exist, with three forms seeing particularly wide use, those being the Becke (B88) [67], Perdew and Wang (PW91) [68] and Perdew, Burke and Enzerhof (PBE) [66] forms. As Martin notes, on pg. 156 of [69] one must be careful in the implementation of the GGA so as to avoid inconsistencies in calculations arising from the approximation in Eq. 2.28. Depending on the properties of the system being investigated either LDA or GGA can lead to better agreement with experimental values. While the LDA tends to overbind [70] leading to theoretical bond lengths and lattice parameters which are too short compared to experiment the GGA suffers from the opposite problem, tending to underbind [71, 72] which leads to bond lengths and lattice parameters which are too large compared to experimental values. A major issue for both the LDA and GGA methods is that both methods are seen to underestimate the band gaps of semiconductors and insulators [73]. This underestimation of the band gap of semiconductors is corrected in the modified Becke-Johnson and hybrid functional approaches which are detailed in the next two sections, and which will be used later in the thesis.

2.4.3 Modified Becke-Johnson approximation

The modified Becke Johnson approximation [74, 75] is a meta-GGA exchange potential which, when used in combination with the LDA-correlation [68], yields band gaps with an accuracy similar to that of hybrid functional methods (detailed in Sec. 2.4.4) but at a fraction of the computational expense. In effect the modified Becke-Johnson potential is a local approximation to an atomic exact-exchange potential with an added screening term and is expressed as:

$$V_X^{mBJ}(\mathbf{r}) = c V_X^{BR}(\mathbf{r}) + (3c - 2) \frac{1}{\pi} \sqrt{\frac{5}{12}} \sqrt{\frac{2\tau}{n(\mathbf{r})}}, \quad (2.29)$$

where $V_X^{mBJ}(\mathbf{r})$ is the modified Becke-Johnson exchange potential, $V_X^{BR}(\mathbf{r})$ is the Becke-Roussel potential [76], $n(\mathbf{r})$ is the electron density and $\tau(\mathbf{r})$ is the kinetic energy density given by:

$$\tau(\mathbf{r}) = -\frac{1}{2} \sum_i |\nabla \Psi_i|^2 \quad (2.30)$$

The Becke-Roussel potential in 2.29 is introduced to mimic the Coulomb potential created by the exchange hole and can be expressed as:

$$V_X^{BR}(\mathbf{r}) = -\frac{1}{b(\mathbf{r})} \left(1 - e^{-x(\mathbf{r})} - \frac{1}{2} x(\mathbf{r}) e^{-x(\mathbf{r})} \right), \quad (2.31)$$

where x is determined from an equation explicitly involving $n(\mathbf{r})$, $\nabla n(\mathbf{r})$, $\nabla^2 n(\mathbf{r})$ and τ , and where the function b is given by the equation:

$$b = \left(\frac{x^3 e^{-x}}{8\pi n(\mathbf{r})} \right)^{\frac{1}{3}}, \quad (2.32)$$

Finally the parameter c in the expression of the modified Becke-Johnson exchange potential in Eq. 2.29 depends linearly on the square root of the average of $\frac{|\nabla n(\mathbf{r}')|}{n(\mathbf{r}')}$ and is expressed as:

$$c = \alpha + \beta \left(\frac{1}{V_{cell}} \int_{cell} \frac{|\nabla n(\mathbf{r}')|}{n(\mathbf{r}')} d^3 r' \right)^{\frac{1}{2}}, \quad (2.33)$$

where α and β are two free parameters and V_{cell} is the unit cell volume. Minimization of the mean absolute relative error for the band gap over a series of solids gives optimal values of $\alpha = -0.012$ and $\beta = 1.023$. c is left as a tunable free parameter which can then be tuned to the band gap of the material being studied. For $c = 1$ the calculated band gap in all cases is found to be lower than experimental values [77], but increasing the value of c leads in all cases to a monotonic increase in the band gap. For solids with small band gaps the optimal value of c when compared to experimental values was found to lie in the range of 1.1–1.3 [75], while the optimal c for materials with larger band gaps was found to be in the range of 1.4–1.7 [75].

2.4.4 Hybrid functionals

While the mBJ approach discussed in the previous section gives excellent agreement to experimental values when parameterised so as to best fit a known band gap, it is limited to material systems where the fundamental band structure has already been well established. As such highly accurate computational DFT methods are still required for the investigation of emerging materials. One such method is the hybrid functional DFT.

Hybrid functionals are a class of approximations for the exchange-correlation energy functional that incorporate a portion of exact exchange from Hartree-Fock theory, with the rest of the exchange-correlation energy being determined by ab initio or empirical methods. In the hybrid functional approximation the exact exchange energy functional is expressed not in terms of the density but rather in terms of the Kohn-Sham states. As such it is termed an implicit density functional.

A hybrid exchange—correlation functional is usually constructed as a linear combination of the Hartree-Fock exact exchange functional:

$$E_x^{HF} = -\frac{1}{2} \sum_{i < j} \int \int \psi_i^*(\mathbf{r}) \psi_j^*(\mathbf{r}') \frac{1}{|\mathbf{r} - \mathbf{r}'|} \psi_j(\mathbf{r}) \psi_i(\mathbf{r}') d\mathbf{r} d\mathbf{r}', \quad (2.34)$$

and any number of exchange and correlation explicit density functionals. In most hybrid functional schemes the parameters determining the weight of each individual functional are set by fitting the functional's predictions to experimental or accurately calculated thermochemical data.

2.4.5 Heyd-Scuseria-Ernzerhof hybrid functionals

One such scheme, which we will be making use of throughout this thesis, is the Heyd-Scuseria-Ernzerhof screened-exchange-correlation functional [78, 79] which uses a screened Coulomb potential to calculate the exchange energy of the system. Within the HSE approximation the screened Coulomb potential is only applied to the exchange interaction, in order to screen the long-range part of the Hartree-Fock (HF) exchange. All other Coulomb interactions of the Hamiltonian, including the Coulomb repulsion interaction of electrons in the system, do not use a screened potential. In order to apply the screening potential in this manner the Coulomb operator is split into short-range (SR) and long-range (LR) components:

$$\frac{1}{|\mathbf{r} - \mathbf{r}'|} = \underbrace{\frac{\text{erfc}(\omega|\mathbf{r} - \mathbf{r}'|)}{|\mathbf{r} - \mathbf{r}'|}}_{\text{(SR)}} + \underbrace{\frac{\text{erf}(\omega|\mathbf{r} - \mathbf{r}'|)}{|\mathbf{r} - \mathbf{r}'|}}_{\text{(LR)}}, \quad (2.35)$$

where $\text{erfc}(\omega|\mathbf{r} - \mathbf{r}'|) = 1 - \text{erf}(\omega|\mathbf{r} - \mathbf{r}'|)$ and where ω is a tunable screening parameter. Using the HSE approximation, the exact exchange mixing is only performed for short-range interactions in **both** HF and DFT, allowing the exchange hole to become delocalized among the near neighbours of a reference point, but not beyond. As such in the HSE scheme only a portion of the short range exchange is from HF, with the rest of the exchange coming from the Perdew-Burke-Ernzerhof (PBE) [66, 70, 80–82] functional. Schematically, the exchange-correlation functional of the HSE, E_{XC}^{HSE} can be expressed as:

$$E_{xc}^{HSE} = aE_x^{HF,SR}(\omega) + (1 - a)E_x^{PBE,SR}(\omega) + E_x^{PBE,LR}(\omega) + E_c^{PBE}, \quad (2.36)$$

where a is the mixing parameter which determines how much exact exchange is included in the calculation, and ω is an adjustable parameter which controls the range of the interaction.

The Hartree Fock short-range exchange energy, $E_x^{HF,SR}$ from Eq. 2.36 can be determined from:

$$E_x^{HF,SR}(\omega) = -\frac{1}{4\pi\epsilon_0} \sum_{i<j} \int \int \psi_i^*(\mathbf{r})\psi_j^*(\mathbf{r}') \frac{erfc(\omega|\mathbf{r}-\mathbf{r}'|)}{|\mathbf{r}-\mathbf{r}'|} \psi_j(\mathbf{r})\psi_i(\mathbf{r}') d\mathbf{r}d\mathbf{r}' \quad (2.37)$$

The standard values of a and ω used in Eq. 2.36 are 1.4 and 0.2 respectively (usually referred to as HSE06) which for most systems give good agreement with experimentally measured values [83, 84].

2.5 Pseudopotentials

In this section we will give a brief overview of the fundamental theory underlying pseudopotentials and the projector augmented wave method which we will implement within the VASP framework in later chapters of this thesis. A more complete description of these topics can be found in Blöchl's original paper [85].

A pseudopotential is an effective potential which is designed to replicate the effect of core electrons and the nucleus of an atom (all-electron potential) such that the "core" states, which consist of the nucleus and inner electrons and which are highly localized around the nucleus, are effectively eliminated and the Coulomb interaction between the core and the valence electrons is replaced by a smoother matching potential. This is done to ensure that the use of plane waves to expand the electron wavefunctions is possible, as such a calculation involving both core and valence electrons and the full Coulombic potential of the nuclei, would be prohibitively time consuming. Replacing valence states with pseudo wavefunctions which can be described with far fewer Fourier modes, simplifies the calculation and makes a plan-wave expansion far more practical to use.

The core concept of pseudopotentials is that the majority of physical properties of solids depend solely upon the valence electrons. The core states which lie much lower in energy, only negligibly interact with these valence states. As such it is possible to partition the electrons between core and valence states [86–88]. A notable exception to this general rule are elements with semi-core states which are high enough in energy to influence the chemical properties of the element. In such elements, ZnS or GaN for instance where the semi-core 3d states of Zn or Ga are close in

energy to the valence states, the semi-core states must be explicitly included as valence states for accurate calculations [89, 90].

The most common types of pseudopotentials are norm conserving [91], ultrasoft (US) [92] and projector augmented-wave method potentials (PAW) [85, 93]. In this thesis we focus on the use of PAW pseudopotentials, which are introduced in the next section.

2.5.1 Projector augmented-wave method

In this section we will give a brief description of the projector augmented-wave method. A more full description of this method can be found in the original Blöchl paper [85] while its implementation in the VASP software package is detailed at length in [93]. We start from the linear transformation \mathcal{T} which relates the all electron wave function $|\psi\rangle$ to the auxiliary smooth pseudo-wavefunction $|\tilde{\psi}\rangle$:

$$|\psi\rangle = \mathcal{T}|\tilde{\psi}\rangle \quad (2.38)$$

Next we define Ω_R as a spherical radius around the atom R , known as the augmentation region. In the context of pseudopotentials the augmentation region Ω_R relates to the region encompassing the nucleus and core electrons. In order to have $|\tilde{\psi}\rangle$ and $|\psi\rangle$ differ only in this spherical augmentation regions Ω_R , we denote \mathcal{T} as:

$$\mathcal{T} = 1 + \sum_R |\mathcal{T}_R\rangle, \quad (2.39)$$

where \mathcal{T}_R is a transformation operator which is chosen to be non-zero only within Ω_R . As a result, outside of the augmentation region Ω_R , $|\tilde{\psi}\rangle$ and $|\psi\rangle$ are equivalent. Within the augmentation regions we then expand the true all-electron wavefunction ψ in to the partial waves ϕ_i and we can similarly expand the pseudo-wavefunction $\tilde{\psi}$, in to the smooth partial waves $\tilde{\phi}_i$ such that:

$$|\phi_i\rangle = (1 + \mathcal{T}_R)|\tilde{\phi}_i\rangle, \quad (2.40)$$

$$\mathcal{T}_R|\tilde{\phi}_i\rangle = |\phi_i\rangle - |\tilde{\phi}_i\rangle, \quad (2.41)$$

with, $|\phi_i\rangle = |\tilde{\phi}_i\rangle$ outside the augmentation region Ω_R . Provided that the smooth partial waves form a complete set inside the augmentation sphere, we can expand the smooth pseudo wave functions as:

$$|\tilde{\psi}\rangle = \sum_i c_i |\tilde{\phi}_i\rangle \quad \text{within } \Omega_R, \quad (2.42)$$

where c_i are for now, undetermined expansion coefficients. Since $|\phi_i\rangle = \mathcal{T}|\tilde{\phi}_i\rangle$ we can similarly expand the true all-electron wave functions as:

$$|\psi\rangle = \mathcal{T}|\tilde{\psi}\rangle = \sum_i c_i |\phi_i\rangle \quad \text{within } \Omega_R, \quad (2.43)$$

with identical expansion coefficients, c_i . Since the operator \mathcal{T} is linear, the coefficients c_i can be determined as an inner product with the projector functions, $|p_i\rangle$:

$$c_i = \langle p_i | \tilde{\phi}_i \rangle, \quad (2.44)$$

with $\langle p_i |$ satisfying the condition,

$$\sum_i |\tilde{\phi}_i\rangle \langle p_i| = 1 \quad \text{within } \Omega_R, \text{ and } 0 \text{ outside} \quad (2.45)$$

Finally, the transformation \mathcal{T} can be expressed as:

$$\mathcal{T} = 1 + \sum_i \mathcal{T}_R |\tilde{\phi}_i\rangle \langle p_i| = 1 + \sum_i (|\phi_i\rangle - |\tilde{\phi}_i\rangle) \langle p_i| \quad (2.46)$$

Using Eq. 2.46 the all electron wavefunction can be determined from the psuedo-wavefunction as

$$|\psi\rangle = |\tilde{\psi}\rangle + \sum_i (|\phi_i\rangle - |\tilde{\phi}_i\rangle) \langle p_i | \tilde{\psi} \rangle \quad (2.47)$$

Further technical details for the practical implementation of the PAW method for use in the VASP framework can be found in [93].

2.6 The Vienna ab initio Simulation Package

VASP, the Vienna Ab initio Simulation Package [85, 93–96], is a computational tool used for atomic scale materials modelling, including the calculation of electronic band structure and quantum mechanical molecular dynamics, from first principles methods.

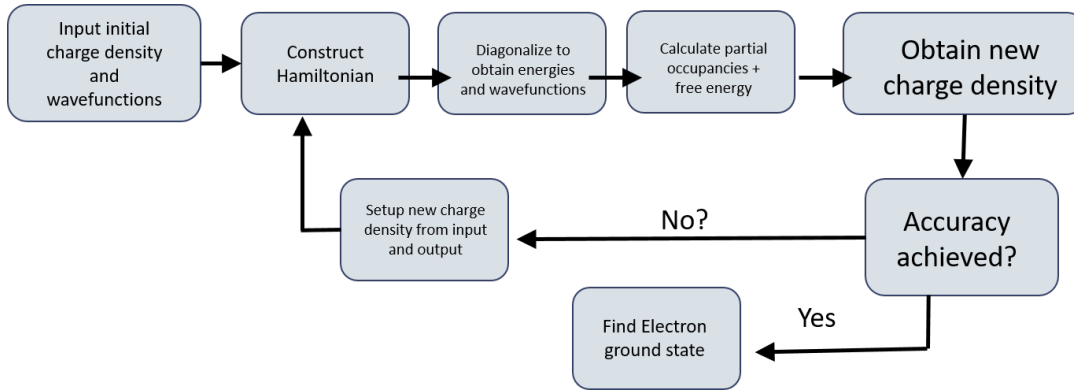


FIGURE 2.2: Flux diagram of the basic steps in VASP to find the self-consistent solution for the electronic ground state of a system of atoms.

VASP is used to self consistently compute an approximate solution to the many-body Schrödinger equation, for a system of atoms. In this thesis we will primarily use VASP within the DFT framework, to solve the Kohn-Sham equations for a system of atoms from first principles. This involves the iterative optimization of the charge density, as detailed in Fig. 2.2. In this iterative process the charge density is calculated and used to determine the Kohn-Sham Hamiltonian for the system. The Kohn-Sham Hamiltonian may then in turn be used to determine the single particle eigenstates from which a new charge density, which acts as part of the input charge density for the next iterative step, can be calculated. Over a series of iterative steps the difference between new and old charge densities is converged to within a desired precision, giving a final charge density which can be used to accurately determine the Kohn-Sham equations for the system.

In VASP, central quantities, like the one-electron orbitals, the electronic charge density, and the local potential are expressed in plane wave basis sets. The interactions between the electrons and ions can be described using norm-conserving or ultrasoft pseudopotentials, or the projector-augmented-wave method.

2.7 Band Unfolding

Calculations involving the simulation of realistic systems frequently utilize a supercell (SC) approach, involving the approximation of a solid as a large periodically repeating cell. For a sufficiently large cell the quantum mechanics of the system should give a good approximation of those of a realistic solid. We note however that the application of periodic boundary conditions can impose an artificial periodicity on interactions in the system. While the primitive cell (PC) and the supercell descriptions of a perfectly periodic material are equivalent, the supercell description suffers from having complicated band structures which arise from the folding of the bands into the smaller supercell Brillouin zone and which occurs even for relatively small

supercell sizes. To properly interpret the band structure in such cases it is necessary first to unfold the bands back. Here we have opted to use the BandUp programme following the procedure laid out in [97, 98] to recover an effective primitive cell picture of the band structure from the folded supercell band structure.

We begin by defining V_{PCBZ} and V_{SCBZ} as the volumes of the primitive cell and supercell Brillouin zones respectively. For each wave vector \mathbf{K} of the supercell Brillouin zone (V_{SCBZ}) there exist $N_{unfold} \equiv V_{PCBZ}/V_{SCBZ}$ wavevectors \mathbf{k}_i of the primitive cell Brillouin zone such that

$$\mathbf{k}_i = \mathbf{K} + \mathbf{G}_{K \rightarrow k_i}, \quad i = 1, 2, 3, \dots, N_{unfold}, \quad (2.48)$$

where $\mathbf{G}_{K \rightarrow k_i}$ are vectors belonging to the supercell reciprocal lattice. The *unfolding vector* $\mathbf{G}_{K \rightarrow k_i}$ *unfolds* \mathbf{K} onto \mathbf{k}_i and has a reverse operation

$$\mathbf{K} = \mathbf{k} - \mathbf{G}_{k \rightarrow K}, \quad (2.49)$$

which folds \mathbf{k} into \mathbf{K} with folding vector $\mathbf{G}_{k \rightarrow K}$. For any given \mathbf{k}_i there is only one \mathbf{K} that satisfies this relationship.

Next we denote an eigenstate of the Hamiltonian in the supercell Brillouin zone representation as $|\psi_{\mathbf{K}}^{SC}\rangle$ and denote a set of wave vectors \mathbf{k}_i in the primitive cell Brillouin zone as $\{\tilde{k}_i\}$. These wavevectors relate to \mathbf{K} as detailed in Eq. 2.48 and correspond to primitive cell eigenstates $|\psi_{\mathbf{k}_i}^{PC}\rangle$ which are of the same eigenvalue as $|\psi_{\mathbf{K}}^{SC}\rangle$. The relation of the eigenstates $|\psi_{\mathbf{K}}^{SC}\rangle$ and $|\psi_{\mathbf{k}_i}^{PC}\rangle$ is detailed in [99, 100] as,

$$|\psi_{\mathbf{K}}^{SC}\rangle = \sum_{\mathbf{k}_i \in \mathbf{K}} a(\mathbf{k}_i; \mathbf{K}) |\psi_{\mathbf{k}_i}^{PC}\rangle. \quad (2.50)$$

The probability of eigenstate $|\psi_{\mathbf{K}}^{SC}\rangle$ having the same character as a primitive cell Bloch state of wave vector \mathbf{k}_i is then given in [99, 100] by a *spectral weight* $P_{\mathbf{K}}(\mathbf{k})$, defined as

$$P_{\mathbf{K}}(\mathbf{k}) \equiv \sum |\langle \psi_{\mathbf{K}}^{SC} | \psi_{\mathbf{k}}^{PC} \rangle|^2 = \sum |C_{\mathbf{K}}^{SC}(\mathbf{g} + \mathbf{k} - \mathbf{K})|^2, \quad (2.51)$$

where \mathbf{g} is an element of the primitive cell reciprocal lattice and $C_{\mathbf{K}}^{SC}$ are coefficients of the plane waves that span the eigenstates of the supercell. Eq. 2.51 shows that the spectral weight can be determined entirely from coefficients $C_{\mathbf{K}}^{SC}$ – no knowledge of the primitive cell eigenstates is necessary [99]. Finally a *spectral function* is defined in [99] as

$$A(\mathbf{k}; \epsilon) \equiv \sum P_{\mathbf{K}}(\mathbf{k}) \delta(\epsilon - \epsilon_m(\mathbf{K})), \quad (2.52)$$

where ϵ denotes the energy. From eq. 2.52 it is evident that only (\mathbf{k}, \mathbf{K}) pairs where \mathbf{K} unfolds onto \mathbf{k} need to be included. We can define a cumulative probability function $S_{\mathbf{k}}(\epsilon)$, where $dS_{\mathbf{k}}(\epsilon) = A(\mathbf{k}; \epsilon)d\epsilon$. $dS_{\mathbf{k}}(\epsilon)$ represents the weight of primitive cell bands at a given primitive cell wave vector \mathbf{k} and can be used within the region of interest in the supercell Brillouin zone to map the supercell states onto a primitive cell grid at energy intervals of size $\delta\epsilon$, and thereby assign a weight to each primitive cell point denoting the number of supercell bands at that point.

In chapter 4 of this thesis we apply the BandUp code within the VASP framework to unfold a series of disordered $\text{Ge}_{1-x}\text{Sn}_x$ alloy supercell band structures. Unfolding of the supercell band structure provides a clear qualitative indication of which critical point each of the alloy high symmetry conduction band states arises from and helps clarify how Sn incorporation impacts the alloy band structure.

Chapter 3

Experimental and theoretical investigation of GeSn alloys

3.1 Overview

In this chapter we present the details of our study of the nature of the band gap in GeSn alloys for use in silicon-based lasers. This work involved a combination of theoretical density functional theory and experimental methodologies, where the experimental side of the investigation of the band gap of germanium-tin alloys haven been undertaken by our collaborators Dr. Tim D. Eales and Prof. Stephen J. Sweeney of the University of Surrey. This experimental study involved the use of photovoltage measurements as a function of hydrostatic pressure on a series GeSn p-i-n photodiodes, with different Sn compositions (between 0 – 10%) grown by low temperature chemical vapour deposition, by the Fisher Yu group at the University of Arkansas. [101] By extracting the absorption edge from these photovoltage measurements and measuring the energy shift of the band gap under pressure the pressure coefficient of the direct band gap could be determined and compared with theoretically determined values.

Special attention was paid in this study to the investigation of Sn-induced band mixing effects. We demonstrate from both experiment and ab-initio theory that the (direct) Γ character of the GeSn band gap changes continuously with alloy composition and has significant Γ character even at low (6%) Sn concentrations. The evolution of the Γ character is due to Sn-induced conduction band mixing effects, in contrast to the sharp indirect-to-direct band gap transition obtained in conventional alloys such as $\text{Al}_{1-x}\text{Ga}_x\text{As}$. Understanding the band mixing effects is critical not only from a fundamental and basic properties viewpoint but also for designing photonic devices with enhanced capabilities utilizing GeSn and related material systems.

3.2 Introduction

In the field of photonics, it is a long-held goal to realise all-silicon based technologies. While silicon (Si) has been instrumental to the development of electronics, its use in photonics has been limited to passive components such as waveguides and devices such as photodetectors and modulators. The fundamental limitation of Si is its indirect band gap which significantly decreases the probability of light emission compared to direct band gap semiconductors such as GaAs. [102] Various strategies have been developed to overcome this fundamental limitation, such as direct epitaxial growth and heterogeneous integration of conventional III-V semiconductors on Si. [103–107] Germanium-tin (GeSn) offers the potential to engineer the first tunable group IV semiconductor alloy with a fundamentally direct band gap. [34, 35] In recent years this material system has received considerable attention as a viable pathway for the next generation of Si-compatible optoelectronic devices. Most significantly GeSn offers the potential to realise an efficient infrared light source on Si [25, 36, 37] with applications in optical interconnects and lab-on-chip trace gas detection. In addition narrow band gap semiconductors on Si offer opportunities for tunnelling enhancement in devices such as tunnelling-field effect transistors (TFETs) [49, 50] for which GeSn is considered as a potential candidate system. [108, 109] Also, Si has demonstrated enhanced nonlinear effects which is important for nonlinear THz applications, [110] and these nonlinear effects are expected to get stronger in narrow band gap materials such as GeSn and its alloys. [111] Due to recent advances in the growth of high crystalline quality GeSn and the diverse nature of its applications, the focus on GeSn alloys has gathered enormous pace. [46, 112–116] Critical to the development of these materials is obtaining a detailed understanding of the band structure evolution of GeSn and the influence of Sn concentration on its electronic and optical properties.

Germanium (Ge) is fundamentally an indirect band gap semiconductor. The indirect energy gap, $E_g(L) = 664$ meV at 300 K is between the highest valence band (VB) state at Γ and the lowest conduction band (CB) states at L. The lowest conduction band Γ state lies 136 meV above the L conduction band minimum. [29] A schematic band structure of bulk Ge is illustrated in Figure 3.1. The present discussion in the literature regarding the band gap evolution of GeSn alloys is based on the assumption that with increasing Sn composition there is a sharp transition from GeSn being an indirect band gap material to a direct one. [46, 112, 117–119] However, there is a large degree of uncertainty for the Sn concentration at which this transition occurs, with typical values ranging from $\sim 6 - 11\%$ Sn. [41–44] Moreover, this analysis neglects alloy induced band mixing effects, which could render the assumption of a sharp direct to indirect band gap invalid. For an alloy with strong band mixing effects, rather than labelling a semiconductor as “direct” or “indirect” it is more appropriate to consider the fractional Γ character of the conduction band edge (CBE). Thus, the fractional Γ character describes what proportion of the lowest conduction states have Γ - like (direct) character.

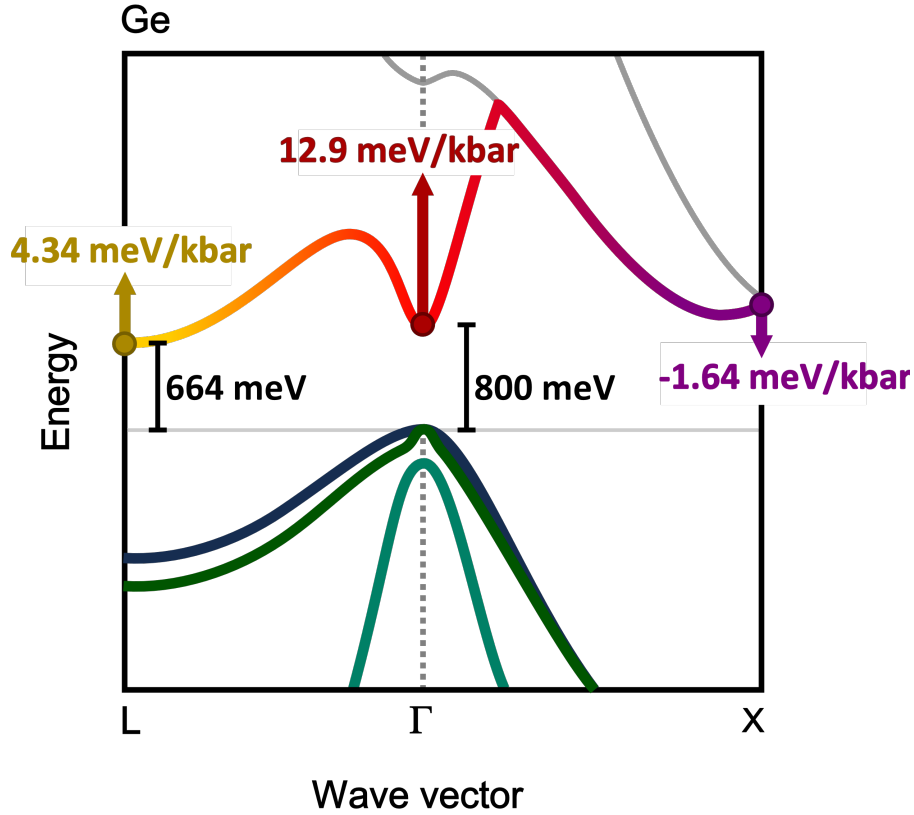


FIGURE 3.1: Schematic illustration of the pure bulk Ge band structure at 300K with the Γ , X and L energy gaps and pressure coefficients calculated by Wei and Zunger [123] indicated with respect to the valence band edge at the Γ -point.

Both the optical gain in a laser [120] and the tunnelling rate in a TFET at the band edge [121] depend directly on the square of the Kane momentum matrix element, $|P|^2$, which describes the coupling between the lowest conduction and highest valence states. This, in turn, is directly proportional to the fractional Γ character of the lowest conduction band states. [122] Therefore, understanding the conduction Γ -L state mixing in GeSn is of central importance from a fundamental physics perspective, but also for designing the next generation of group IV electronic and optoelectronic devices.

In this work we show from both experiment and ab-initio theory that there is not a sharp direct to indirect transition in GeSn. Instead, the evolution of the GeSn optical and electronic properties is determined by band mixing effects between the Γ and L conduction band states. It is therefore more appropriate to discuss the nature of the GeSn band gap in terms of the fractional Γ character of the alloy fundamental band gap E_g rather than in the widely accepted frame of a sharp indirect to direct gap transition. In earlier theoretical studies these features have been neglected either through the choice of supercell, [124] or through insensitivity of the model to these effects (e.g. treating the material in the virtual crystal approximation). [125] Previous experimental works such as those based on photoreflectance are also insensitive to indirect transitions [126–128]. Using high hydrostatic pressure measurements, we address the question of the fractional Γ character of the conduction band edge in GeSn alloys. The direct

and indirect band gaps in Ge have distinctly different pressure dependencies, as illustrated in Figure 3.1. The value of the pressure coefficient may therefore be used to distinguish between direct and indirect band gap transitions in GeSn alloys. GeSn p-i-n diode samples with Sn concentrations of 6.1%, 6.4% and 9.2% ($\pm 0.3\%$) are investigated using pressure dependent photovoltage spectroscopy measurements of the absorption edge in Sec. 3.5. As discussed in detail below, with only 6% Sn, the pressure coefficient of the GeSn absorption edge, at $9.2 \text{ meV kbar}^{-1}$, is intermediate between that of the indirect L gap ($4.3 \text{ meV kbar}^{-1}$) and that of the direct Γ gap ($12.9 \text{ meV kbar}^{-1}$), providing clear evidence of the substantial Γ character of E_g below what is typically predicted as the indirect-direct band gap crossover in GeSn alloys. [41–44] Furthermore, we show that with increasing Sn concentration, the pressure coefficient increases monotonically, approaching that of the direct Γ gap. The intermediate value pressure coefficient for 6% Sn is analogous to that observed previously in dilute-nitride $\text{GaInN}_x\text{As}_{1-x}$ systems, where the reduced pressure coefficient was used to identify a band anti-crossing interaction between the GaInAs host matrix Γ CBE and N-related localised states lying above the CBE. [129, 130]

These experimental measurements are accompanied by hybrid functional density functional theory studies of $\text{Ge}_{1-x}\text{Sn}_x$, in structures that allow for Γ - and L-state mixing effects and account for alloy induced features on a microscopic level. The significant Γ character and transitional behaviour in the pressure coefficient observed in the experiment indicates band mixing effects between the CB states. The experimental findings are supported by our atomistic, first-principles calculations detailed in Sec. 3.6. The pressure dependent band edge calculations reveal very similar trends when compared to the experimental results, supporting the Γ -L state mixing effect. Moreover, our theoretical calculations give insight into the origin of the mixing between the different conduction band states.

Overall, the combined experimental and theoretical work presented in this chapter provides evidence of substantial Γ (direct-gap) character in GeSn, even at compositions where the band gap is expected to be indirect. The dominant Γ character, present even with 6% Sn concentrations is indicative of CB mixing effects. The analysis and conclusions presented here are fundamentally different to the usual assumption of a sharp indirect-to-direct band gap transition in GeSn alloys. Such band mixing can therefore lead to improved optical properties at lower Sn concentrations than would otherwise be expected, as well as opening an efficient tunnelling path in TFETs. But, at the same time the intrinsic alloy fluctuations may lead to an inhomogeneous broadening of the band edges, which impacts the TFET turn-on rate, reduces electron mobility and broadens the gain spectrum thereby reducing the peak gain. Therefore, a higher carrier density for transparency and threshold may be required in lasers. Although the composition dependence of mixing effects on broadening is uncertain, mixing is likely to be strongest near the indirect/direct band gap “crossover” and to become less important with increasing Sn content.

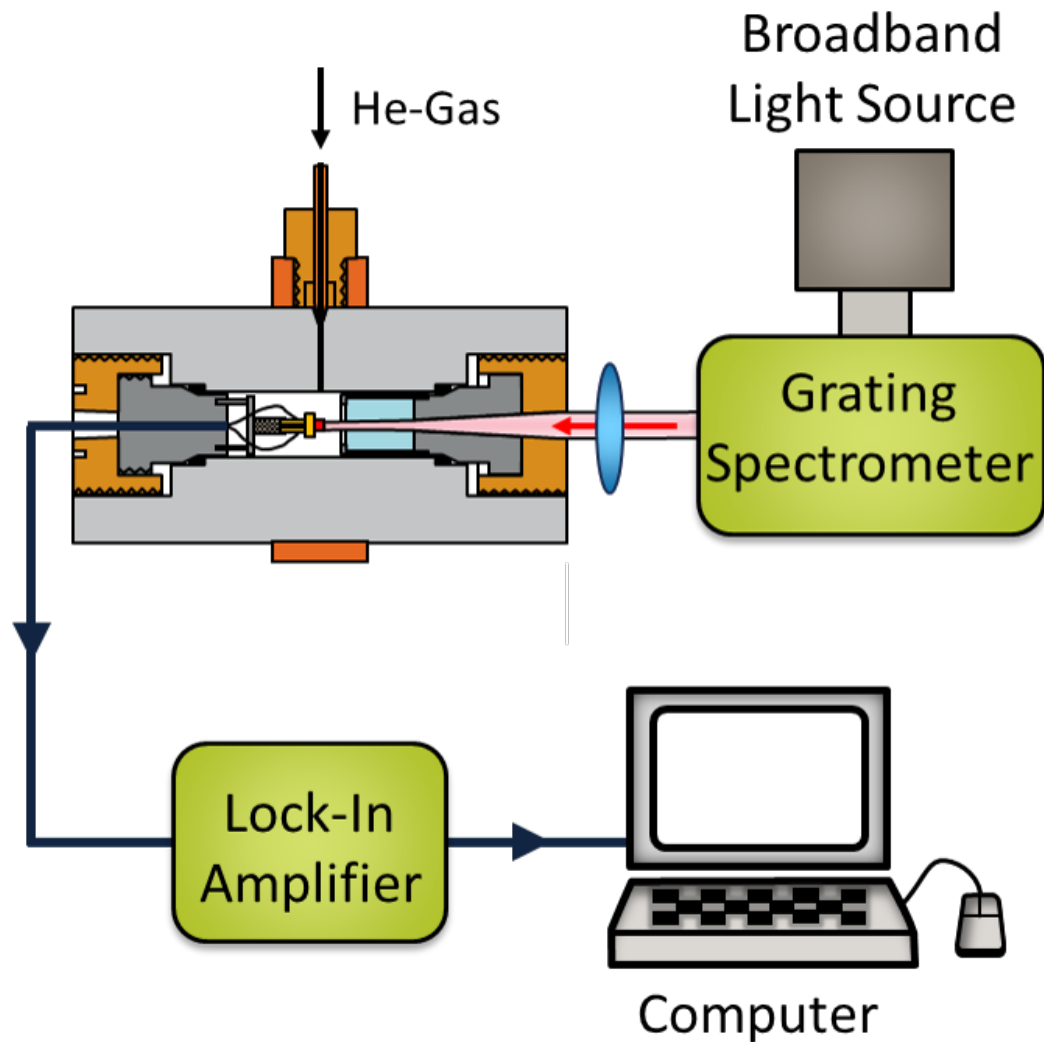


FIGURE 3.2: Schematic illustration of the experimental setup used to perform the photovoltage measurements under high hydrostatic pressure generated by Dr. Tim Eales [131]

3.3 Experimental methods

3.3.1 Sample Fabrication

The samples were fabricated, by Fisher Yu's group in the University of Arkansas, into circular mesa structures with diameters of 100, 250 and 500 μm using photo lithography and wet etching processes. The wet chemical etch ($\text{HCl}:\text{H}_2\text{O}_2:\text{H}_2\text{O} = 1:1:20$ at room temperature) showed a stable etching rate of 100 nm/min regardless of Sn composition. A 100-nm-thick SiO_2 passivation layer was then deposited by plasma-enhanced chemical vapour deposition followed by the openings made for the metal contacts. The p- and n-type metal contacts consist of 10 nm Cr and 200 nm Au defined by metal deposition and liftoff processes.

3.3.2 Experimental Setup

Figure 3.2 shows the experimental setup that was used to perform photovoltage measurements on the GeSn photodiodes under high hydrostatic pressure. For these photovoltage measurements light from a broadband source was selected using a Bentham TMc300 Triple Grating Monochromator. The spectrometer steps then through wavelengths from $2\mu\text{m}$ - $2.5\mu\text{m}$ using an internal optical chopper to modulate the output so as to vary the absorption depth of the photons. The GeSn samples being investigated were mounted on transistor outline headers using thermoconductive epoxy as an adhesive and the transistor outline pins were contacted to the mesa's n and p contacts with gold wire bonding. A Stanford Research Systems SR830 lock-in amplifier was placed in parallel with the device to measure photovoltage from the sample. The device was loaded into a non-magnetic CuBe high pressure cell. Hydrostatic pressure was applied with a gas compression system (UniPress) using helium gas as an inert hydrostatic pressure medium. Optical access was provided through a small sapphire window in the high pressure cell and the light was focused onto the mesa.

3.3.3 Surface Photovoltage

Surface photovoltage (SPV) is defined as the illumination-induced change in the surface potential. The underlying principle of photovoltage measurements is that the depletion region in the p-n junction of a semiconductor has an internal electric field due to the ionization of donors and acceptors at the junction. By directing modulated light on the depletion region of the p-n junction, one can induce the formation of free carriers, as photons from the light are absorbed creating electron hole pairs. These carriers separate out due to the internal electric field of the p-n junction and can be detected as photovoltage. [132] From these measurements and the Beer Lambert Law the absorption coefficient can then be extracted. [133]

3.4 Theoretical Framework

The band structure calculations in this chapter are undertaken using density functional theory (DFT) in the Heyd Scuseria Ernzerhof (HSE) hybrid functional scheme. [78, 79, 134] The details of our HSE-DFT calculations, implemented in the Vienna ab-initio software package (VASP) [95, 96] are given in Sec. 3.4.1 below. However, before presenting the details, it is useful to discuss briefly theoretical approaches to analyse the evolution of the band structure and potential (conduction) band mixing effects in an alloy such as GeSn. A widely used approach to address this question is band unfolding, where the bands of the supercell are folded back to the larger original primitive first Brillouin zone. [97, 99, 135] From the resulting unfolded band structure, the k character of the energetically lowest lying CB state in the Brillouin zone (e.g.

at the Γ and/or the L point) can be identified. Analysing the spectral weights of this state at different k-points can then give insight into band mixing effects. However, depending on how many states are involved in the band mixing, it can be difficult to identify these contributions easily and clearly. For example, because there are 4 L states in the unfolded band structure, and the lowest state at Γ can mix with all 4 of them, only a small fraction (25%) of this L character is associated with the one L point typically shown in an unfolded band structure. A quick visual inspection of the unfolded band structure can then significantly underestimate the amount of mixing present. Here we employ a different approach to study the evolution of the CBE character in GeSn alloys, namely performing hydrostatic pressure dependent DFT calculations. In doing so we obtain the same information as from the band unfolding, but with the additional benefits that we can (i) identify band mixing effects more clearly, given the large differences in Γ , L and X pressure coefficients and (ii) directly compare our theoretical results to the experimental data.

3.4.1 Density Functional Theory

All our density functional theory (DFT) studies have been performed within the Heyd Scuse-ria Ernzerhof (HSE) hybrid functional scheme, using the projector augmented-wave (PAW) method. [85, 93] More specifically we apply here the HSEsol scheme. [95] The calculations have been carried out in the framework of the plane-wave-based ab initio package VASP. [93, 95] For an accurate description of the CB and VB structures of both Ge and α -Sn we have used the following settings: the screening parameter μ was set to 0.2 \AA^{-1} while the exact exchange mixing parameter is 0.3. To avoid artefacts from Pulay stresses when performing structural relaxations and connected electronic structure calculations, a large plane wave cut-off energy of 400 eV was used. For the bulk calculations, the underlying Γ -centered k-point grid is $6 \times 6 \times 6$. For the supercell calculations (16 atom face centred cubic cell, and 64 atom cubic cells) a $3 \times 3 \times 3$ Γ -centered k-point mesh was applied. Our calculations include spin-orbit coupling (SOC) to achieve an accurate description of the α -Sn band structure at the Γ point. The semi-core d-states in Ge and Sn were treated as core electrons, since several studies have reported that unfreezing them has a negligible effect on the electronic structure. [124, 136] Within this theoretical framework the conduction band splitting between the Γ and L states in Ge is 143 meV, which is in very good agreement with the literature data. Furthermore, for α -Sn we calculate a spin orbit splitting energy (ΔE_{SO}) of $\Delta E_{SO} = 0.751 \text{ eV}$ and a negative band gap of $E_g(\Gamma) = -0.373 \text{ eV}$. Again these numbers are in good agreement with the experimental ($\Delta E_{SO} = 0.8 \text{ eV}$ [137]; $E_g(\Gamma) = -0.413 \text{ eV}$ [137]) and theoretical literature data ($\Delta E_{SO} = 0.681 \text{ eV}$ [136]; $E_g\Gamma = -0.519 \text{ eV}$ [136]) data. We conclude that the DFT approach used is ideally suited to investigate GeSn alloys on a first-principles level and can form the basis for developing empirical (atomistic) models.

3.4.2 Hydrostatic pressure coefficients

States originating from different wave vectors \mathbf{k} in the Brillouin zone of the primitive unit cell of the underlying diamond lattice are folded back to the zone centre ($\mathbf{K} = 0$) in supercell calculations. It can therefore be difficult to identify the character of individual zone-centre states in the band structure of a $\text{Ge}_{1-x}\text{Sn}_x$ supercell, and hence to deduce the composition at which the alloy becomes a direct-gap semiconductor. To address this issue, we investigate how the alloy CB structure changes as hydrostatic pressure is applied to the alloy supercell. The pressure coefficients $\frac{dE_g}{dP}$ for the indirect $L_{6c}-\Gamma_{8v}$ and $X_{9c}-\Gamma_{8v}$ and direct $\Gamma_{7c}-\Gamma_{8v}$ band gaps of Ge have respective values of 4.66, -1.60 and 13.33 meV kbar^{-1} in our HSEsol calculations. These values are again in good agreement with experimentally calculated values of Γ and L. [138–140] For α -Sn the pressure coefficients of Γ and L are comparable to those in Ge, having calculated values of 15.7 meV kbar^{-1} and 4.42 meV kbar^{-1} respectively. [123] As such it is expected that the pressure coefficients of the dilute $\text{Ge}_{1-x}\text{Sn}_x$ samples analysed in this work will not significantly differ from those of Ge.

Due to the significant difference in the pressure coefficients of the Γ and L states in Ge, contributions from direct and indirect-like states can be readily identified in dilute GeSn alloys. In this manner the calculation or measurement of $\frac{dE_g}{dP}$ for the fundamental band gap then allows one to identify the character of the band gap, and hence to track the evolution of the character of the CB edge states and band gap with increasing Sn composition x .

3.5 Experimental Results

In this section we discuss the results of the experimental investigation of the optical properties of the GeSn p-i-n photodiodes which was carried out by Prof. S. Sweeney and Dr. T.D. Eales on samples grown by the Fisher Yu group in Arkansas. We start in Sec. 3.5.1 by reviewing how the GeSn p-i-n photodiodes were grown. In the following sections we then discuss the results obtained by subjecting these GeSn samples to high hydrostatic pressure and taking photovoltage measurements from which the pressure coefficient of the samples conduction band edge was then determined.

3.5.1 Sample synthesis

The optical properties of GeSn are investigated using GeSn p-i-n photodiodes grown with low-temperature Chemical Vapour Deposition (CVD). The Double Heterostructure (DHS) p-i-n photodiodes were grown on a Si substrate using a thick strain relaxed, p-doped, Ge buffer as a virtual substrate. This was followed by the deposition of a 200nm unintentionally doped GeSn

film and an n-doped Ge cap layer. The Sn concentrations in the GeSn layer were measured as 6.1%, 6.4% and 9.2% using X-ray diffraction, with residual compressive strains of -0.5%, -0.4% and -0.5% respectively. The high crystal quality of the GeSn layers was confirmed using cross-sectional transmission electron microscopy. Further details of the growth can be found elsewhere. [141] The Sn concentrations correspond to the range of values where the contemporary literature predicts the indirect to direct band gap crossover to occur in GeSn. [41–44] As we explain below, due to band mixing effects it is more appropriate to discuss the band gap character rather than the indirect or direct nature of the band gap over a critical composition range. An important metric is the fractional Γ character, which describes here the proportion of the CBE state that projects onto Γ -like bulk Ge states. The band edge optical recombination rate, tunnelling rate and optical gain are all expected to increase monotonically with increasing Γ character. [120, 121, 129]

3.5.2 Absorption Coefficient and absorption edge

The absorption coefficient (α) describes the intensity attenuation of the light passing through a material and can be expressed as a summation of the absorption cross-sections per unit volume of a material for a given optical process. The higher the absorption coefficient α is, the shorter is the distance that the light penetrates into the material before it is absorbed. The absorption coefficient of a semiconductor is traditionally expressed using the relationship between absorption coefficient α and the photon energy $h\nu$ for the fundamental band gap of E_g as

$$\alpha \approx (h\nu - E_g)^n$$

where n has a value of 1/2 for a direct band gap transition and a value of 2 for indirect band gap transitions. [133] Using this relationship and the data from the photovoltage measurements undertaken on the $\text{Ge}_{1-x}\text{Sn}_x$ photodiodes the absorption edge for each cell could be determined from a plot such as that shown in Fig. 3.3. For this investigation of GeSn photodiodes absorption in the thin 50 nm Ge cap layer was assumed to be negligible and therefore neglected.

The band edge character of GeSn is determined here by measuring the pressure coefficient of the effective band edge. For the purpose of this work, the effective band edge refers to the aggregate effect of the low energy CB states, which determines the optical properties of GeSn. The pressure coefficient was determined by extracting the absorption spectrum from photovoltage measurements and measuring the energy shift of the band edge under high pressure. Photovoltage spectra were obtained using a lock-in-amplifier and a Bentham grating-based monochromator with an integrated light source to select wavelengths. The monochromated

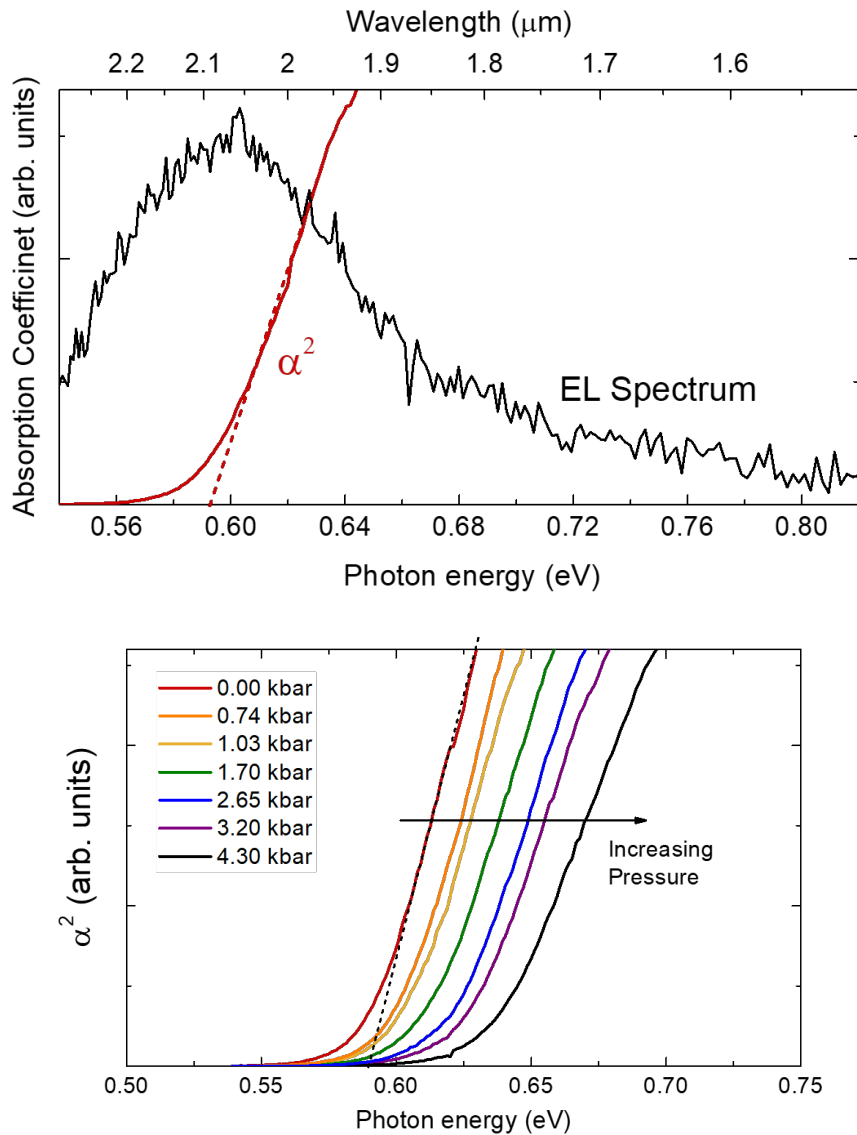


FIGURE 3.3: (a) Electroluminescence and the square of the absorption coefficient measured at atmospheric pressure for the $\text{Ge}_{0.936}\text{Sn}_{0.064}$ photodiode. (b) Absorption spectra (α^2) under hydrostatic pressure, measured at room temperature.

light was modulated using an optical chopper. The linewidth for each wavelength measurement was 10 nm. For the high-pressure measurements, the GeSn photodiodes were housed inside a CuBe pressure cell with light focused through a sapphire window onto the device. Hydrostatic pressures of up to 5 kbar were applied using a compression system with helium gas as the pressure medium. It is essential to have a strong band edge feature in the absorption spectrum which can be consistently measured under pressure. Taking the square of the absorption spectrum, plotted as a function of photon energy, and extrapolating the falling slope to the energy axis (Tauc equation [142]) gives good agreement with the peak of the electroluminescence spectrum measured at ambient pressure shown in Fig.3.3(a).

Due to the small aperture window in the high pressure cell, it was not possible to obtain electroluminescence under pressure owing to the low signal-to-noise ratio; however, this extrapolation procedure provides a strong and consistent method to establish the pressure coefficient of the effective band edge. Extrapolation of α^2 has been used previously in the literature to determine the compositional dependence of the direct band gap of GeSn. [101, 133] However, as revealed by the high pressure measurements detailed below, the compositional dependence of the absorption edge is somewhat more complex, and we find from the pressure coefficients that what is measured as direct gap absorption can actually be absorption from states with mixed Γ (direct) and L (indirect) character.

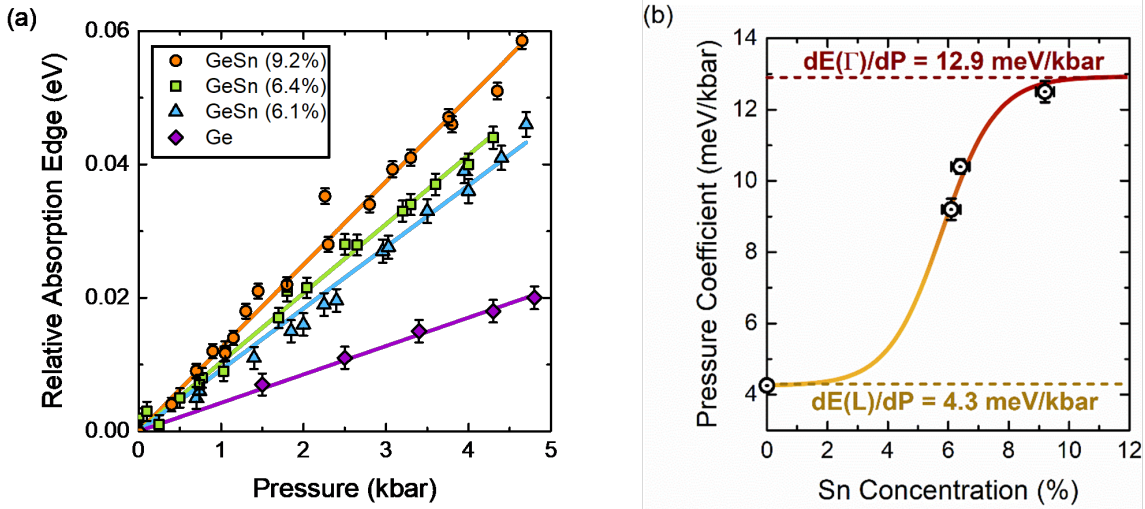


FIGURE 3.4: (a) The energy shift of α^2 as a function of pressure from atmospheric pressure for Ge and $\text{Ge}_{1-x}\text{Sn}_x$ photodiodes. The gradients of the pressure dependence give the pressure coefficients of the band edge, which are plotted as a function of Sn concentration in (b). The sigmoid plot is a guide to the eye.

3.5.3 Pressure coefficients

The method for determining the pressure coefficient of the effective band edge is illustrated in Figure 3.3(b). With increasing pressure, the absorption edge shifts to higher energies, due to the positive pressure coefficients associated with the Γ - and L- conduction band minima. At each pressure, we observe a strong linear region in the α^2 data. The measured relative shifts of the band edge as a function of pressure for the three GeSn photodiodes are presented in Figure 3.4(a). In each case, there is a strong linear relationship between the shift of the absorption edge and the applied pressure value. A pressure coefficient can therefore be reliably determined for each sample. For comparison, the movement of the absorption edge of a commercial Ge photodiode is presented. As can be seen from Figure 3.4(a) the pressure coefficient of 4.3 $\text{meV}\text{kbar}^{-1}$, derived for the Ge photodiode, is in good agreement with the pressure coefficient of the L conduction minima in pure Ge. The derived pressure coefficients of the GeSn photodiodes

are $9.2 \text{ meV}\text{kbar}^{-1}$, $10.4 \text{ meV}\text{kbar}^{-1}$ and $12.5 \text{ meV}\text{kbar}^{-1}$ for the 6.1%, 6.4% and 9.2% Sn samples, respectively.

There are a number of notable features in these results. Firstly, the pressure coefficient of $9.2 \text{ meV}\text{kbar}^{-1}$ for the 6.1 % Sn sample is just over midway between the L-point value ($4.3 \text{ meV}\text{kbar}^{-1}$) and the Γ direct gap value ($12.9 \text{ meV}\text{kbar}^{-1}$) of pure Ge. This provides evidence for substantial Γ character at the band edge in GeSn, even at a composition where the band gap is generally predicted to be indirect. The dominant Γ character of the band edge, even with such a low Sn concentration is, as we show below, evidence of CB mixing effects. Secondly, with increasing Sn concentration, there is a monotonic increase in the pressure coefficient of the band edge. Significantly, there is no sharp transition in the pressure coefficient with Sn concentration, as would be expected in conventional alloys such as GaAs [143], AlGaAs [144], InGaSb [145] and AlInAs [146]. Instead, we observe a continuous increase in the Γ character with Sn concentration. This evolution is illustrated in Figure 3.4 (b), which plots the pressure coefficient as a function of Sn concentration, illustrating the asymptotical approach of the GeSn pressure coefficient to that of the Γ conduction band minimum of Ge.

3.6 Density Functional Theory analysis

In this section we present the results of the DFT analysis undertaken on a series of ordered and disordered $\text{Ge}_{1-x}\text{Sn}_x$ supercells of varying Sn contents. This analysis is divided into two distinct segments; Section 3.6.1, where we analyze the dependence of the band gap in free-standing GeSn alloys, to gain insight into the fundamental electronic structure properties of these systems and section 3.6.2, where we analyze the pressure dependence of the conduction band edge states of $\text{Ge}_{1-x}\text{Sn}_x$ with varying composition x to gain insight into the key role of band mixing effects on the evolution of the band structure in $\text{Ge}_{1-x}\text{Sn}_x$ alloys with increasing % Sn content.

3.6.1 Band structure calculations: Pressure dependence of band gap

To analyze the pressure dependence of the band gap in free-standing GeSn alloys and to gain insight into the fundamental electronic structure properties of these systems from theory, we proceed in the following way. First, and key to this study, 16- and 64-atom supercells (SCs) have been chosen, for both of which the bulk Ge conduction band L and X states fold to the supercell Γ point. With these states folding back in this way, band mixing can then occur between Γ and the high symmetry L and X conduction band states. This is in contrast to previous DFT calculations where supercells have been chosen so as to exactly avoid this mixing, [124] or where mixing effects have not been considered in the analysis of the band structure.

[125] Moreover, and in line with the experimental considerations, it is important to understand how the electronic structure and therefore the $\Gamma - L$ conduction state mixing evolves with Sn content. Taking these two factors into account, Sn composition and $\Gamma - L$ conduction band state mixing, the following cells have been investigated in our theoretical analysis. To study very low Sn contents a 64 atom supercell has been constructed where one Ge atom is replaced by a Sn atom ($\text{Ge}_{63}\text{Sn}_1$). This leaves us with a system of only 1.56% Sn ($\text{Ge}_{0.9844}\text{Sn}_{0.0156}$). Given that the experimental data, Figure 3.4 (a), shows clear indication of $\Gamma - L$ state mixing for GeSn alloys with 6% Sn, we have primarily targeted this composition in the calculations. To analyze the importance of the alloy microstructure on the results for this composition, two different cells with nominally the same Sn content (6.25% Sn) have been generated. The first supercell is again a 64 atom supercell. Here, 4 Ge atoms have been substitutionally replaced at random by 4 Sn atoms ($\text{Ge}_{60}\text{Sn}_4$). In addition, we have considered a 16 atom supercell (face centred cubic (fcc) cell) with one Sn atom substitutionally replacing a Ge atom ($\text{Ge}_{15}\text{Sn}_1$). In this case, due to the small supercell size and the periodic boundary conditions, a very ordered arrangement of the Sn atoms has been constructed. Below we discuss in more detail the impact of the supercell size on the results. Using these cells, we have studied the composition and pressure dependence of the band gap energy E_g of the different systems. To do so, the structures have been initially relaxed (cell shape, volume and internal degrees of freedom of the atoms) to find the equilibrium lattice constant. To mimic the effect of pressure on the cell, the equilibrium lattice constant has been reduced and the internal atomic positions have been relaxed again at each pressure. Figure 3.5 shows the results of these calculations.

Following the experimental approach, we have calculated here the relative band gap change ΔE_g with pressure, meaning that the band gap shift with respect to the zero pressure data (equilibrium structure) is displayed. As a reference, we have performed the same calculation for a two atom, pure Ge cell. Again, this procedure is similar to the experimental setup. From the pure Ge cell the pressure dependence of the Ge band gap at the Γ -point, $\Delta E_{\Gamma}^{\text{Ge}}(\text{Bulk})$ (red filled squares), and the fundamental band gap, $\Delta E_L^{\text{Ge}}(\text{Bulk})$ (green filled diamonds), between the valence band edge (Γ_{8v} -state) and the conduction band edge at the L-point (L_{6c} -state), have been extracted. The pressure coefficient $(\frac{dE}{dP}(\Gamma))^{\text{theory}}$ for $\Delta E_{\Gamma}^{\text{Ge}}(\text{Bulk})$ is found to have a value of $(\frac{dE}{dP}(\Gamma))^{\text{theory}} = 13.3 \text{ meV/kbar}^{-1}$. For the indirect band gap $\Delta E_L^{\text{Ge}}(\text{Bulk})$ a pressure coefficient of $(\frac{dE}{dP}(L))^{\text{theory}} = 4.66 \text{ meV/kbar}^{-1}$ is calculated. These numbers are in very good agreement with the values $(\frac{dE}{dP}(\Gamma))^{\text{exp}} = 12.9 \text{ meV/kbar}^{-1}$, $(\frac{dE}{dP}(L))^{\text{exp}} = 4.34 \text{ meV/kbar}^{-1}$ given above. Starting with the 1.56% Sn data ($\text{Ge}_{0.9844}\text{Sn}_{0.0156}$, blue open circles) we find that the pressure dependence of the band gap energy at this very low Sn content ($4.75 \text{ meV/kbar}^{-1}$) is extremely close to the pressure coefficient of the indirect band gap of pure Ge (green filled diamonds in Fig. 3.4), confirming an indirect band gap at very low Sn content. However, when turning to the 6.25% Sn systems (magenta and black open triangles in Figure 3.5), the calculated band gap pressure dependence of the GeSn alloy shows very similar results when

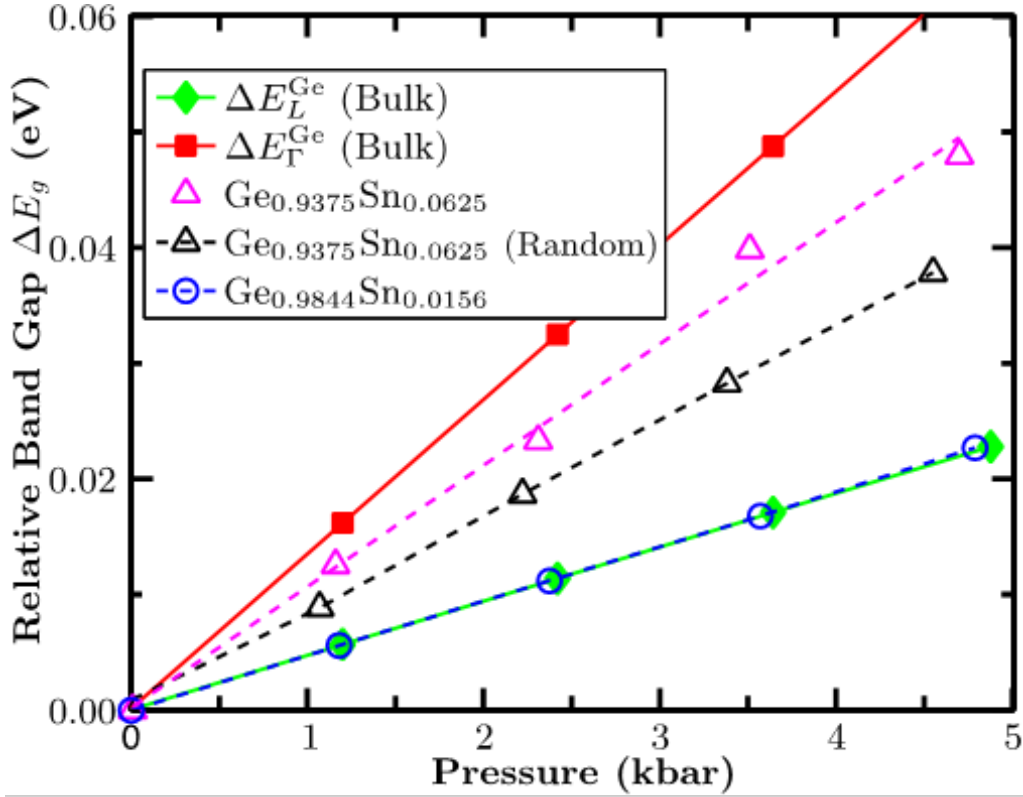


FIGURE 3.5: The relative band gap ΔE_g as a function of the applied pressure from hybrid-functional density functional theory calculation. Calculations have been performed for GeSn supercells with different Sn contents. As a reference, calculated data for pure Ge bulk systems are also given.

compared to the experimental data, cf. Figure 3.4 (a). A closer inspection of the 6.25% Sn system reveals that even though the 16 (magenta open triangles in 3.5) and the 64 (black open triangles) atom supercells have nominally the same Sn content, they exhibit clearly different pressure coefficients of $10.5 \text{ meV kbar}^{-1}$ and $8.2 \text{ meV kbar}^{-1}$, respectively. This highlights that the alloy microstructure and the supercell size noticeably affect the electronic structure of this system. This effect will be investigated and discussed further below, when band mixing effects are investigated in more detail.

Overall, the theoretical and experimental data show that by 6% Sn the alloy conduction band edge has strong Γ character ($> 50\%$ Γ in experiment and the 16-atom supercell; $> 40\%$ in the 64-atom supercell considered). Consequently, when accounting for the CB Γ -L state mixing in the calculations, our theoretical results are consistent with the experimental observation of a continuous transition from an indirect-to-direct band gap material. This aspect has been widely neglected in previous literature studies and sheds new light on the evolution of band gap in GeSn alloys with Sn content, clearly modifying the previous perception of a sharp indirect to direct band gap transition. [42, 124, 147, 148]

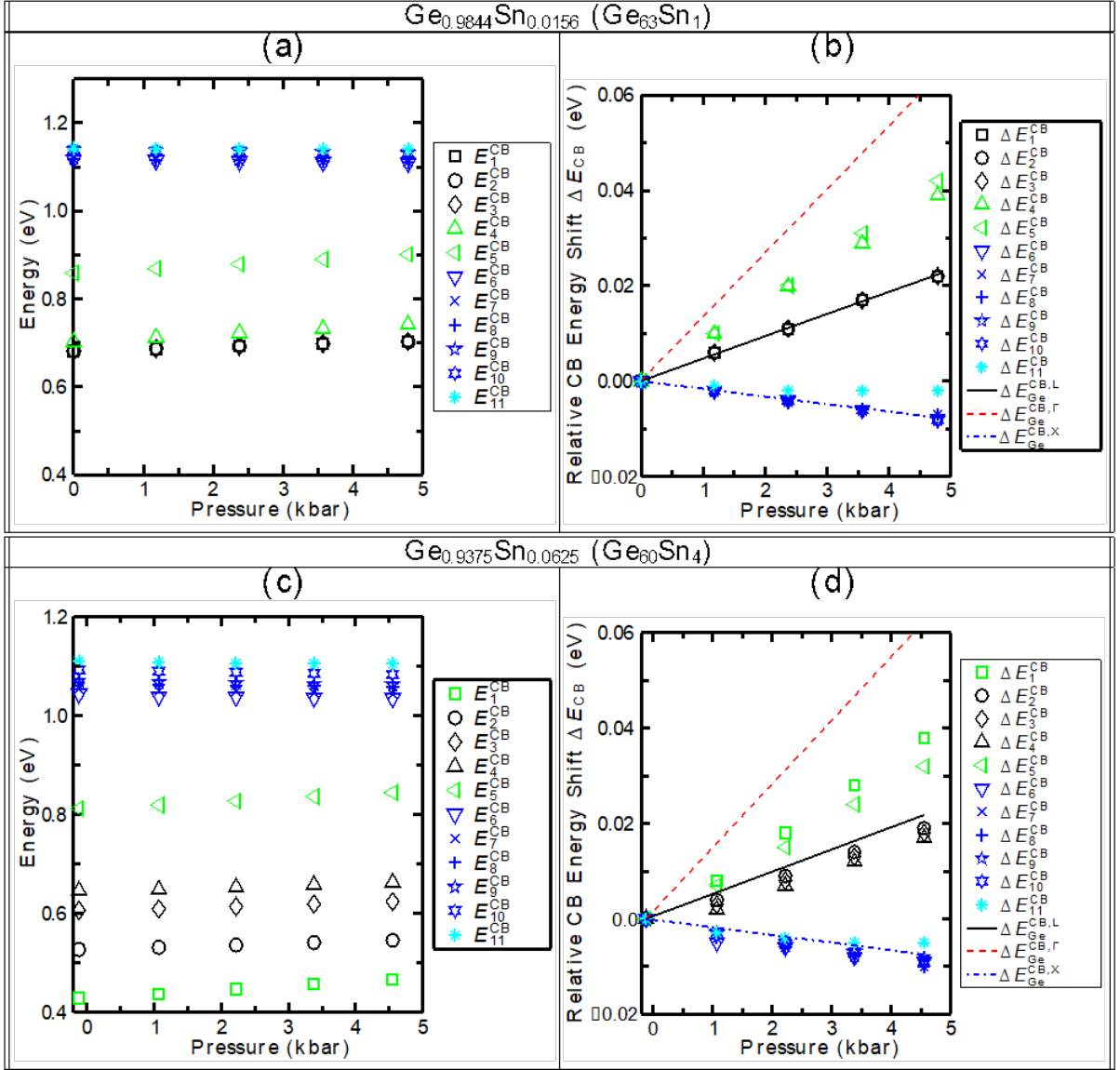


FIGURE 3.6: (a) Pressure dependence of the 11 energetically lowest zone centre conduction band (CB) states in $\text{Ge}_{0.9844}\text{Sn}_{0.0156}$ (64 atom supercell with 1 Sn and 63 Ge atoms, $\text{Ge}_{63}\text{Sn}_1$) with respect to the valence band (VB) edge energy. (b) Change in energies in conduction band states shown in (a) with pressure. Additionally, the pressure dependence of the pure Ge Γ - (red dashed), L- (black solid) and X- (blue dashed-dotted) gaps are also shown. (c) Same as (a) but for $\text{Ge}_{0.9375}\text{Sn}_{0.0625}$ (64 atom supercell with 4 Sn and 60 Ge atoms; Sn atoms randomly distributed; $\text{Ge}_{60}\text{Sn}_4$). (d) Same as in (b) for the $\text{Ge}_{0.9375}\text{Sn}_{0.0625}$ 64 atom supercell.

3.6.2 Band structure calculations: Band mixing effects

To further support this finding, we have studied the pressure dependence with respect to the VB edge of the first 11 CB states of the two 64 atom supercells considered here. The results of this study are displayed in Figure 3.6. The first row, Figure 3.6 (a) and (b), shows data for the 1.56% Sn system ($\text{Ge}_{63}\text{Sn}_1$). In Figure 3.6 (a) the energy separation of the energetically lowest 11 conduction band states with respect to the VB edge energy at each pressure is displayed. Figure 3.6 (b) depicts the relative energy shift of the conduction band states with applied

pressure. The results of the same analysis, but this time for the 6.25% Sn system, carried out with a random distribution of 4 Sn atoms in a 64 atom supercell ($\text{Ge}_{60}\text{Sn}_4$), are depicted in Figure 3.6 (c) and (d).

3.6.2.1 Band structure calculations: Band mixing effects at low Sn contents

We start with the analysis of the 1.56% Sn system (Figure 3.6 (a) and (b)). When looking at the relative energy positions of the different CB states with respect to the VB edge at each pressure, Figure 3.6 (a), we find that the first three conduction band states (ΔE_1^{CB} , ΔE_2^{CB} , ΔE_3^{CB}) are degenerate in energy. When looking at their pressure dependence, Figure 3.6 (b), these states exhibit the pressure dependence of the conduction band L-state in pure Ge (black solid line in Figure 3.6 (b)), consistent with the band gap data in Figure 3.5 for 1.56% Sn. Before turning to ΔE_4^{CB} , and ΔE_5^{CB} (triangles in Figure 3.6 (a)), we first look at ΔE_6^{CB} to ΔE_{11}^{CB} . Again, these states are almost degenerate in energy. Furthermore, they are energetically clearly separated from ΔE_1^{CB} to ΔE_5^{CB} . We attribute ΔE_6^{CB} to ΔE_{11}^{CB} to X-like states. This is confirmed by their pressure dependence, cf. Figure 3.6 (b), which follows closely the pressure dependence of the Ge bulk X CB states (blue dashed dotted line). A closer inspection of the pressure dependence of ΔE_{11}^{CB} (light blue stars) reveals a slightly larger pressure coefficient than the other X-like states ΔE_6^{CB} to ΔE_{10}^{CB} . Before looking at this behaviour in detail, we examine the pressure dependence of ΔE_4^{CB} and ΔE_5^{CB} first. Here, these two states exhibit pressure coefficients which are intermediate between the pressure coefficients of Ge bulk CB L (black solid) and Γ states (red dashed). In the supercells considered here, one expects in general 4 L-like states, with three having p-like symmetry about the Sn atom and one having s-like symmetry. Therefore ΔE_4^{CB} and ΔE_5^{CB} are a mixture of Γ and L states with s-like symmetry on the Sn site. Additionally, given that ΔE_{11}^{CB} shows a slight deviation from the pure Ge X-like bulk pressure dependence we expect also a contribution from this X-like state to ΔE_4^{CB} and ΔE_5^{CB} . The predicted mixing of the different states is further supported by the observation that the sum of the pressure coefficients of ΔE_4^{CB} , ΔE_5^{CB} and ΔE_{11}^{CB} is within 1 meV/kbar^{-1} of the sum of the pressure coefficients of the bulk Ge Γ , L and X states. Consequently, our data clearly indicate band mixing effects between s-like L, Γ and X conduction band states. However, for the Sn content of 1.56% the mixed states lie above the conduction band minimum, and the conduction band edge is still made up of states that are L-like in character. To understand the effect of increasing Sn content on band mixing effects and, thus, the connected consequences for the band gap of GeSn alloys, we turn now to the 64 atom supercell with a random distribution of 4 Sn atoms.

3.6.2.2 Band structure calculations: Band mixing effects at higher Sn contents

In comparison to the 1.56% Sn case, cf. Figure 3.6 (b), the striking difference in the 6.25% Sn case is that the lowest CB state (ΔE_1^{CB} , green squares), Figures 3.6 (c,d), has a pressure coefficient intermediate between the Ge bulk CB Γ (red dashed line) and L state (black solid line), with a second state, ΔE_5^{CB} (green triangles) also having an intermediate pressure coefficient. Again, this indicates Γ -L state mixing due to Sn incorporation in the supercell. Looking now at the other CB states, Figure 3.6 (c), ΔE_2^{CB} to ΔE_4^{CB} are all L state related, as confirmed by their pressure dependence, Figure 3.6 (d). Due to alloy disorder, their degeneracy is lifted. ΔE_6^{CB} to ΔE_{11}^{CB} are again X-like in character, with some mixing from Γ - and L-like states, as can be seen from their pressure dependence, Figure 3.6 (d). Our results on the 16 atom fcc SC with just 1 Sn atom, but nominally the same Sn content, give similar trends in the pressure dependence of the band gap as the 64-atom random alloy SC (cf. Figure 3.5). But, as one can infer from Figure 3.5, a higher pressure coefficient of the band gap is observed in the 16 atom fcc SC. We attribute this to the small SC size and the resulting long-range correlations (ordering) introduced by the periodic boundary conditions, which leads to increased Γ character for the lowest conduction state in the 16 atom fcc SC compared to the 64-atom random structure considered. This comparison highlights that further studies are required to understand the impact of the SC size on the CB mixing effects in full detail. To do so, systems with several hundred to thousands of atoms would need to be studied, in order to minimize the influence of long range ordering arising from the periodic boundary conditions of the simulation cell. However, systems of such size are beyond the capabilities of standard DFT approaches. Consequently, empirical models, such as the tight-binding or empirical pseudopotential method are required. However, these empirical methods have to be benchmarked against, for example, DFT results to obtain reliable results. Therefore, our presented HSE-DFT calculations not only provide new insight into the electronic structure of GeSn alloys, they can now also serve as a starting point for developing empirical models to study the electronic and optical properties of these systems. Overall, even without using these very large SCs, our calculations support that band mixing effects in GeSn alloys lead to a continuous evolution of the material from being an indirect band gap system to a direct one.

3.7 Chapter Summary

There are a number of interesting features arising from these results that are worth discussing. In this work we investigated the compositional dependence of the band gap character of GeSn alloys both from theory and experiment. On the experimental side, three GeSn alloy photodiodes were studied with Sn concentrations between 6% – 10%. The experimental approach uses

hydrostatic pressure to reversibly modify the electronic band structure of GeSn. The substantial difference in the conduction band pressure coefficients of Γ and L allow their contributions to the effective band edge to be determined under pressure. Measuring the effect of hydrostatic pressures on the absorption edge, we derived pressure coefficients of the effective band edge, as a function of Sn composition. Conventionally in Group IV and III-V binary and ternary alloy supercells the pressure coefficient of the conduction band edge is found to be purely composed of band gap character arising from a single conduction band critical point, such as Γ , L or X. In sharp contrast, the results of this investigation of dilute $\text{Ge}_{1-x}\text{Sn}_x$ alloys show that the pressure coefficients measured experimentally for the $\approx 6\%$ Sn photodiodes is intermediate between those of Γ and L in pure Ge, as shown in Fig. 3.3. The pressure coefficients measured for the two GeSn photodiode samples with $x \approx 6-7\%$ are in sharp contrast to the existing literature, which suggests there should be a sharp transition from a purely L-like (indirect gap) pressure coefficient to a purely Γ -like (direct gap) pressure coefficient after some critical Sn composition. The results indicate instead continuous evolution of Γ -character in the conduction band gap edge, as the band gap narrows as a function of Sn concentration. This monotonic increase of Γ character at the conduction band edge, whose pressure coefficient appears to asymptotically approach that of Γ in pure Ge, is indicative of band mixing effects in the alloy which have not generally been accounted for in the contemporary literature.

As a result of the presence of strong band mixing effects in the alloy the distinction between direct and indirect band gaps breaks down. It becomes instead more appropriate to discuss the nature of the band gap in terms of the fractional Γ character of the conduction band edge states. This fractional Γ character describes the extent to which the band edge state is composed of states arising from the Γ states of bulk Ge.

Further investigation of the impact of band mixing on the electronic properties of GeSn was performed here by calculating the band structure using hybrid functional DFT. These calculations further supported the experimentally observed band mixing effects and thus a continuous evolution of the band gap from being indirect to direct.

Band mixing effects have important implications for the viability of future electronic and photonic devices based on GeSn alloys. One consequence of band mixing is improved optical properties at lower Sn concentrations than would otherwise be expected. However, mixing and random alloy fluctuations may lead to an intrinsic inhomogeneous broadening of band edges. This would broaden the gain spectrum, requiring a higher carrier density for transparency and threshold. Interband tunnelling could likewise be enhanced at lower Sn concentrations but with inhomogeneous broadening reducing the rate at which current increases with voltage. In addition, strong mixing effects will increase electron scattering in conventional electronic devices, thereby reducing electron mobility compared to that expected using a virtual crystal

approximation. The composition dependence of mixing effects is not yet known and will be further investigated in the next chapter.

Chapter 4

Electronic and optical properties of GeSn alloys

4.1 Overview

In this chapter we present a theoretical analysis of electronic structure evolution in the group-IV alloy $\text{Ge}_{1-x}\text{Sn}_x$ with increasing content of x . We outline the theoretical density functional theory methods we use to investigate the alloy electronic structure in ordered and disordered supercells of $\text{Ge}_{1-x}\text{Sn}_x$. We find that Sn incorporation primarily impacts the conduction band (CB) structure while leaving the valence band relatively unperturbed. We demonstrate that, in addition to producing a strong reduction in the band gap and increase in the spin-orbit splitting energy per % Sn replacing Ge, Sn incorporation drives hybridisation of Ge states lying close in energy to the CB edge. The importance of alloy disorder in determining the details of the electronic structure is highlighted by tracking the character of the alloy CB edge eigenstates in response to the formation of a Sn-Sn nearest neighbour pair. Having established the requirement to explicitly consider alloy disorder, we analyse the electronic structure evolution in realistic (disordered) alloy supercells using a special quasi-random structure approach. In $\text{Ge}_{1-x}\text{Sn}_x$ alloys this analysis shows the continuous evolution of a direct band over a range of Sn compositions $x \lesssim 10\%$ due to strong Sn-induced band mixing.

In our work, we calculate that Sn incorporation results in a strong reduction of the fundamental band gap, by ≈ 34 meV per % Sn replacing Ge. Secondly, the band gap becomes direct in character with increasing x , but the alloy CB edge eigenstates in our supercell calculations are in general neither purely indirect nor direct in character, but predominantly contain an admixture of indirect (Ge L_{6c}) and direct (Ge Γ_{7c}) character.

Based on the HSE calculations, a semi-empirical valence force field (VFF) potential and sp^3s^* tight-binding (TB) Hamiltonian were parametrised by colleagues. Comparing the HSE, mBJ

and TB models, and using the HSE results as a benchmark, we demonstrate that: (i) mBJ calculations provide an accurate first principles description of the electronic structure at reduced computational cost, (ii) the VFF potential is sufficiently accurate to circumvent the requirement to perform first principles structural relaxation, and (iii) TB calculations provide a good quantitative description of the alloy electronic structure in the vicinity of the band edges. Our results also emphasise the importance of Sn-induced band mixing in determining the nature of the conduction band structure of $\text{Ge}_{1-x}\text{Sn}_x$ alloys. The theoretical models and benchmark calculations we present inform and enable predictive, computationally efficient and scalable atomistic calculations for disordered alloys and nanostructures. This provides a suitable platform to underpin further theoretical investigations of the properties of this emerging semiconductor alloy.

The remainder of this chapter is organised as follows. In Sec. 4.2 we describe the first principles framework used to calculate the structural and electronic properties of $\text{Ge}_{1-x}\text{Sn}_x$ alloy supercells, as well as the generation of the special quasi-random structures (SQSs) used in our analysis of disordered alloys. We also describe in this section how we use calculations of the band structure as a function of hydrostatic pressure to determine the hybridised character of the CB edge states. This is followed by an analysis of structural relaxation using our different models in Sec. 4.3. The results of our calculations are then presented, beginning in Sec. 4.4 with an analysis of the impact of Sn incorporation on the electronic structure of ordered $\text{Ge}_{1-x}\text{Sn}_x$ alloy supercells. In Sec. 4.5 we quantify the importance of Sn clustering, via analysis of the impact of nearest-neighbour Sn-Sn pair formation on the electronic structure. Then, in Sec. 4.6 we analyse the evolution of the electronic structure with x in realistic, disordered (SQS) alloy supercells. Finally, in Sec. 4.7 we summarise and conclude.

4.2 Theoretical Models

4.2.1 Summary of theoretical methods

In this section we outline the theoretical methods we utilise in this study of germanium-tin alloys, beginning by outlining the density functional theory (DFT) methods we have used, including a summary of how we have parameterised the DFT and which functionals have been utilised in this study. We then proceed to detail how the VFF and TB models developed by colleagues to investigate $\text{Ge}_{1-x}\text{Sn}_x$ alloys allow to extend from supercells containing only 10^2 atoms for HSE or mBJ DFT, up to systems of sizes as large 10^4 to 10^6 atoms. Following this we outline our choice of supercells and their impact on mixing effects in the alloy before detailing the special quasi random structures we have used for our investigation of the disordered alloy supercells.

4.2.2 First principles: hybrid functional and modified Becke-Johnson DFT

Our analysis of the $\text{Ge}_{1-x}\text{Sn}_x$ electronic structure is based on DFT calculations employing two distinct exchange-correlation (XC) functionals: (i) the Heyd-Scuseria-Ernzerhof (HSE) hybrid XC functional [78, 79] modified for solids (HSEsol), [134] and (ii) the modified Becke-Johnson (mBJ) XC functional. [75] The semi-core d states of Ge are treated as core electron states, since unfreezing these states has been demonstrated to have a negligible impact on the calculated electronic structure. [124] We therefore employ pseudopotentials in which the $(4s)^2(4p)^2$ orbitals of Ge and $(5s)^2(5p)^2$ orbitals of Sn are explicitly treated as valence states. Due to the large relativistic and consequent spin-orbit coupling effects associated with Sn [149], and to a lesser extent with Ge, all calculations explicitly include spin-orbit coupling. All DFT calculations were performed using the projector augmented-wave method, [85, 93] as implemented in the Vienna Ab-initio Simulation Package (VASP) [95, 96].

Since Sn incorporation is found to strongly impact the Ge band structure close in energy to the CB edge, and as we are interested in examining the transition from an indirect to direct band gap in $\text{Ge}_{1-x}\text{Sn}_x$ at low Sn compositions $x \lesssim 10\%$, we prioritise the accuracy of the description of the Ge band structure close in energy to the CB edge. For the HSEsol calculations we therefore treat the exact exchange mixing α as an adjustable parameter, the value of which is chosen to reproduce the 146 meV low temperature separation in energy between the measured 0.744eV fundamental indirect $L_{6c}-\Gamma_{8v}$ and 0.890eV direct $\Gamma_{7c}-\Gamma_{8v}$ band gaps of Ge. Similarly for the mBJ calculations the relative weight c of the conventional Becke-Johnson exchange potential is also treated as an adjustable parameter and chosen to reproduce the $\Gamma_{7c}-L_{6c}$ energy difference. A screening parameter of $\mu = 0.2 \text{ \AA}^{-1}$ was used in all of the HSEsol calculations.

For primitive unit cells we utilise a Γ -centred $6 \times 6 \times 6$ Monkhorst-Pack \mathbf{k} -point grid for Brillouin zone integration, which is downsampled appropriately for larger supercells in order to preserve the resolution of the Brillouin zone sampling. A plane wave cut-off energy of 400 eV is used for all calculations, which is chosen to be sufficiently high to minimise Pulay stress and allow for accurate structural relaxation. Structural relaxation is achieved via free energy minimisation, by allowing the lattice vectors and ionic positions to relax freely, subject to the additional criterion that the maximum force on any atom in the supercell does not exceed 0.01 eV \AA^{-1} . To generate relaxed atomic positions for HSEsol (mBJ) electronic structure calculations, the HSEsol (LDA) XC functional is used to perform structural relaxations. Due to the large relativistic effects associated with Sn [149], and to a lesser extent with Ge, spin-orbit coupling is explicitly included in the computation of the lattice free energy for all structural relaxations.

Using this Γ -centred $6 \times 6 \times 6$ Monkhorst-Pack \mathbf{k} -point grid for Brillouin zone integration in calculations for a Ge primitive unit cell, it was found that $\alpha = 0.3$ (i.e. 30% exact exchange mixing) produces indirect and direct band gaps of 0.765 and 0.908 eV. While these values

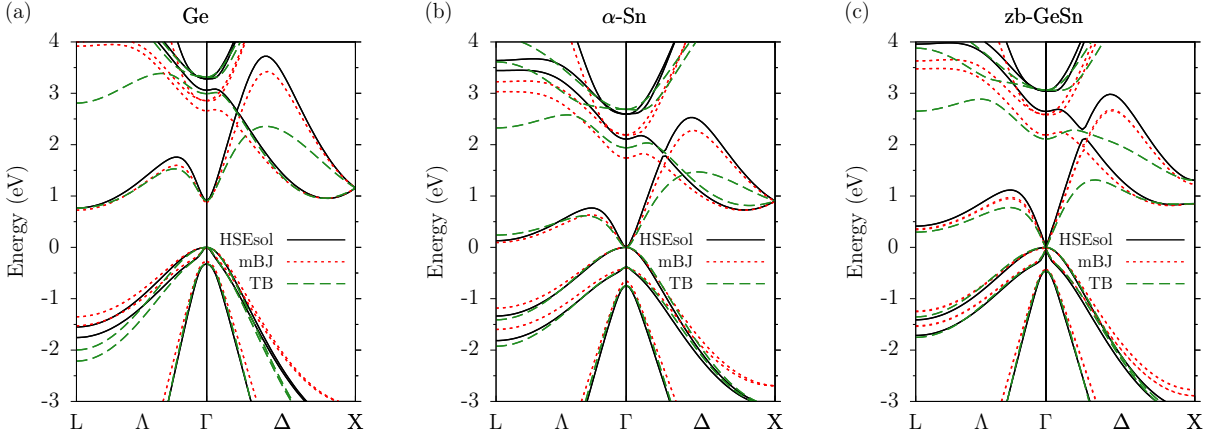


FIGURE 4.1: Band structure of (a) Ge, (b) α -Sn, and (c) zincblende GeSn (zb-GeSn), calculated via DFT, using the HSEsol (solid black lines) and mBJ (dotted red lines) exchange-correlation functionals, and via a semi-empirical sp^3s^* TB Hamiltonian (dashed green lines). All calculations include spin-orbit coupling. For comparative purposes, the zero of energy has been chosen to lie at the energy of the Γ_{8v} VB edge in all cases.

overestimate the measured band gaps by ≈ 20 meV, the corresponding Γ_{6c} - L_{6c} splitting of 143 meV is in excellent agreement with experiment. The calculated VB spin-orbit splitting energy for Ge is 0.322 eV, which again overestimates the measured value of 0.296 eV by 26 meV. Using the same settings for α -Sn we calculate a direct band gap of -0.382 eV compared to the measured value of -0.413 eV, and a spin-orbit splitting energy of 0.750 eV, which underestimates by 50meV, but is in good agreement with the measured valence band splitting of 0.800 eV.

For the mBJ calculations the same plane wave cut-off energy and \mathbf{k} -point grids were employed as for the HSEsol calculations, in order to allow the two approaches to be compared on an equal basis. In the mBJ calculations we again prioritise the description of the lowest CB in Ge: the parameter c in the mBJ exchange-correlation functional is treated as adjustable, and again chosen to reproduce the experimentally measured Γ_{6c} - L_{6c} splitting. Setting $c = 1.2$ produces indirect Γ_{8v} - L_{6c} and direct band gaps of 0.724 and 0.868 eV. While these band gaps are approximately 20 meV smaller than those measured experimentally, we note that the corresponding Γ_{6c} - L_{6c} splitting of 144 meV is in excellent agreement with experiment. The calculated VB spin-orbit splitting for Ge is 0.274 eV, underestimating the measured value by 22 meV. Using the same settings for α -Sn we calculate a direct band gap of -0.401 eV, within 12 meV of the measured value and a spin-orbit splitting energy of 0.651 eV which underestimates the measured value by 149meV. These values are again in reasonably good agreement with measured values.

The HSEsol- and mBJ-calculated band structures of Ge, α -Sn and zb-GeSn are shown, using solid black and dotted red lines respectively, in Figs. 4.1(a), 4.1(b) and 4.1(c). We note that, compared to the HSEsol XC functional, the mBJ XC functional tends to (i) overestimate the zone-centre effective mass of the lowest energy CB, (ii) underestimate the magnitude of the VB

spin-orbit splitting energy, and (iii) underestimate the energies of higher lying zone centre CB states.

4.2.3 Semi-empirical: valence force field potential and tight-binding Hamiltonian

The semi-empirical description of the structural and elastic properties of $\text{Ge}_{1-x}\text{Sn}_x$ alloys is based on a nearest-neighbour VFF potential. The VFF potential employed here is that originally introduced by Musgrave and Pople, [150] and later modified by Martin. [56] This potential is considered in its non-polar form, whereby the contribution to the lattice free energy associated with an atom located at site i is given by

$$\begin{aligned}
 V_i = & \frac{1}{2} \sum_j \frac{k_r}{2} \left(r_{ij} - r_{ij}^{(0)} \right)^2 \\
 & + \sum_j \sum_{k>j} \left[\frac{k_\theta}{2} r_{ij}^{(0)} r_{ik}^{(0)} \left(\theta_{ijk} - \theta_{ijk}^{(0)} \right)^2 \right. \\
 & \quad \left. + k_{rr} \left(r_{ij} - r_{ij}^{(0)} \right) \left(r_{ik} - r_{ik}^{(0)} \right) \right. \\
 & \quad \left. + k_{r\theta} \left(r_{ij}^{(0)} \left(r_{ij} - r_{ij}^{(0)} \right) + r_{ik}^{(0)} \left(r_{ik} - r_{ik}^{(0)} \right) \right) \left(\theta_{ijk} - \theta_{ijk}^{(0)} \right) \right], \quad (4.1)
 \end{aligned}$$

where the indices j and k describe the four nearest-neighbour atoms of atom i . The unstrained (equilibrium) and relaxed bond lengths between atoms i and j are denoted respectively by $r_{ij}^{(0)}$ and r_{ij} ; $\theta_{ijk}^{(0)}$ and θ_{ijk} respectively denote the unstrained and relaxed angles between the nearest neighbour bonds formed by atoms i and j , and i and k . The first and second terms in Eq. (4.1) respectively describe contributions to the free energy associated with bond stretching (changes in r_{ij}) and bond-angle bending (changes in θ_{ijk}), while the third and fourth terms are ‘‘cross terms’’ which respectively describe the impact of changes in r_{ik} on r_{ij} , and the impact of changes in θ_{ijk} on both r_{ij} and r_{ik} .

By firstly re-casting the lattice free energy calculated via Eq. (4.1) in terms of macroscopic and internal strains, and secondly inverting the associated derived expressions for the elastic constants C_{11} , C_{12} and C_{44} , and Kleinman (internal strain) parameter ζ , it has recently been demonstrated that the force constants k_r , k_θ , k_{rr} and $k_{r\theta}$ of this potential can be determined analytically. This circumvents the conventional requirement to perform numerical fitting to determine the force constants, and provides an exact description of the static lattice properties of the constituent materials Ge, α -Sn and zinc blende GeSn (zb-GeSn) in the linear elastic limit. The derivation of these analytical relationships is outlined in Tanner et al. [151]. The parameters used in the VFF structural relaxations are provided in Table 4.1. Full details of the

TABLE 4.1: Equilibrium bond lengths $r^{(0)}$, and force constants k_r , k_θ , k_{rr} and $k_{r\theta}$, used to implement structural relaxations using the VFF potential of Eq. (4.1) for $\text{Ge}_{1-x}\text{Sn}_x$ alloy supercells. Force constants have been computed analytically based on HSEsol calculated structural properties for Ge, α -Sn and zb-GeSn.[151, 152]

Parameter	Unit	Ge	α -Sn	zb-GeSn
$r^{(0)}$	\AA	2.445	2.813	2.632
k_r	eV \AA^{-2}	7.0414	6.5920	7.7970
k_θ	$\text{eV \AA}^{-2} \text{ rad}^{-2}$	0.5104	0.2594	0.3375
k_{rr}	eV \AA^{-2}	0.2416	-0.1246	-0.2369
$k_{r\theta}$	$\text{eV \AA}^{-2} \text{ rad}^{-1}$	0.3005	0.0430	-0.0753

parametrisation of Eq. (4.1) based on HSEsol calculations are provided in [152]. To perform structural relaxations for $\text{Ge}_{1-x}\text{Sn}_x$ alloy supercells this VFF potential was implemented using the General Utility Lattice Program (GULP) where, as in the DFT calculations described above, the structural relaxation proceeds by minimising the lattice free energy.

The semi-empirical electronic structure calculations for $\text{Ge}_{1-x}\text{Sn}_x$ alloys are based on a nearest-neighbour sp^3s^* TB Hamiltonian, and include spin-orbit coupling. The unstrained band structures of Ge, α -Sn and zb-GeSn are parametrised based on those calculations using the HSEsol formalism described in Sec. 4.2. As with the HSEsol and mBJ DFT calculations, the priority in generating a TB fit to the Ge band structure is to provide an accurate description of the lowest CB, in terms of the energies of the CB edge states at the L , Γ and X points in the Brillouin zone. For this, the fitting procedure outlined in [153], which relates the TB parameters to the energies at the Γ and X points, is followed and then the resulting parameters are adjusted to achieve an exact fit to the energies of the L_{6c} , Γ_{6c} and X_{6c} CB edge states. For the α -Sn band structure the fitting procedure of [153] is applied without modification, which is found to provide a good overall fit to the HSEsol band structure.

Key to describing the impact of Sn incorporation on the electronic structure of $\text{Ge}_{1-x}\text{Sn}_x$ alloys is the TB fit to the band structure of a zb-GeSn primitive unit cell. Such a fitting allows for an accurate description of the interaction between orbitals situated on neighbouring Ge and Sn atoms in alloy supercell calculations. To generate a suitable set of TB parameters for zb-GeSn we again begin with the procedure outlined in [153]. Following this procedure provides a good overall fit to the HSEsol-calculated zb-GeSn band structure, but it was found that these parameters tend to underestimate the impact of Sn incorporation in $\text{Ge}_{1-x}\text{Sn}_x$ alloy supercell calculations. To rectify this the differences in the free atomic orbital energies, which are used to determine the Ge and Sn atomic orbital energies in the zb-GeSn TB Hamiltonian are adjusted. [153] In doing so, a more accurate description of the impact of Sn incorporation is obtained compared to first principles calculations, while simultaneously maintaining a good overall fit to the HSEsol-calculated zb-GeSn band structure.

TABLE 4.2: Lattice constant a , direct Γ_{7c} - Γ_{8v} band gap E_g and VB Γ_{8v} - Γ_{7v} spin-orbit splitting energy Δ_{SO} for Ge, diamond-structured Sn (α -Sn) and zinc blende GeSn (zb-GeSn), calculated via DFT using the HSEsol (with $\alpha = 0.3$), and LDA (for a) or mBJ (with $c = 1.2$, for E_g and Δ_{SO}) XC functionals, and compared to low-temperature experimental measurements and previous first principles theoretical calculations. For Ge the fundamental (indirect) L_{6c} - Γ_{8v} band gap is listed in parentheses.

Material	a (Å)			E_g (eV)			Δ_{SO} (eV)		
	HSEsol	LDA	Reference	HSEsol	mBJ	Reference	HSEsol	mBJ	Reference
Ge	5.653	5.649	5.657 ^a , 5.648 ^b	0.908 (0.765)	0.868 (0.724)	0.890 (0.744) ^c	0.322	0.274	0.296 ^c
α -Sn	6.496	6.483	6.489 ^a	-0.382	-0.401	-0.413 ^d	0.750	0.651	0.800 ^d
zb-GeSn	6.079	6.074	6.127 ^e , 6.032 ^f	0.040	0.007	0.085 ^f	0.460	0.424	0.480 ^g

^aMeasured average Ref. [32], ^bCalc. average [32], ^cRef. [155], ^dRef. [137], ^eCalc. average Refs. [33, 156–158], ^fRef. [33]

4.2.4 Primitive Ge, Sn and zincblende-GeSn DFT benchmarks

Table 4.2 summarises the results of the DFT calculations for the three constituent crystalline materials relevant to $\text{Ge}_{1-x}\text{Sn}_x$ – diamond-structured semiconducting Ge ($x = 0$), diamond-structured [154] α -Sn ($x = 1$), and the fictitious semimetallic zinc blende-structured IV-IV compound GeSn (zb-GeSn; $x = 0.5$). The table lists calculated lattice constants a , direct band gaps E_g , and valence band (VB) spin-orbit splitting energies Δ_{SO} , compared to (low temperature) experimental measurements and previous theoretical calculations. The band structures of Ge, α -Sn and zb-GeSn, calculated using the HSEsol (solid lines) and mBJ (dashed lines) XC functionals, are also shown respectively in fig 4.1. We note that zb-GeSn – equivalent to an ordered $\text{Ge}_{0.5}\text{Sn}_{0.5}$ alloy – is close to semimetallic, with a very small predicted direct band gap of 0.040 eV (0.007 eV) in the HSEsol (mBJ) calculation, suggesting that the band gap in $\text{Ge}_{1-x}\text{Sn}_x$ alloys can be expected to close for some Sn composition near or below 50% and that the indirect to direct band gap transition should occur at a much lower % Sn composition.

4.2.5 Choice of alloy supercells

Emerging theoretical [124] and experimental [131, 159] evidence suggests the possibility of strong Sn-induced hybridisation of the Ge Γ_{7c} and L_{6c} CB edge states in $\text{Ge}_{1-x}\text{Sn}_x$. In a real alloy, all states that can (by symmetry) mix will mix: this physical effect will manifest in electronic calculations regardless of the choice of supercell. For example, Eckhardt et al. [124] noted the presence of strong Sn-induced Γ_{7c} - L_{6c} mixing, but subsequently chose to analyse supercells in which the L points do not fold to the supercell zone centre ($\mathbf{K} = 0$), to block this mixing and simplify their interpretation of the indirect- to direct-gap transition. However, unfolded band structures presented by Polak et al. [135] for the same supercells revealed clear signatures of Sn-induced band mixing, occurring instead with states along the Λ direction which did fold to $\mathbf{K} = 0$. That is, the choice to specifically neglect Γ_{7c} - L_{6c} mixing does not remove Sn-induced mixing of Ge states lying close in energy to the CB edge.

In the case of $\text{Ge}_{1-x}\text{Sn}_x$, we note that (i) the alloy CB edge originates from the Ge L_{6c} states, and (ii) we are interested in the acquisition of direct Ge Γ_{7c} character by the alloy CB edge. These observations suggest that there does not exist sufficient physical justification to explicitly neglect Γ_{7c} - L_{6c} mixing – which can be expected to be pronounced based on the small separation in energy of these states – in the analysis of the $\text{Ge}_{1-x}\text{Sn}_x$ electronic structure. We therefore choose supercells in which the L points in the primitive unit cell Brillouin zone of the underlying diamond lattice fold to the supercell zone centre $\mathbf{K} = 0$. This is the case in $n \times n \times n$ face-centred cubic (FCC) and simple cubic (SC) supercells for even values of n . As such, we employ $2 \times 2 \times 2$ FCC (16-atom) and SC (64-atom) supercells in our alloy electronic structure calculations.

We note that in supercells where L and X do not fold back to the origin, such as in the 54 atom case, L and Γ do not mix with each other. Points close to L and X will however fold back to the origin, with states two-thirds of the way from Γ to L and from Γ to X folding back in the 54 atom case. Supercell calculations carried out by a colleague (Amy Kirwan) show that the pressure coefficients of these states are very close to those of the states at the L and X point. These states will still provide the lowest energy conduction states at Γ in the 54-atom supercell and are therefore available to mix with the Γ state, to which they are close in energy. Consequently, a very similar pressure coefficient analysis could be undertaken in such supercells to analyse the character of the lowest conduction band states in the alloy. However, the Γ state is the lowest conduction state at the zone centre in the 54-atom Ge supercell, with the states which are two thirds of the way to L and to X lying higher in energy. This inversion of the order of the direct and indirect gap states may then have a quantitative impact on the results and analysis of mixing in small supercells where L and X do not fold back to the origin.

4.2.6 Generation of special quasi-random structures

To investigate the electronic structure of more realistic, disordered $\text{Ge}_{1-x}\text{Sn}_x$ alloys we employ a series of 128-atom ($4 \times 4 \times 4$ FCC) SQSs, containing up to 19 Sn atoms i.e. Sn compositions up to $x = 14.8\%$. The SQSs are generated stochastically, using a Monte Carlo simulated annealing procedure – implemented in the Alloy Theoretic Automated Toolkit (ATAT) [160, 161] using the mcsqs routine [162]. This routine optimises the supercell lattice correlation functions associated with pairs and triplets up to third nearest-neighbour distance about each lattice site, with respect to the target lattice correlation functions for a randomly disordered, diamond-structured alloy of a specified Sn composition x [163, 164]. Analysis of the evolution of the number of Sn-Sn pairs in the supercell with increasing Sn composition is presented in Sec.4.6.

4.2.7 Hydrostatic pressure coefficients

States originating from different wave vectors \mathbf{k} in the Brillouin zone of the primitive unit cell of the underlying diamond lattice are folded back to the zone centre ($\mathbf{K} = 0$) in supercell calculations. It can therefore be difficult to identify the character of individual zone-centre states in the band structure of a $\text{Ge}_{1-x}\text{Sn}_x$ supercell, and hence to deduce the composition at which the alloy becomes a direct-gap semiconductor. To address this issue, we investigate how the alloy CB structure changes as hydrostatic pressure is applied to the alloy supercell. As noted in chapter 3 the pressure coefficients $\frac{dE_g}{dP}$ for the indirect $L_{6c}-\Gamma_{8v}$ and direct $\Gamma_{7c}-\Gamma_{8v}$ band gaps of Ge are significantly different to one another, having respective values 4.66 and 13.33 meV kbar^{-1} in our HSEsol calculations, and 4.07 and 13.23 meV kbar^{-1} in our mBJ calculations. Calculation of $\frac{dE_g}{dP}$ for the fundamental band gap in a given alloy supercell then allows to identify the character of the band gap, and hence to track the evolution of the character of the CB edge states and band gap with increasing Sn composition x .

4.3 Ordered and disordered alloy supercells

4.3.1 Summary of content

Having outlined the theoretical models we have established to calculate the structural and electronic properties of $\text{Ge}_{1-x}\text{Sn}_x$ alloys, we now turn our attention to the application of these models in alloy supercell calculations. We compare and contrast the results of calculations carried out using all three models, reaffirming key features of the alloy properties and establishing the accuracy of the models. We begin in Sec. 4.3 by considering structural relaxation, before considering key features of ordered and disordered alloy supercell band structures in Sec. 4.4. In Sec. 4.5 we investigate how the separation of Sn atoms in disordered alloy supercells impacts the alloy electronic band structure. Then in Sec. 4.6 we consider how the electronic structure evolves with x in realistic, disordered $\text{Ge}_{1-x}\text{Sn}_x$ special quasi-random structures. Finally in Sec. 4.7 we summarise the main findings of this chapter.

4.3.2 Structural relaxation - Alloy lattice constant

Using the HSEsol calculations described in Sec. 4.2.2 we calculate (unstrained) lattice constants $a = 5.646, 6.496$ and 6.079 Å for Ge, α -Sn and zb-GeSn, respectively. The calculated lattice constant for Ge is in exact agreement with that determined via x-ray diffraction measurements, is slightly lower than the average value of 5.657 Å obtained by compiling a range of experimental data, and lies within the range of values 5.535 – 5.760 Å computed using various first principles approaches. For α -Sn the calculated lattice constant is close to the value of 6.489 Å determined

via x-ray diffraction measurements. The calculate lattice constant for the fictitious IV-IV compound zb-GeSn lies within the range of values 6.054 – 6.200 Å calculated using various first principles approaches. [33, 156–158] The LDA-calculated lattice constants for Ge, α -Sn and zb-GeSn are 5.647, 6.483 and 6.074 Å. These lattice constants for Ge and α -Sn are in good quantitative agreement with those obtained from HSEsol calculations. We note that the LDA is generally known to overbind systems compared to more advanced exchange-correlation functionals, leading in general to smaller equilibrium lattice constants, reflected here in the slightly smaller calculated lattice constants for α -Sn and zb-GeSn compared to the HSEsol values.

The physical properties, including band gaps and lattice constants, of many binary semiconductor alloys A_xB_{1-x} vary in a non-linear manner as a function of the alloy composition x , which can often be described by a second-order polynomial of the form shown below in equation 4.2.

$$a_{Sn_xGe_{1-x}} = xa_{Sn} + (1-x)a_{Ge} + bx(1-x) \quad (4.2)$$

In equation 4.2 b is the bowing parameter and a is the lattice constant. By replacing the lattice constant a in equation 4.2 with the direct band gap E_g , a similar expression can then be obtained for the optical gap.

Recent first principles calculations suggested the presence of an unusual negative bowing parameter for the lattice constant [124] – i.e. that the alloy lattice constant is larger than that obtained by interpolating linearly between the lattice constants of Ge and α -Sn. We find here that the HSEsol-calculated zb-GeSn lattice constant is slightly in excess of, but extremely close to, the average value 6.071 Å of those calculated for Ge and α -Sn. This appears to suggest that the $Ge_{1-x}Sn_x$ lattice constant possesses a small, negative bowing parameter. However, we note that such bowing parameters have to date only been extracted on the basis of calculations performed on small, ordered alloy supercells at low Sn compositions $x \lesssim 10\%$ and have not included alloy disorder effects. Further analysis which considers alloy disorder effects to quantitatively describe the evolution of the structural properties across the full Sn composition range is provided later in this chapter in Sec. 4.6.

TABLE 4.3: Relaxed lattice constant a and Ge-Sn nearest-neighbour bond length $r_{\text{Ge-Sn}}$, for a series of ordered and disordered $\text{Ge}_{1-x}\text{Sn}_x$ alloy supercells relaxed via DFT using HSEsol and LDA XC functionals, and via the semi-empirical VFF potential of Eq. (4.1) (parametrised using HSEsol-calculated lattice and elastic constants for Ge, α -Sn and zb-GeSn). The equilibrium lattice constant of Ge – calculated using the HSEsol and LDA approaches, and taken as input to the VFF potential – are provided for reference. For the disordered $\text{Ge}_{60}\text{Sn}_4$ supercell $r_{\text{Ge-Sn}}$ refers to the average length of all relaxed Ge-Sn bonds; values listed in parentheses are the standard deviations associated with these averaged values.

Supercell	x (%)	Description	a (Å)			$r_{\text{Ge-Sn}}$ (Å)		
			HSEsol	LDA	VFF	HSEsol	LDA	VFF
Ge	—	Pure Ge	5.646	5.647	5.646	—	—	—
$\text{Ge}_{63}\text{Sn}_1$	1.56	Ordered SC	5.661	5.664	5.658	2.574	2.578	2.558
$\text{Ge}_{15}\text{Sn}_1$	6.25	Ordered FCC	5.702	5.703	5.694	2.554	2.554	2.544
$\text{Ge}_{60}\text{Sn}_4$	6.25	Disordered SC	5.701	5.700	5.694	2.583 (0.010)	2.584 (0.010)	2.563 (0.010)

4.3.3 Internal relaxation: ordered supercells

Table 4.3 compares the relaxed supercell lattice constants a and relaxed bond length $r_{\text{Ge-Sn}}$ between nearest-neighbour Ge and Sn atoms obtained via HSEsol, LDA and VFF relaxations of a number of specific $\text{Ge}_{1-x}\text{Sn}_x$ alloy supercells of varying % x content. Specifically, we consider three distinct $2 \times 2 \times 2$ SC and FCC supercells: (i) an ordered 64-atom $\text{Ge}_{63}\text{Sn}_1$ SC supercell having $x = 1.56\%$, (ii) an ordered 16-atom $\text{Ge}_{15}\text{Sn}_1$ FCC supercell having $x = 6.25\%$, and (iii) a disordered 64-atom $\text{Ge}_{60}\text{Sn}_4$ SC supercell having $x = 6.25\%$. The four Sn atoms in the $\text{Ge}_{60}\text{Sn}_4$ were substituted at randomly selected sites on the lattice of the Ge_{64} host matrix supercell. We note that this disordered supercell contains a Sn-Sn “pair” – i.e. two Sn atoms which are nearest neighbours. The ordered $\text{Ge}_{15}\text{Sn}_1$ and disordered $\text{Ge}_{60}\text{Sn}_4$ supercells have the same Sn composition, thereby allowing the importance of alloy disorder effects in determining the material properties to be inferred via comparison of the results of calculations carried out for each.

We note that the A_1 -symmetric relaxation about the Sn lattice site in the ordered supercells produces four Ge-Sn nearest-neighbour bonds of equal length. Due to the presence of multiple Ge-Sn nearest-neighbour bonds and broken symmetry in the disordered $\text{Ge}_{60}\text{Sn}_4$ supercell, it is not possible to unambiguously assign a single value to $r_{\text{Ge-Sn}}$. We instead assign $r_{\text{Ge-Sn}}$ as the average of all of the relaxed Ge-Sn bond lengths in the supercell, and quantify deviations from this average using the standard deviation $\sigma(r_{\text{Ge-Sn}})$ of the relaxed Ge-Sn bond lengths (listed in parentheses in Table 4.3). A more general comparison of the HSEsol, LDA and VFF relaxations for this disordered supercell is provided in Fig. 4.2.

Beginning with the ordered $\text{Ge}_{63}\text{Sn}_1$ and $\text{Ge}_{15}\text{Sn}_1$ supercells, the HSEsol relaxation results in respective increases of 0.015 and 0.056 Å in the lattice constant compared to that of unstrained Ge (cf. Table 4.3). In both cases these relaxed lattice constants a slightly exceed those calculated based on a linear interpolation of the HSEsol-calculated Ge and α -Sn lattice constants, again

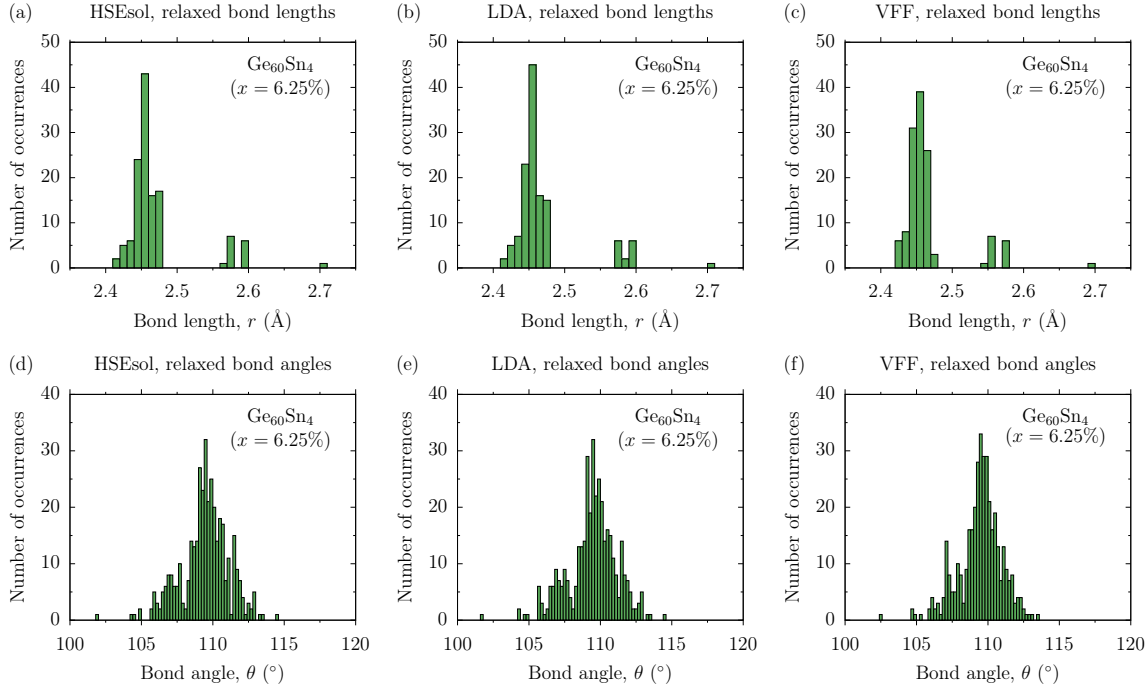


FIGURE 4.2: Comparison of first principles and semi-empirical relaxations of the atomic positions for a disordered $\text{Ge}_{60}\text{Sn}_4$ ($x = 6.25\%$) supercell containing a Sn-Sn nearest-neighbour pair. Top row: relaxed nearest-neighbour bond lengths r obtained from (a) HSEsol, (b) LDA, and (c) VFF minimisations of the lattice free energy. Bottom row: relaxed bond angles – formed by adjacent pairs of nearest-neighbour bonds – obtained from (d) HSEsol, (e) LDA, and (f) VFF minimisations of the lattice free energy. Relaxed bond lengths and angles have been sorted into bins of width $\Delta r = 0.01 \text{ \AA}$ and $\Delta\theta = 0.2^\circ$ respectively.

suggesting the presence of a small, negative bowing parameter for a . Relaxing these supercells in the LDA yields respective increases of 0.017 and 0.056 \AA in a for the $\text{Ge}_{63}\text{Sn}_1$ and $\text{Ge}_{15}\text{Sn}_1$ supercells. While the calculated increase in a for the $\text{Ge}_{15}\text{Sn}_1$ supercell precisely matches that obtained from the HSEsol calculation, the LDA relaxation overestimates the increase in a due to Sn incorporation in the larger $\text{Ge}_{63}\text{Sn}_1$ supercell. This behaviour is somewhat surprising: the LDA-calculated zb-GeSn lattice constant is smaller than that obtained from HSEsol calculations, upon which basis it could be expected that nearest-neighbour Ge-Sn bonds relax to shorter lengths in LDA calculations. In spite of this, the LDA-relaxed lattice constants show very close agreement with the HSEsol values: the differences between the LDA and HSEsol relaxed lattice constants are, respectively, only 0.05 and 0.02% for the $\text{Ge}_{63}\text{Sn}_1$ and $\text{Ge}_{15}\text{Sn}_1$ supercells. Relaxing these same supercells using the VFF potential of Eq. (4.1), parametrised based on HSEsol-calculated lattice and elastic constants, the corresponding calculated increases in a for $\text{Ge}_{63}\text{Sn}_1$ and $\text{Ge}_{15}\text{Sn}_1$ are 0.012 and 0.048 \AA . These values are in excellent agreement with the HSEsol relaxation: for $\text{Ge}_{63}\text{Sn}_1$ and $\text{Ge}_{15}\text{Sn}_1$ the respective differences between the VFF and HSEsol relaxed lattice constants are only 0.05 and 0.14% . Overall, for these ordered supercells we note that the LDA and VFF structural relaxations faithfully reproduce a obtained from a HSEsol relaxation but, nevertheless, the LDA (VFF) relaxation tends to overestimate (underestimate) the increase in a associated with substitutional Sn incorporation.

Considering now the relaxed Ge-Sn nearest-neighbour bond lengths (cf. Table 4.3), we calculate $r_{\text{Ge-Sn}} = 2.574$ and 2.554 Å in HSEsol relaxations of the $\text{Ge}_{63}\text{Sn}_1$ and $\text{Ge}_{15}\text{Sn}_1$ supercells. Compared to the unstrained Ge nearest-neighbour bond length $r_{\text{Ge}}^{(0)} = 2.445$ Å, these bond lengths represent respective increases of 0.129 and 0.109 Å. This result is initially surprising: the relaxed lattice constants obtained from the HSEsol relaxation exhibit the opposite trend, with the increase in a for the $\text{Ge}_{63}\text{Sn}_1$ supercell exceeding that calculated for $\text{Ge}_{15}\text{Sn}_1$. Further analysis reveals that this behaviour arises from the significantly smaller volume of the $\text{Ge}_{15}\text{Sn}_1$ supercell, in which Sn incorporation is accommodated by an increase in the average relaxed Ge-Ge bond length $r_{\text{Ge-Ge}}$. For the $\text{Ge}_{63}\text{Sn}_1$ and $\text{Ge}_{15}\text{Sn}_1$ supercells we respectively calculate $r_{\text{Ge-Ge}} = 2.448$ and 2.457 Å. The LDA relaxations of these ordered supercells produce respective relaxed Ge-Sn bond lengths which are increased by 0.133 and 0.109 Å compared to the corresponding LDA-calculated equilibrium Ge bond length. The corresponding increases in the VFF relaxations of these supercells are 0.113 and 0.099 Å. Using the HSEsol-calculated values as a reference, the computed differences in the LDA-relaxed values $r_{\text{Ge-Sn}}$ for the $\text{Ge}_{63}\text{Sn}_1$ and $\text{Ge}_{15}\text{Sn}_1$ supercells are, respectively, 0.15 and 0.01%. The corresponding differences between the HSEsol and VFF relaxed Ge-Sn nearest-neighbour bond lengths for these supercells are 0.6 and 0.4%.

4.3.4 Internal relaxation: disordered supercell

Turning to the disordered $\text{Ge}_{60}\text{Sn}_4$ supercell, we note that the relaxed lattice constants obtained from the HSEsol and LDA relaxations are slightly lower than those computed for the ordered $\text{Ge}_{15}\text{Sn}_1$ supercell having the same Sn composition. This slight reduction in relaxed lattice constant in the presence of alloy disorder is likely related to the volume effect described above, whereby the larger surrounding Ge matrix in a 64-atom supercell provides more surrounding volume for expansion to accommodate the local strain introduced by Sn incorporation. The average relaxed Ge-Sn nearest-neighbour bond length $r_{\text{Ge-Sn}} = 2.583 \pm 0.010$ Å for this disordered supercell is significantly larger than that calculated for either of the ordered supercells. This is in part a result of the presence of a Sn-Sn nearest-neighbour pair in the supercell, the large local expansion of the lattice associated with which leads to larger relaxed Ge-Sn bond lengths about these two Sn atoms. Examining Table 4.3, we note that this general trend is also observed in the LDA and VFF relaxations. However, the averaged nearest-neighbour bond lengths presented in Table 4.3 are insufficient in general to quantify the lattice relaxation in a disordered supercell. Thus, we present in Fig. 4.2 a more comprehensive view of the HSEsol, LDA and VFF relaxations of the $\text{Ge}_{60}\text{Sn}_4$ supercell. The top (bottom) row of Fig. 4.2 shows the relaxed bond lengths (angles) in the $\text{Ge}_{60}\text{Sn}_4$ supercell, sorted into bins of width $\Delta r = 0.01$ Å ($\Delta\theta = 0.2^\circ$). Panels (a) and (d), (b) and (e), and (c) and (f) respectively show the distributions of relaxed bond lengths and angles obtained from the HSEsol, LDA and VFF relaxations.

Examining firstly the HSEsol results in Figs. 4.2(a) and (d), we note the distribution of bond lengths brought about by the presence of alloy disorder. The three distinct peaks in the distribution of relaxed bond lengths in Fig. 4.2(a) describe, in order of increasing bond length, relaxed Ge-Ge, Ge-Sn and Sn-Sn bonds. The width of the distribution of Ge-Ge bonds is strongly enhanced compared to that in the ordered $\text{Ge}_{63}\text{Sn}_1$ supercell: the computed standard deviation of the relaxed Ge-Ge bond lengths in the $\text{Ge}_{60}\text{Sn}_4$ supercell is 0.014 \AA , compared to 0.006 \AA in the $\text{Ge}_{63}\text{Sn}_1$ supercell. As described above, the reduction in symmetry associated with the presence of alloy disorder also generates a distribution of relaxed Ge-Sn bond lengths, the standard deviation of which we compute to be 0.01 \AA . The single Sn-Sn bond in the supercell has a relaxed bond length $r_{\text{Sn-Sn}} = 2.704 \text{ \AA}$, an increase of 0.259 \AA compared to $r_{\text{Ge}}^{(0)}$. However, this relaxed Sn-Sn bond length is significantly lower than the equilibrium α -Sn bond length $r_{\text{Sn}}^{(0)} = 2.813 \text{ \AA}$. We attribute this compression of the Sn-Sn bond to the lower bulk modulus of α -Sn compared to that of either Ge or zb-GeSn – i.e. the relatively soft Sn-Sn bond is compressed by the comparatively harder surrounding Ge-Ge and Ge-Sn bonds.

Figure 4.2(d) shows the corresponding HSEsol-calculated distribution of relaxed bond angles in the $\text{Ge}_{60}\text{Sn}_4$ supercell. Since the equilibrium tetrahedral bond angle $\theta^{(0)} = 109.5^\circ$ is equal for all tetrahedrally-bonded constituent materials – and hence the constituent materials Ge, α -Sn and zb-GeSn – the bond angle distribution provides, in general, less insight into the details of the lattice relaxation. We find that the relaxed bond angle distribution to be centred at $\theta^{(0)}$, with the lattice relaxation tending to produce a normal-like distribution of bond angles about this value. We note however the presence of a single outlying bond angle on the low side of the peak. This smallest angle describes a single Sn-Ge-Sn nearest-neighbour configuration, which has been highly distorted by the asymmetric relaxation of its local atomic environment.

Considering the corresponding LDA-calculated bond length distribution of Fig. 4.2(b), we note excellent qualitative and quantitative agreement with the corresponding HSEsol distribution. Relative to the HSEsol-relaxed supercell we calculate a maximum difference of 0.14% in the LDA-relaxed length of an individual nearest-neighbour bond, and an average error of only 0.04% across all nearest-neighbour bonds in the supercell. However, evident in Fig. 4.2(b) is a slight decrease in the width of the peak in the distribution of relaxed Ge-Sn bond lengths. We interpret this result as further confirmation that the LDA disproportionately overbinds Ge-Sn bonds compared to Ge-Ge or Sn-Sn bonds, as reflected in the differences between the HSEsol- and LDA-calculated lattice constants. Qualitatively, the VFF-calculated bond length distribution of Fig. 4.2(c) is in excellent agreement with the HSEsol distribution of Fig. 4.2(a): the VFF relaxation reproduces faithfully the width and relative number of relaxed Ge-Sn bonds having slightly different bond lengths. The maximum individual and overall average differences in relaxed bond length between the HSEsol and VFF relaxations are, respectively, 0.9 and 0.7%. Finally, we note that the LDA- and VFF-calculated bond angle distributions of Figs. 4.2(e)

and (f) display no significant qualitative or quantitative deviations from the corresponding HSEsol-calculated distribution of Fig. 4.2(d).

On the basis of these detailed comparisons, we conclude overall that both the LDA and VFF relaxations of a given $\text{Ge}_{1-x}\text{Sn}_x$ alloy supercell are in excellent quantitative agreement with the results of the significantly more computationally expensive HSEsol relaxation. This indicates that either LDA-DFT or the semi-empirical VFF potential of Eq. (4.1) can be used to reliably perform structural relaxations, offering high accuracy in conjunction with significantly reduced computational cost compared to HSEsol-DFT.

4.4 Supercell band structure

4.4.1 Band gap and spin-orbit splitting energy

Turning our attention to the electronic structure, we begin by considering the band structures calculated for the ordered $\text{Ge}_{63}\text{Sn}_1$ ($x = 1.56\%$) and $\text{Ge}_{15}\text{Sn}_1$ ($x = 6.25\%$) alloy supercells. The results of these calculations are shown in Fig. 4.3, where the top (bottom) row shows the band structure calculated for $\text{Ge}_{63}\text{Sn}_1$ ($\text{Ge}_{15}\text{Sn}_1$) using, from left to right, the HSEsol ((a) and (d)), LDA + mBJ ((b) and (e)), and VFF + TB ((c) and (f)) where the TB calculations were carried out by Dr Christopher Broderick. In each band structure plot the left- and right-hand panels respectively show the supercell band dispersion calculated along the (111) and (001) directions in the supercell Brillouin zone. The supercell wave vector \mathbf{K} is specified in units of $\frac{\pi}{A}$, where $A = 2a$ ($A = a$) is the lattice constant associated with the chosen $2 \times 2 \times 2$ SC (FCC) supercells. Recalling that the 64- and 16-atom supercells respectively possess SC and FCC lattice vectors, we note that the zone boundary along the (001) direction lies at $\frac{\pi}{A}$ in the 64-atom supercells. we recall that the supercells considered here have been chosen so that L-points from the Brillouin zone of the primitive unit cell are folded to the supercell zone centre at $\mathbf{K} = 0$. As such, the lowest energy CB states in Ge_{64} and Ge_{16} supercells are the degenerate L_{6c} CB minima, folded to $\mathbf{K} = 0$ from $\mathbf{k} = \frac{\pi}{a}(1, 1, 1)$ and equivalent points in the Brillouin zone of the primitive unit cell.

Examining the results of the HSEsol band structure calculations for $\text{Ge}_{63}\text{Sn}_1$ and $\text{Ge}_{15}\text{Sn}_1$ in Figs. 4.3(a) and 4.3(d), we note firstly that Sn incorporation gives rise to a strong reduction of the supercell band gap E_g with increasing x . For $\text{Ge}_{63}\text{Sn}_1$ and $\text{Ge}_{15}\text{Sn}_1$ we respectively calculate $E_g = 0.681$ and 0.388 eV, representing respective decreases of 85 and 378 meV compared to the indirect (fundamental) 0.766 eV Γ_{8v} - Γ_{7c} band gap of Ge. We note also a moderate increase of the VB spin-orbit splitting energy Δ_{SO} with increasing x . The respective values $\Delta_{\text{SO}} = 0.334$ and 0.379 eV calculated for the ordered 64- and 16-atom alloy supercells are 12 and 57 meV larger than that calculated for Ge.

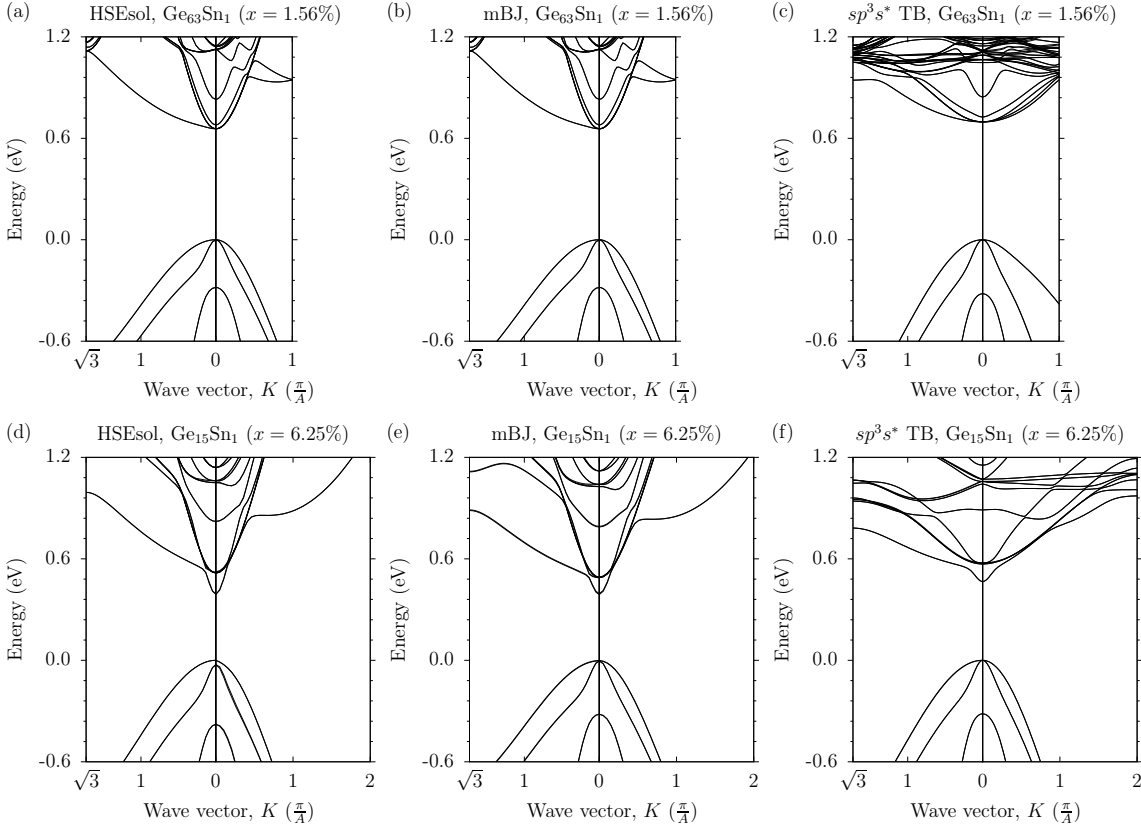


FIGURE 4.3: First principles and semi-empirical calculations of the band structure of two ordered $\text{Ge}_{1-x}\text{Sn}_x$ alloy supercells: a 64-atom $2 \times 2 \times 2$ SC $\text{Ge}_{63}\text{Sn}_1$ supercell (top row) and a 16-atom $2 \times 2 \times 2$ FCC $\text{Ge}_{15}\text{Sn}_1$ supercell (bottom row), having respective Sn compositions $x = 1.56$ and 6.25% . The left- and right-hand panel of each plot respectively shows the band structure calculated along the (111) and (001) directions in the supercell Brillouin zone. The band structures calculated via DFT, using HSEsol ((a) and (d)) and mBJ ((b) and (e)) XC functionals, and via a semi-empirical sp^3s^* TB Hamiltonian ((c) and (f)). The atomic positions used in the HSEsol, mBJ and sp^3s^* TB band structure calculations were respectively obtained from HSEsol, LDA and VFF supercell relaxations. For comparative purposes, the zero of energy has been chosen to lie at the VB edge in all cases.

The values of E_g and Δ_{SO} calculated using the HSEsol, LDA + mBJ and VFF + TB models are summarised in Table 4.4. Considering the mBJ-calculated values, we note slight underestimation of both the decrease in E_g and increase in Δ_{SO} compared to HSEsol calculations. The mBJ-calculated $\text{Ge}_{63}\text{Sn}_1$ and $\text{Ge}_{15}\text{Sn}_1$ band gaps of 0.660 and 0.356 meV represent respective decreases of 64 and 368 meV compared to the indirect (fundamental) Ge band gap of 0.724 eV. The corresponding VB spin-orbit splitting energies $\Delta_{\text{SO}} = 0.282$ and 0.316 eV represent respective increases of 8 and 42 meV compared to the Ge spin-orbit splitting energy $\Delta_{\text{SO}} = 0.274$ eV. For the $\text{Ge}_{63}\text{Sn}_1$ supercell the VFF + TB model predicts a 92 meV decrease in E_g , which is slightly larger than the HSEsol- and mBJ-calculated 85 and 64 meV decrease. For the $\text{Ge}_{15}\text{Sn}_1$ supercell the TB-calculated band gap $E_g = 0.392$ eV is in excellent agreement with the HSEsol-calculated value $E_g = 0.388$ eV.

Considering the values of E_g calculated using the three models for the disordered $\text{Ge}_{60}\text{Sn}_4$

TABLE 4.4: Band gap E_g and VB spin-orbit splitting energy Δ_{SO} for the $\text{Ge}_{1-x}\text{Sn}_x$ alloy supercells of Table 4.3, calculated via DFT, using the HSEsol and mBJ XC functionals, and via a semi-empirical sp^3s^* TB Hamiltonian. The corresponding calculated values of the direct $\Gamma_{8v}-\Gamma_{7c}$ and indirect (fundamental) $\Gamma_{8v}-L_{6c}$ band gaps of Ge are provided for reference, with the latter listed in parentheses.

Supercell	x (%)	Description	E_g (eV)			Δ_{SO} (eV)		
			HSEsol	mBJ	sp^3s^* TB	HSEsol	mBJ	sp^3s^* TB
Ge	—	Pure Ge	0.909 (0.766)	0.868 (0.724)	0.909 (0.766)	0.322	0.274	0.322
$\text{Ge}_{63}\text{Sn}_1$	1.56	Ordered SC	0.681	0.660	0.674	0.334	0.282	0.330
$\text{Ge}_{15}\text{Sn}_1$	6.25	Ordered FCC	0.388	0.356	0.392	0.379	0.316	0.353
$\text{Ge}_{60}\text{Sn}_4$	6.25	Disordered SC	0.429	0.425	0.442	0.372	0.322	0.365

supercell we note that, in all cases, E_g is significantly larger than in the ordered $\text{Ge}_{15}\text{Sn}_1$ supercell having the same Sn composition ($x = 6.25\%$). This strong dependence of the calculated band gap on the alloy microstructure provides initial evidence that alloy disorder and related band mixing effects play an important role in determining the details of the alloy electronic structure. The corresponding differences between the values of Δ_{SO} calculated for the disordered $\text{Ge}_{60}\text{Sn}_4$ and ordered $\text{Ge}_{15}\text{Sn}_1$ supercells are significantly smaller, and further suggest that alloy disorder effects can be expected to primarily impact the CB structure in $\text{Ge}_{1-x}\text{Sn}_x$ alloys. Overall, we note that the trends in E_g and Δ_{SO} vs. x calculated using all three models are in good quantitative agreement with previously published values. [124, 135]

4.4.2 Impact of Sn incorporation on conduction band structure

In addition to the respective strong decrease and moderate increase of E_g and Δ_{SO} with increasing x , we note key qualitative changes in the nature of the alloy CB edge states compared to those in pure Ge. The lowest energy supercell CB states at the zone centre in the equivalent SC Ge_{64} and FCC Ge_{16} supercells are the eightfold degenerate L_{6c} CB minima: the result of Kramers-degenerate bands folding back to $\mathbf{K} = \mathbf{0}$ from the four equivalent L points in the Brillouin zone of the primitive unit cell. The degeneracy of these folded L_{6c} states is lifted in the ordered alloy supercell calculations of Fig. 4.3. Examining the HSEsol-calculated CB eigenstates of the $\text{Ge}_{63}\text{Sn}_1$ supercell we find that the lowest energy CB eigenstates at $\mathbf{K} = \mathbf{0}$ are sixfold (threefold and Kramers) degenerate, and possess purely T_2 symmetry (p -like orbital character) at the Sn lattice site. The second lowest energy CB eigenstate lies 22 meV above the CB edge in energy, is twofold (Kramers) degenerate, and possesses A_1 symmetry (s -like orbital character) at the Sn lattice site. The next highest energy CB state in the HSEsol calculation is again twofold degenerate, lies 178 meV above the CB edge, and possesses A_1 symmetry (s -like orbital character) at the Sn lattice site. The corresponding energy differences in the mBJ and TB calculations – between the CB edge and the second- and third-lowest energy sets of $\mathbf{K} = \mathbf{0}$ alloy CB states – are, respectively, 23 and 174 meV, and 54 and 120 meV. The discrepancies in the TB-calculated energies of the higher lying CB states is a consequence of the chosen TB fit

to the HSEsol-calculated zb-GeSn band structure (cf. Sec. 4.2.3), during which the primary aim was to describe the alloy band gap and hybridised character of the alloy CB edge eigenstates.

This splitting of the folded L_{6c} states of Ge into distinct sets of states which are T_2 - and A_1 -symmetric (p - and s -like) at the Sn lattice site indicates Sn-induced mixing of the supercell zone-centre eigenstates of the Ge_{64} host matrix semiconductor, driven by (i) A_1 symmetric lattice relaxation about the Sn lattice site, and (ii) interactions between the $(4s)^2$ valence orbitals of Ge and the $(5s)^2$ valence orbitals of α -Sn. We note similar features in the HSEsol-calculated band structure of the $\text{Ge}_{15}\text{Sn}_1$ supercell (cf. Fig. 4.3). In this case the CB edge eigenstate is twofold (Kramers) degenerate and possesses purely A_1 symmetry (s -like orbital character) at the Sn lattice site, while the second lowest energy CB eigenstates lie 127 meV above the CB edge, are sixfold (threefold and Kramers) degenerate and possess purely T_2 symmetry (p -like orbital character) at the Sn lattice site. The corresponding energy differences in the mBJ and TB calculations are, respectively, 100 and 104 meV. We note that the T_2 -symmetric (p -like) triplet in the HSEsol and mBJ calculations splits into a singlet and higher lying doublet – separated by 21 meV – in the TB calculation. This is a result of the large spin-orbit coupling associated with the substitutional Sn atom, combined with the manner in which the atomic spin-orbit coupling is parametrised in the TB method. [165] This ordering of the lowest and second-lowest energy CB states is reversed compared to that in the $\text{Ge}_{63}\text{Sn}_1$ supercell. Further analysis of the CB edge eigenstates, presented below, shows that the direct nature of the $\text{Ge}_{1-x}\text{Sn}_x$ alloy CB edge states evolves continuously with increasing x , and that this evolution is driven by the aforementioned Sn-induced mixing. This band mixing, which acts to hybridise the L_{6c} and Γ_{7c} CB edge states of Ge, leads to the emergence of a strongly hybridised alloy CB edge in $\text{Ge}_{1-x}\text{Sn}_x$ alloys. [124] By comparison, the impact of Sn incorporation on the VB is minimal: the alloy VB edge states in all supercells retain primarily Ge Γ_{8v} character.

While the TB model describes well the impact of Sn incorporation on the CB and VB edge states at $\mathbf{K} = \mathbf{0}$ compared to the DFT calculations we note, in both the 64- and 16-atom calculations of Figs. 4.3(c) and 4.3(f), (i) overestimation of electron effective masses, and (ii) the presence in the CB dispersion of additional folded bands within the range of energies displayed in Fig. 4.3. These features represent a typical TB fit to the band structure. Firstly, fitting the TB parameters to the energies of the lowest CB at the L, Γ and X points is known to lead to overestimation of CB edge effective masses in a nearest-neighbour sp^3s^* model. [166] Secondly, the TB structure described by the sp^3s^* model is dispersionless between the X and W points in the Brillouin zone: [153, 167] energies of W-point CB states generally lie at higher energies than those at X in first principles calculations, leading to more bands folding back to the supercell zone centre at lower energies in the TB calculations. We emphasise however that these well-known features of the sp^3s^* TB model do not impede the description of the character, hybridisation and localisation of zone-centre alloy band edge states. The TB method allows for accurate descriptions of the impact of localised impurities, as has been demonstrated

previously for highly-mismatched III-V-N [122, 168] and III-V-Bi [169, 170] alloys, as well as III-N semiconductor alloys. [171, 172] We emphasise that both the mBJ and TB calculations qualitatively and quantitatively describe the behaviour revealed by the HSEsol calculations, providing a key confirmation of their suitability to perform accurate analysis of the $\text{Ge}_{1-x}\text{Sn}_x$ electronic structure.

4.4.3 Sn-induced band mixing: band gap pressure coefficient

To quantify the Sn-induced band mixing and its impact on the nature of the alloy CB edge states, we have used all three models to calculate the pressure coefficient $\frac{dE_g}{dP}$ of the fundamental band gap. To do so we proceed by applying hydrostatic pressure to the supercell and relaxing the internal degrees of freedom before computing the electronic structure. The results of these calculations are summarised in Table 4.5. HSEsol calculations predict $\frac{dE_g}{dP} = 4.66$ and 13.33 meV kbar⁻¹ for the indirect Γ_{8v} - L_{6c} and direct Γ_{8v} - Γ_{7c} band gaps of Ge. These calculated values are in good quantitative agreement with the respective measured values of 4.3 and 12.9 meV kbar⁻¹. [131, 159] The corresponding LDA + mBJ-calculated values 4.07 and 13.23 meV kbar⁻¹ are in good quantitative agreement with both the HSEsol calculations and experiment. Using the VFF + TB model we calculate indirect- and direct-gap pressure coefficients of 4.69 and 13.52 meV kbar⁻¹ for Ge. The TB parameters are fitted exactly to the HSEsol band edge hydrostatic deformation potentials. We note the small (< 1.5%) errors in the TB-calculated pressure coefficients reflects the use of a harmonic VFF potential to relax the internal degrees of freedom under applied pressure. While the VFF potential of Eq. (4.1) describes exactly the bulk moduli B of Ge, α -Sn and zb-GeSn, it does not describe the pressure dependence of B – which are captured implicitly in the DFT calculations – leading to minor errors at experimentally relevant pressures.

Given the large differences in the pressure coefficients associated with the direct and indirect (Γ_{8v} - L_{6c} and Γ_{8v} - X_{5c}) band gaps of Ge, calculations and experimental measurements of $\frac{dE_g}{dP}$ constitute a key experimental signature of band mixing effects: hybridised CB edge states possess a pressure coefficient intermediate between those of the band gaps associated with the

TABLE 4.5: Band gap pressure coefficients for the $\text{Ge}_{1-x}\text{Sn}_x$ alloy supercells of Tables 4.3 and 4.4, calculated using the HSEsol, LDA + mBJ and VFF + TB models described in Sec. 4.2. The calculated pressure coefficients of the direct Γ_{8v} - Γ_{7c} and indirect (fundamental) Γ_{8v} - L_{6c} band gaps of Ge are provided for reference, with the latter listed in parentheses.

Supercell	x (%)	$\frac{dE_g}{dP}$ (meV kbar ⁻¹)		
		HSEsol	mBJ	sp^3s^* TB
Ge	—	13.33 (4.66)	13.23 (4.07)	13.52 (4.69)
Ge ₆₃ Sn ₁	1.56	4.75	4.19	4.73
Ge ₁₅ Sn ₁	6.25	10.00	9.50	10.00
Ge ₆₀ Sn ₄	6.25	8.32	7.57	9.39

constituent (hybridising) states. HSEsol calculations predict respective pressure coefficients $\frac{dE_g}{dP} = 4.75$ and 10.00 meV kbar⁻¹ for the ordered Ge₆₃Sn₁ and Ge₁₅Sn₁ supercells. The first of these values is very close to the indirect-gap pressure coefficient of Ge, reflecting that the CB edge states in Ge₆₃Sn₁ are largely derived from the L_{6c} CB edge states of the corresponding Ge₆₄ host matrix semiconductor. The second of these values is intermediate between those calculated for the indirect (fundamental) Γ_{8v} -L_{6c} and direct band gaps of Ge, confirming the presence of Sn-induced Γ_{7c} -L_{6c} mixing. That is, as x increases to 6.25% the calculated pressure coefficient increases significantly, towards that of the Ge direct band gap. We note that the calculated values of $\frac{dE_g}{dP}$ for the Ge₁₅Sn₁ supercell are in good agreement with the measured value of 9.2 meV kbar⁻¹ for a Ge_{0.94}Sn_{0.06} ($x = 6\%$) photodiode. [131, 159] These calculated and measured values of $\frac{dE_g}{dP}$ suggest that the hybridised nature of the alloy CB edge states in Ge_{1-x}Sn_x depends strongly on Sn composition x , and suggests that the CB edge states in the ordered Ge₁₅Sn₁ supercell are primarily Ge Γ_{7c} -derived, with the alloy having primarily (but not purely) direct-gap character.

For the disordered Ge₆₀Sn₄ supercell we calculate $\frac{dE_g}{dP} = 8.32$ meV kbar⁻¹. This value is reduced compared to that calculated for the ordered Ge₁₅Sn₁ supercell having the same Sn composition, further emphasising that alloy disorder has a strong impact on the nature of the hybridised Ge_{1-x}Sn_x CB edge states. This calculated variation of $\frac{dE_g}{dP}$ at fixed x highlights that important quantitative differences can result in the character of the Ge_{1-x}Sn_x CB edge states, resulting from an interplay of band mixing and alloy disorder effects. Examining the data of Table 4.5 we note that the LDA + mBJ and VFF + TB models correctly capture the increase in $\frac{dE_g}{dP}$ vs. x obtained from HSEsol calculations, suggesting that both models accurately capture the nature of the hybridised CB edge states and their evolution with increasing x .

Based on this analysis we reach three conclusions. Firstly, the calculated (and measured) values of $\frac{dE_g}{dP}$ being intermediate between those of the direct and Γ_{8v} -L_{6c} band gaps of Ge indicates that the Ge_{1-x}Sn_x alloy CB edge states consist of a strong admixture of Ge Γ_{7c} and L_{6c} states in the supercell calculations. Secondly, this band mixing is driven by the differences in covalent radius and chemical properties between Ge and Sn. Thirdly, this band mixing evolves continuously with increasing x , transferring Ge Γ_{7c} character to the alloy band edge. This final conclusion is in accordance with the measurements of [131] and [159] described in Chapter 3, which found $\frac{dE_g}{dP} = 4.33, 9.2, 10.4$ and 12.9 meV kbar⁻¹ for the fundamental band gap in Ge_{1-x}Sn_x photodiodes having $x = 0, 6, 8$ and 10% .

This suggests that the indirect- to direct-gap transition in Ge_{1-x}Sn_x proceeds continuously rather than occurring abruptly at some critical Sn composition. Combined, these results would suggest significant implications for the interpretation of the Ge_{1-x}Sn_x band structure. The strongly hybridised nature of the Ge_{1-x}Sn_x CB edge states could have significant consequences for technologically relevant material properties. The LDA + mBJ and VFF + TB models

established and benchmarked here provide quantitatively accurate descriptions of band mixing effects in alloy supercell calculations. It should be noted however that the supercells used here have strong medium range order due to their small size. Larger supercells are therefore required to investigate the evolution of the band structure as the medium range order is reduced. Such calculations are not feasible using DFT approaches, but are currently underway by colleagues using the tight-binding method.

4.5 Impact of Sn local environment on germanium-tin alloy electronic structure

Having quantified the impact of Sn incorporation on the band structure of ordered $\text{Ge}_{1-x}\text{Sn}_x$ alloy supercells, we now turn our attention to the investigation of how the separation of Sn atoms in disordered alloy supercells impacts the alloy electronic band structure. We begin by taking a $\text{Ge}_{15}\text{Sn}_1$ supercell and substituting a second Sn atom in to the supercell in place of a Ge atom to form four distinct $\text{Ge}_{14}\text{Sn}_2$ ($x = 12.5\%$) supercells in which the two Sn atoms are located at fourth-, third-, second- and first-nearest lattice sites respectively. We then repeat this same substitution with the $\text{Ge}_{63}\text{Sn}_1$ supercell to form four distinct $\text{Ge}_{62}\text{Sn}_2$ ($x = 3.13\%$) supercells in which the two Sn atoms are located at fourth-, third-, second- and first-nearest lattice sites respectively. In this manner, we can investigate how the electronic properties of $\text{Ge}_{14}\text{Sn}_2$ and $\text{Ge}_{62}\text{Sn}_2$ supercells vary as the separation between two Sn atoms decreases until they form a nearest-neighbour Sn-Sn pair. For each case we calculate the electronic structure and quantify the dependence of the fundamental band gap E_g , and its pressure coefficient $\frac{dE_g}{dP}$, on the relative position of the two Sn atoms in the supercell.

We note that incorporation of > 1 substitutional Sn atoms breaks the cubic symmetry of the underlying diamond lattice, which was preserved in the ordered supercell calculations of Sec. 4.6. As a result of this reduction in symmetry the fourfold (twofold and Kramers) degeneracy of the zone-centre VB edge states is lifted, giving rise to two distinct sets of Kramers degenerate states. The precise value of the VB edge splitting in a disordered supercell is in general a non-monotonic function of Sn composition x , but instead depends on the precise short-range disorder present in a given alloy supercell. In this section, as well as in Sec. 4.6 below, we therefore calculate band gaps in disordered supercells with respect to the average energy of the split VB edge states.

Schematic illustrations of the different configurations of the 16 atoms supercell for the 4th – 1st nearest neighbour Sn pairs are shown in Fig. 4.4. In all cases one Sn atom is positioned on the corner of the cell at the (0,0,0) site while the position of the second Sn atom is varied for different nearest neighbour configurations. To achieve a 4th nearest neighbour configuration in the $\text{Ge}_{14}\text{Sn}_2$ supercell the second Sn atom is positioned on the (1,1,1) site. As a result of the

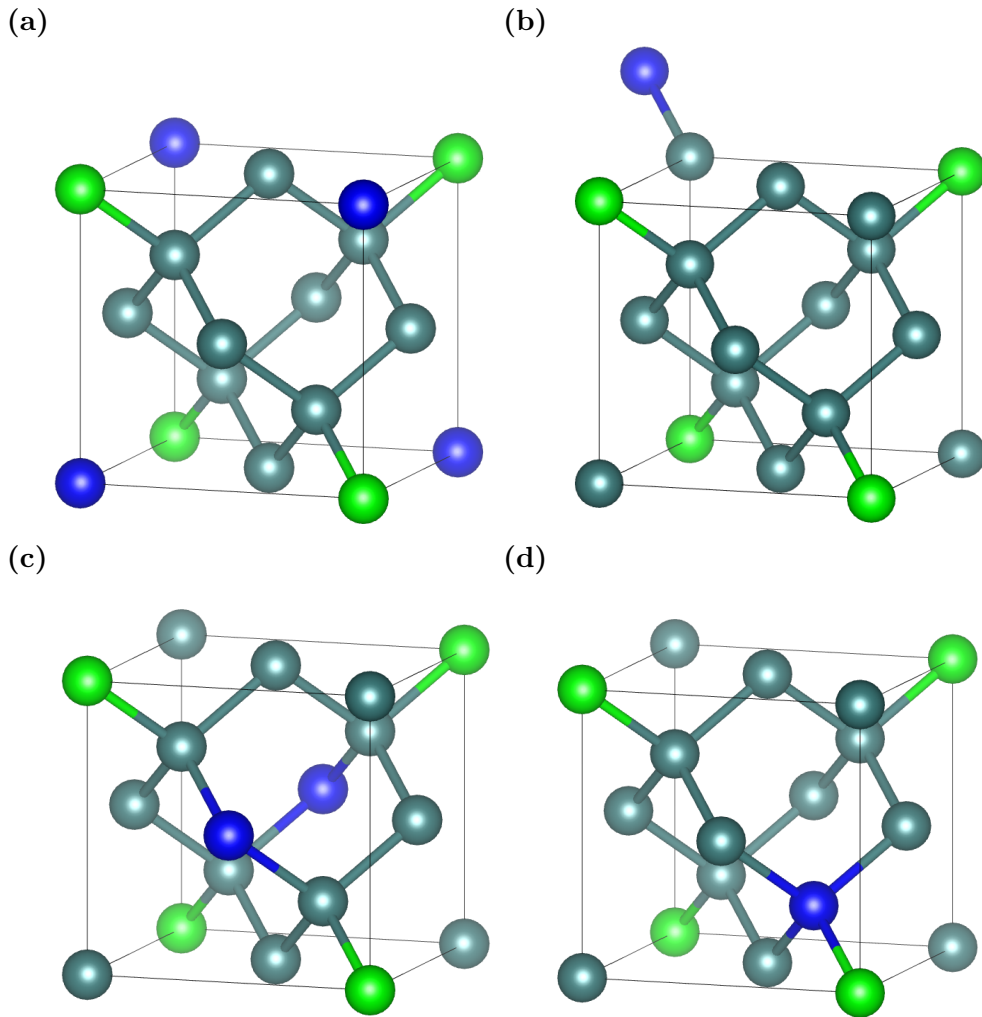


FIGURE 4.4: Schematic of the 16 atom Ge supercell structure with two Sn atoms (coloured in green and blue respectively) positioned at nearest neighbour distances varying from (a) fourth, (b) third, (c) second, and (d) first nearest neighbours (NNs) to one another.

periodic repetition of the supercell each Sn atom in this configuration will have 12 separate 4th nearest Sn neighbours. By then moving this Sn atom $(+\frac{1}{4}, +\frac{1}{4}, +\frac{1}{4})$ to the $(\frac{5}{4}, \frac{5}{4}, \frac{5}{4})$ site a 3rd nearest neighbour supercell is formed. We note that in moving to this third nearest neighbour configuration irrespective of which direction one moves from the (1,1,1) site the atom to which one moves will always lie outside of the cubic cell used in in Fig. 4.4. Each Sn atom in this configuration will have three 3rd nearest neighbour Sn atoms. For the 2nd nearest neighbour case the second Sn atom is positioned on the $(0, \frac{1}{2}, \frac{1}{2})$ lattice sites. Periodic repetition of the supercell means that the Sn atom will have two 2nd nearest neighbouring Sn atoms in this configuration. Finally for the 1st nearest neighbour $\text{Ge}_{14}\text{Sn}_2$ cell the second Sn atom is set up on the $(\frac{1}{4}, \frac{1}{4}, \frac{1}{4})$ lattice site. Each Sn atoms in the cell will have a single nearest neighbouring Sn atom as well and three 3rd nearest neighbouring Sn atoms arising from the periodic repetition of the supercell.

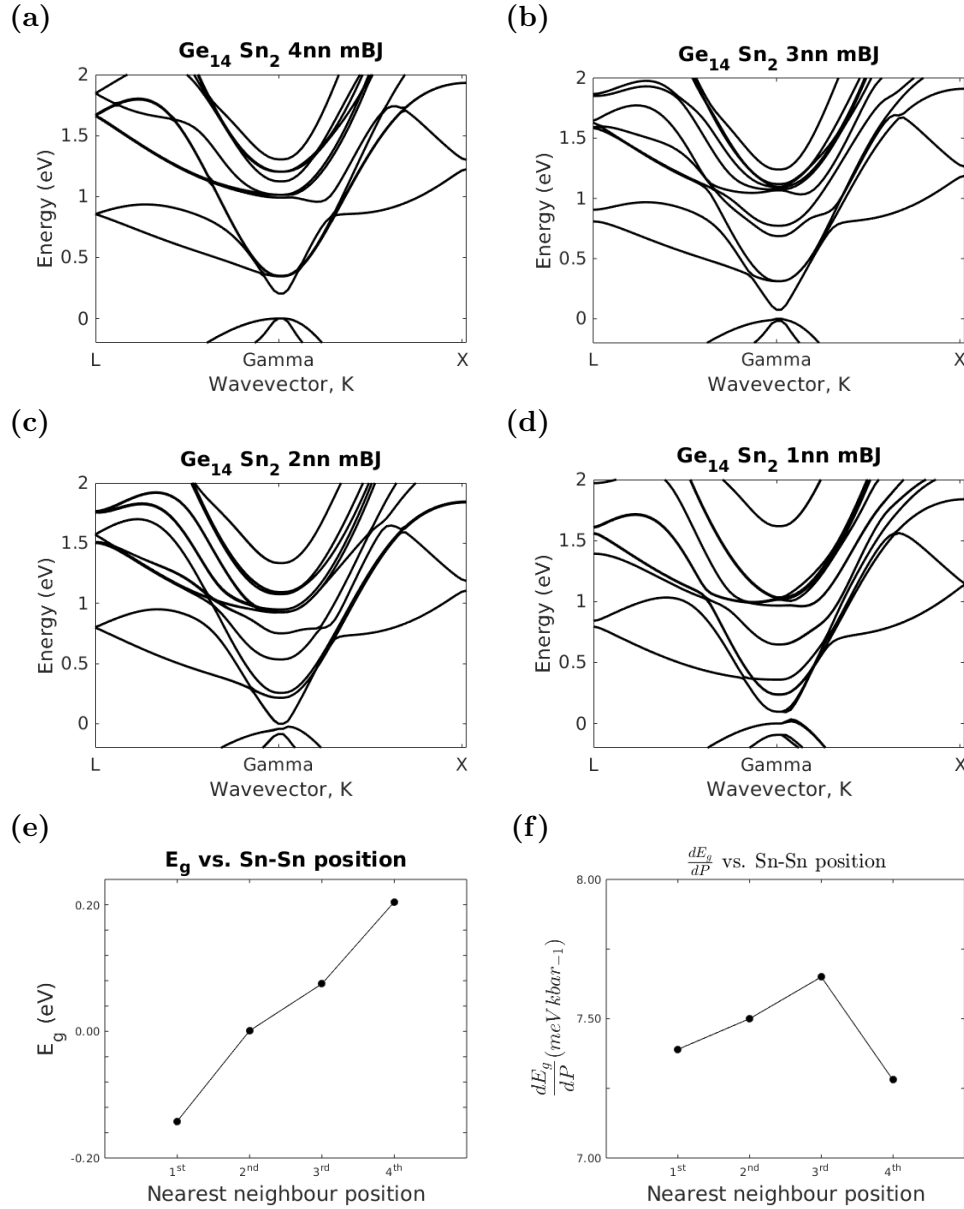


FIGURE 4.5: Calculated CB structure of disordered, 16-atom ($2 \times 2 \times 2$ SC) $\text{Ge}_{14}\text{Sn}_2$ ($x = 3.125\%$) supercells in which the two Sn atoms are (a) fourth, (b) third, (c) second, and (d) first nearest neighbours (NNs). (e) Calculated variation of the fundamental band gap E_g of the $\text{Ge}_{14}\text{Sn}_2$ supercells of (a) – (d) with respect to the relative position of the two Sn atoms. (f) same as (e), but for the pressure coefficient $\frac{dE_g}{dP}$ of the fundamental band gap E_g .

The results of the calculations – utilizing the mBJ XC functional – for disordered $\text{Ge}_{14}\text{Sn}_2$ supercells are summarised in Figure 4.5, where Figures 4.5(a), 4.5(b), 4.5(c) and 4.5(d) respectively show the calculated conduction band structure for the fourth-, third-, second- and first-nearest neighbour Sn-Sn atom pair respectively. Figures 4.5(e) and 4.5(f) show the dependence of the calculated values of E_g and $\frac{dE_g}{dP}$ on the relative position of the two Sn atoms respectively.

In an overall sense the band structures shown in Figures 4.5(a)–(d), are in good qualitative agreement with each other. In each of the four supercells Γ_{7c} from pure Ge has reduced in

energy sufficiently to come below the (Kramers degenerate) triplet state which arises from L_{6c} of pure Ge to form a direct band gap. This feature is perhaps unsurprising given the high 12.5% Sn content present in these supercells and the transition to a direct gap by 12.5% Sn content is in agreement with existing literature predictions. However despite qualitative similarities in the calculated band structures, Sn clustering produces significant quantitative differences in the calculated electronic properties of supercells with fixed Sn composition x .

Starting with the $\text{Ge}_{14}\text{Sn}_2$ supercell in which the two Sn atoms are fourth-nearest neighbours we calculate a fundamental band gap $E_g = 0.205$ eV, which is reduced by 519 meV compared to the fundamental band gap of Ge, by 455 meV compared that of the ordered $\text{Ge}_{63}\text{Sn}_1$ (1.56%) supercell and by 0.151 meV compared that of the ordered $\text{Ge}_{15}\text{Sn}_1$ (6.25%) supercell. Correspondingly, spin orbit splitting of this supercell has a value of $\Delta_{\text{SO}} = 0.335$ eV, which is increased by 61 meV compared to that in Ge, and by 53 meV and 19 meV compared to $\text{Ge}_{63}\text{Sn}_1$ and $\text{Ge}_{15}\text{Sn}_1$ supercells respectively. For the case of third-nearest neighbour Sn atoms we calculate a band gap of $E_g = 0.0751$ eV, a reduction of 130 meV compared to the fourth-nearest neighbour Sn atoms, and $\Delta_{\text{SO}} = 0.342$ eV, 7 meV higher than that calculated for fourth-nearest neighbour Sn atoms. For the case of second-nearest neighbour Sn atoms we calculate a negative band gap of $E_g = -0.001$ eV, 204 meV lower than that of the fourth-nearest neighbour Sn atoms, and $\Delta_{\text{SO}} = 0.3552$ eV, 20 meV higher than that calculated for fourth-nearest neighbour Sn atoms. Finally for the ultimate case, where the two Sn atoms are positioned as a Sn-Sn nearest neighbour pair we again calculate a negative band gap, this time with a value of $E_g = -0.142$ eV, 866 meV lower than that of the fundamental band gap of Ge, and 347 meV lower than the fundamental band gap in the case of fourth-nearest neighbour Sn atoms. Similarly, we calculate $\Delta_{\text{SO}} = 0.387$ eV for the supercell containing a Sn-Sn nearest-neighbour pair, an increase of 113 meV compared to that in bulk Ge, and an increase of 52 meV compared to the case of fourth-nearest neighbour Sn atoms. Since these four disordered supercells have equal Sn composition $x = 12.5\%$, this calculated ≈ 347 meV variation in E_g is strongly indicative of the impact that Sn-Sn clustering may have on the electronic properties of $\text{Ge}_{1-x}\text{Sn}_x$ alloys.

Figure 4.5(f) shows the calculated pressure coefficients $\frac{dE_g}{dP}$, associated with the fundamental supercell band gap E_g , as a function of Sn-Sn separation for the same series of $\text{Ge}_{14}\text{Sn}_2$ supercells. In line with the ordered supercell calculations of Sec. 4.3.2, the calculated values of $\frac{dE_g}{dP}$ are intermediate between the values 4.07 and 13.23 meV kbar⁻¹ associated with the L_{6c} - Γ_{8v} and Γ_{7c} - Γ_{8v} band gaps of Ge (cf. Table 4.5). Again, this reveals the hybridised nature of the alloy CB edge states in these supercells, which are primarily derived from a linear combination of Ge L_{6c} states having strong s -like orbital character at the Sn lattice sites, but which contain an admixture of Ge Γ_{7c} character. In all four cases – having fourth-, third-, second- and first-nearest neighbour Sn atoms – the calculated value of $\frac{dE_g}{dP}$ remains closest to that associated with the state arising from the Γ_{7c} state of pure Ge band, suggesting that the supercell band gap is primarily direct in nature for compositions of $x = 12.5\%$ Sn. We note that the precise

value of $\frac{dE_g}{dP}$ varies non-monotonically with Sn-Sn separation. This non-monotonic change in hydrostatic pressure with varying neighbour distance is however noted to be rather small, with the difference of 0.4meV/kbar between the largest and smallest values representing only a 5% change in mixing. We cannot identify why the pressure coefficient should decrease slightly in the fourth neighbour case. It can be seen from Fig. 4.4(a) that this Ge₁₄Sn₂ supercell is equivalent to a Ge₇Sn₁ cubic supercell, for which there will be no Γ -X mixing. It is not clear however why the elimination of Γ -X mixing should lead to a reduction in the pressure coefficient. Nevertheless, these results reveal that the details of the Sn-induced band mixing are impacted by the specific short-range disorder present in a given alloy supercell.

This demonstrates more generally that the character of the CB edge states, and hence the nature of the band gap, in real (disordered) Ge_{1-x}Sn_x alloys, is sensitive to the presence of short-range alloy disorder and Sn clustering. We note also that long range periodic ordering effects arising from the small size of the supercell studied may impact here on the level of mixing seen as the two Sn atoms in the supercell are moved closer together from fourth nearest neighbours initially to eventually forming a Sn-Sn nearest neighbour pair. We expect that in larger supercells the impact of long range periodic ordering should be lessened and the mixing closer to that which might be seen in a real disordered alloy.

The unfolded band structures of the disordered, 16-atom ($2 \times 2 \times 2$ SC) Ge₁₄Sn₂ ($x = 12.5\%$) supercells in which the two Sn atoms are positioned as (a) fourth, (b) third, (c) second, and (d) first nearest neighbours are shown in Fig 4.6 (a)–(d). These band structures, which were unfolded using the BandUP software package [97] are all in generally good qualitative agreement and agree well in terms of conduction and valence band energies with the folded band structures shown in Fig. 4.5 (a) – (d). In each of unfolded bandstructures from fourth to first nearest neighbour Sn pairs the lowest conduction band state lies at the Γ CBE critical point, which again is in good agreement with hydrostatic pressure calculations, which indicated the presence of strong Γ character in the lowest energy conduction band state. We note that because there are 4 L states in the unfolded band structure, and the lowest state at Γ can mix with all 4 of them, only a fraction (25%) of this L character is associated with the one L point shown in the unfolded band structure. The L character of the lowest conduction state deduced from the pressure calculations is then very difficult to observe in Fig. 4.5.

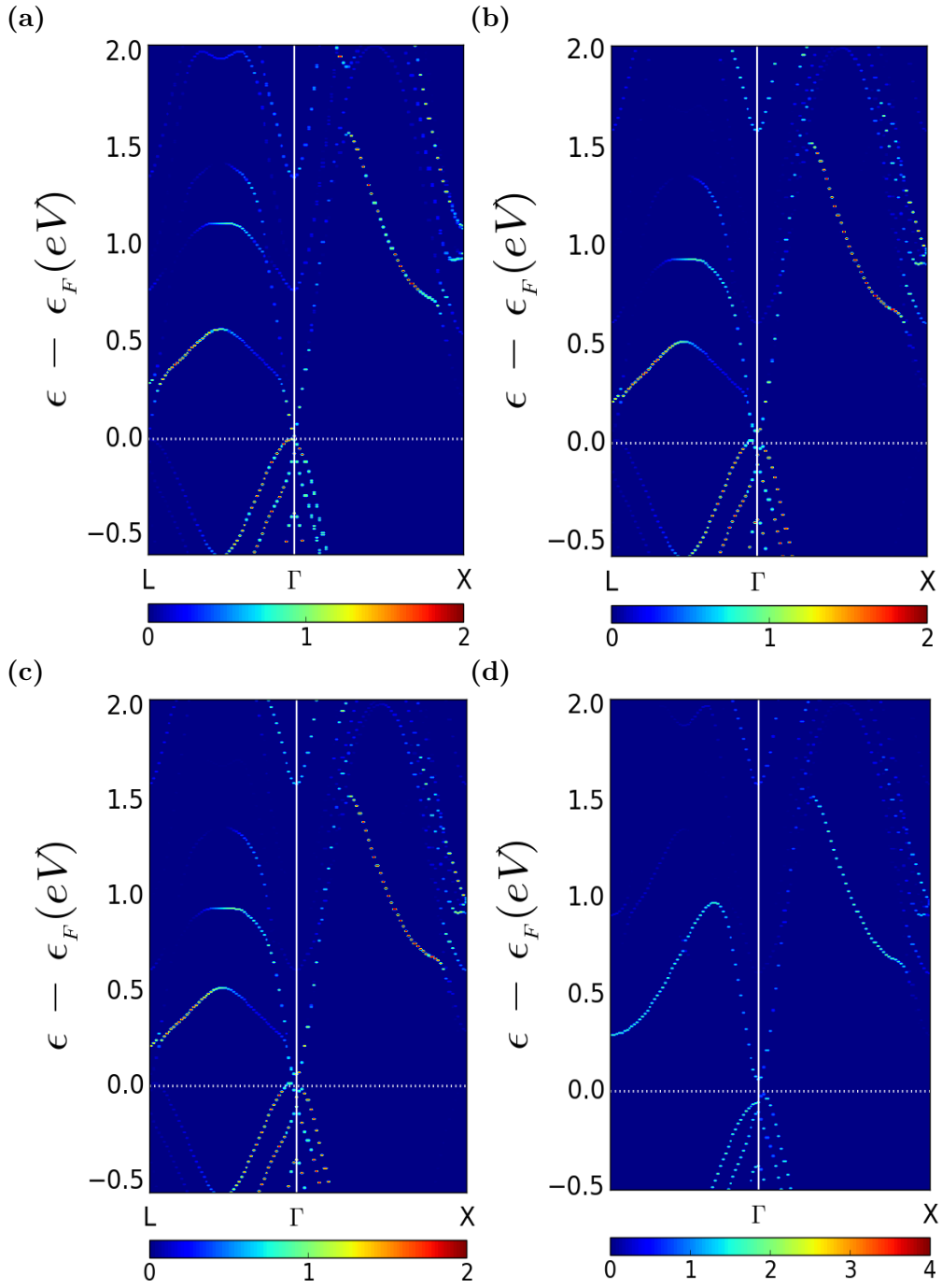


FIGURE 4.6: Calculated unfolded band structure of disordered, 16-atom ($2 \times 2 \times 2$ SC) $\text{Ge}_{14}\text{Sn}_2$ ($x = 12.5\%$) supercells in which the two Sn atoms are (a) fourth, (b) third, (c) second, and (d) first nearest neighbours (NNs).

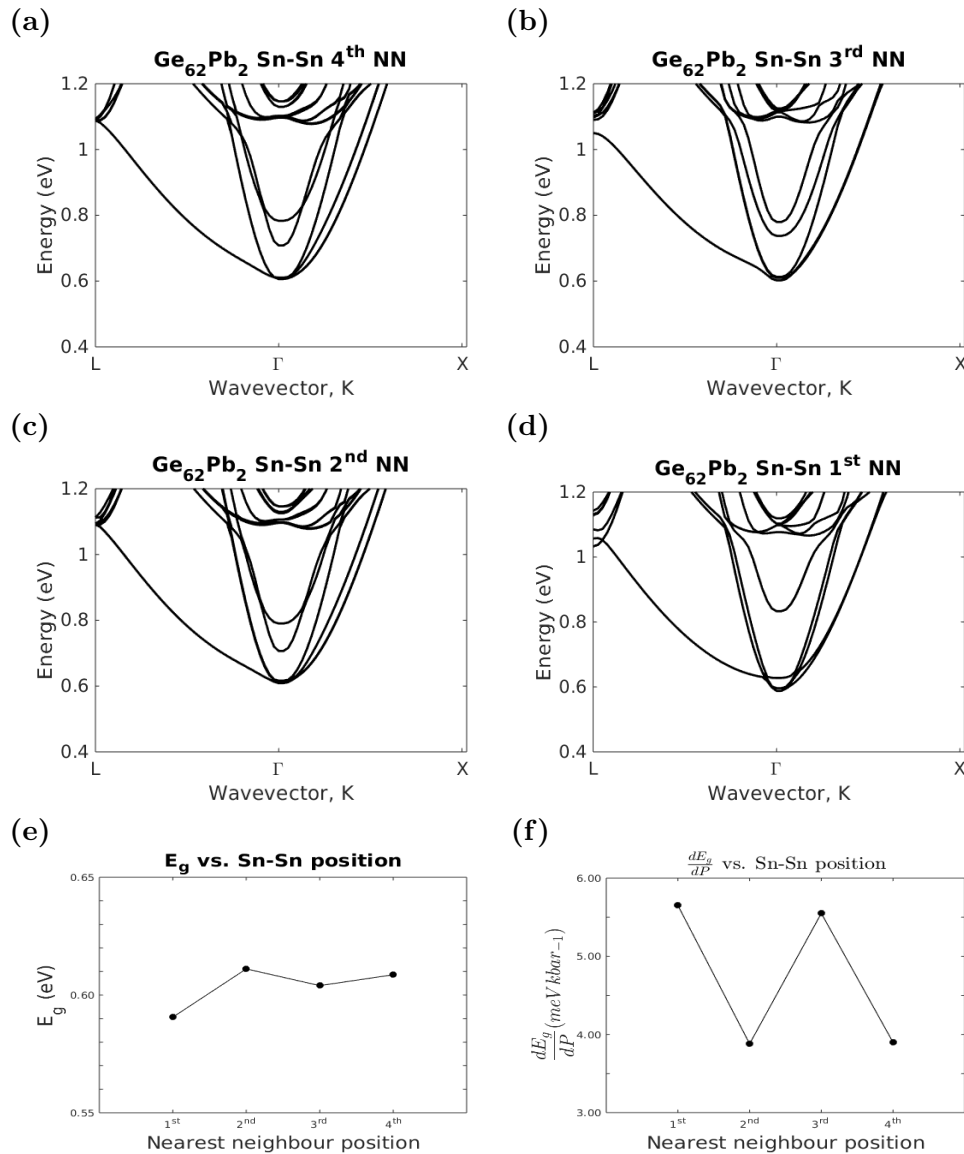


FIGURE 4.7: Calculated CB structure of disordered, 64-atom $(2 \times 2 \times 2)$ SC $\text{Ge}_{62}\text{Sn}_2$ ($x = 3.125\%$) supercells in which the two Sn atoms are (a) fourth, (b) third, (c) second, and (d) first nearest neighbours (NNs). (e) Calculated variation of the fundamental band gap E_g of the $\text{Ge}_{62}\text{Sn}_2$ supercells of (a) – (d) with respect to the relative position of the two Sn atoms. (f) same as (e), but for the pressure coefficient $\frac{dE_g}{dP}$ of the fundamental band gap E_g .

Moving on from the $\text{Ge}_{14}\text{Sn}_2$ disordered alloy supercells, Figure 4.7 summarises the results of the calculations examining the band structure of the larger $\text{Ge}_{62}\text{Sn}_2$ disordered alloy supercells of 3.125 % Sn content with Figures 4.7(a) – 4.7(d) showing the calculated conduction band structure for the fourth-, third-, second- and first-nearest neighbour Sn-Sn atom pair respectively. Figures 4.7(e) and 4.7(f) show the dependence of the calculated values of E_g and $\frac{dE_g}{dP}$ respectively on the relative position of the two Sn atoms in the supercell. The band structures shown in Figures 4.7(a), 4.7(b), 4.7(c) and 4.7(d) display, overall, high qualitative similarity. Similarly to the ordered supercells described earlier in the chapter, the three (Kramers degenerate) lowest energy CB states in each of these supercells possess primarily p -like orbital

character at Sn lattice sites, with the next two (Kramers degenerate) CB states up in energy possessing primarily *s*-like orbital character at Sn lattice sites. However while in the ordered alloy supercells the three *p*-like Ge L_{6c} -derived states form degenerate triplet states, here their degeneracy is lifted in the disordered supercells due to the loss of the underlying cubic symmetry of the lattice. However, as we describe below, despite qualitative similarities in the calculated band structures, Sn clustering produces significant quantitative differences in the calculated electronic properties in supercells having fixed Sn composition x .

Beginning with the $\text{Ge}_{62}\text{Sn}_2$ supercell in which the two Sn atoms are positioned as fourth-nearest neighbours we calculate a fundamental band gap $E_g = 0.609$ eV, which is reduced by 115 meV compared to the fundamental band gap of Ge, in line with earlier predictions of a 34meV decrease per % Sn incorporated, and by 72 meV compared to that of the ordered $\text{Ge}_{63}\text{Sn}_1$ supercell considered above. Correspondingly, we calculate $\Delta_{\text{SO}} = 0.289$ eV for this $\text{Ge}_{62}\text{Sn}_2$ supercell, which is increased by 15 meV compared to that in Ge, and by 7 meV compared to that in $\text{Ge}_{63}\text{Sn}_1$. In line with the ordered supercell calculations of Sec. 4.4, these results confirm that Sn incorporation in Ge leads to a strong decrease in E_g and increase in Δ_{SO} with increasing x . For the case of third-nearest neighbour Sn atoms we calculate $E_g = 0.604$ eV ($\Delta_{\text{SO}} = 0.289$ eV), 5 meV lower than (equal to) that calculated in the case of fourth-nearest neighbour Sn atoms. Ultimately, in the presence of a nearest-neighbour Sn-Sn pair we calculate $E_g = 0.591$ eV, which is reduced by 133 meV compared to the fundamental band gap of Ge, and by 18 meV compared to the case of fourth-nearest neighbour Sn atoms. Similarly, we calculate $\Delta_{\text{SO}} = 0.293$ eV for the supercell containing a Sn-Sn nearest-neighbour pair, which is increased by 19 meV compared to that in Ge, and by 4 meV compared to the case of fourth-nearest neighbour Sn atoms. We emphasise again that the calculated decrease of E_g – shown in Fig. 4.7(e) – and increase of Δ_{SO} (not shown) as the two Sn atoms are brought closer together is not a monotonic function of the Sn-Sn inter atomic distance, but depends on the specific relative position of the two Sn atoms. Since these four disordered supercells have equal Sn composition $x = 3.125\%$, this calculated ≈ 18 meV variation in E_g – representing $\approx 3\%$ of the total band gap – indicates the non negligible impact that Sn-Sn clustering may have on the electronic properties of $\text{Ge}_{1-x}\text{Sn}_x$ alloys.

Figure 4.7(f) shows the calculated pressure coefficients $\frac{dE_g}{dP}$, associated with the fundamental supercell band gap E_g , as a function of Sn-Sn separation for the same series of $\text{Ge}_{62}\text{Sn}_2$ supercells. Similarly to the ordered supercell calculations of Chapter. 3, the calculated values of $\frac{dE_g}{dP}$ in these four primarily indirect gap supercells are all close to the value of 4.07 meV kbar $^{-1}$ associated with the L_{6c} - Γ_{8v} band gap of Ge (cf. Table 4.5). This suggests that the supercell band gap remains primarily indirect in nature at $x = 3.125\%$. We also note that the precise value of $\frac{dE_g}{dP}$ varies non-monotonically with Sn-Sn separation, indicating again that the details of the Sn-induced band mixing are impacted by the specific short-range disorder present in a given alloy supercell. This demonstrates more generally that the character of the CB edge

states, and hence the nature of the band gap, in real (disordered) $\text{Ge}_{1-x}\text{Sn}_x$ alloys, is likely to be sensitive to the presence of short-range alloy disorder and Sn clustering.

Overall, these results demonstrate that the calculated values of E_g and $\frac{dE_g}{dx}$ – the latter reflecting the hybridised character of the alloy CB edge states – in $\text{Ge}_{1-x}\text{Sn}_x$ at fixed Sn composition x display significant dependence on the precise short-range alloy disorder present in a given alloy supercell. We note however that due to the small number of atoms in these supercells, the importance of such short-range disorder effects may be somewhat overstated here in comparison to the effects that would likely be noted in larger scale alloy supercell calculations. This issue is discussed in more detail in Sec. 4.6 below. While our analysis in Chapter. 3 identified the presence of Sn-induced band mixing in $\text{Ge}_{1-x}\text{Sn}_x$, our calculations here indicate the sensitivity of the $\text{Ge}_{1-x}\text{Sn}_x$ electronic structure to the presence of short-range alloy disorder (particularly in the form of clustering of substitutional Sn atoms). From a theoretical perspective, our results therefore suggest the breakdown of the virtual crystal approximation in $\text{Ge}_{1-x}\text{Sn}_x$ alloys, which neglects effects related to band mixing and alloy disorder. We therefore conclude that atomistic calculations which explicitly account for the differences in size and chemical properties between Ge and Sn are required to provide quantitative insight into the properties of real $\text{Ge}_{1-x}\text{Sn}_x$ alloys.

4.6 Disordered alloys: electronic structure evolution in germanium-tin special quasi-random structures

Having already investigated the important role short-range Sn-related structural disorder plays in influencing the details of the alloy electronic structure, we focus now on how the electronic structure evolves with x in more realistic, disordered $\text{Ge}_{1-x}\text{Sn}_x$ special quasi-random structures. To begin, the suitability of these special quasi-random structures for use in electronic structure calculations is assessed by comparing predicted and actual occurrences of clusters of first nearest-neighbouring Sn atoms in randomly disordered substitutional $\text{Ge}_{1-x}\text{Sn}_x$ alloys of increasing Sn composition x . The probability of occurrence of a Sn-Sn pair – i.e. the probability that two Sn atoms substituted at randomly chosen lattice sites occupy neighbouring sites – varies for small x as $2x^2$. As such, we would expect that a randomly disordered N -atom supercell contains, on average, a total of $\sim N \times 2x^2$ Sn pairs. Figure 4.8(a) shows the expected (solid red line) and actual (solid green bars) number of Sn-Sn pairs in the 128-atom SQSs used in our electronic structure calculations. The actual number of Sn-Sn pairs that occur in the SQSs is in all cases equal to the expected number $128 \times 2x^2$, rounded to the nearest whole number. We note that the probability of occurrence of a larger cluster containing three neighbouring Sn atoms is $\propto x^3$, which remains $\lesssim 10^{-3}$ in the composition range considered. Hence we expect, and find, that no Sn clusters containing more than two neighbouring Sn atoms occur

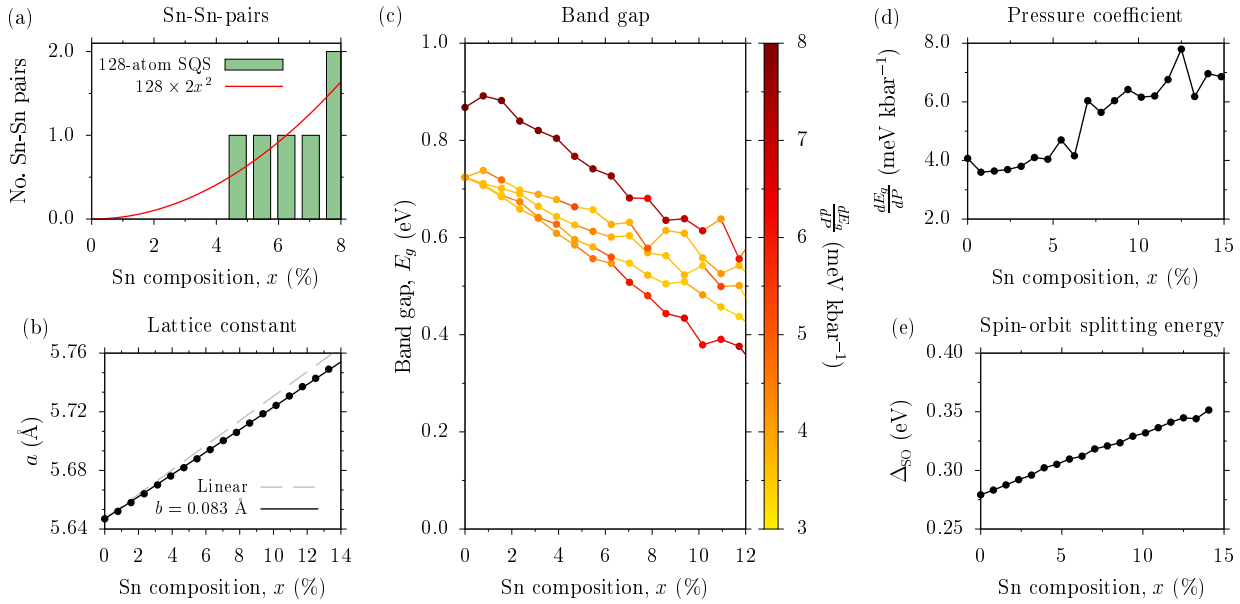


FIGURE 4.8: (a) Expected (solid red line) and actual (solid green bars) occurrence of nearest-neighbour Sn-Sn pairs in the 128-atom ($4 \times 4 \times 4$ FCC) SQSs used to analyse the electronic structure evolution in disordered $\text{Ge}_{1-x}\text{Sn}_x$ alloys. (b) Variation of the relaxed lattice constant a with Sn composition x (closed circles) for the SQSs of (a). The dashed grey line shows a calculated by interpolating linearly between the lattice constants of Ge and diamond-structured Sn (cf. Table 4.2). The solid black line shows the best fit to the calculated lattice constants, having bowing parameter $b = 0.076 \text{ \AA}$. (c) Variation with x of the band gaps E_g , calculated between the VB edge and the five lowest energy CB states at the supercell zone centre (closed circles). The colour of the data points are weighted according to the pressure coefficient $\frac{dE_g}{dP}$ associated with the corresponding band gap E_g . (d) Variation of $\frac{dE_g}{dP}$ with x for the fundamental band gap of (c). (e) Variation of the VB spin-orbit splitting energy Δ_{SO} with x .

in the SQSs employed in our analysis here. On this basis, we conclude that the 128-atom SQSs considered here have appropriate distributions of Sn atoms to analyse the evolution of the alloy properties with x .

The closed circles in Fig. 4.8(b) show the variation of the relaxed lattice constant a with x for the series of SQSs investigated. Comparing the calculated values of a to the increase expected based on Végard's law (dashed grey line), we observe that the lattice constants calculated for SQSs containing > 1 Sn atom are lower in value than those expected based on a linear interpolation of the Ge and α -Sn lattice constants. This suggests a positive bowing coefficient b for the lattice constant of disordered $\text{Ge}_{1-x}\text{Sn}_x$. Fitting to the calculated lattice constants – depicted by the solid black line in Fig. 4.8(b) – yields a best-fit bowing coefficient $b = 0.083 \text{ \AA}$. We note that this is in contrast to the results of our calculations in Sec. 4.3.2, where relaxation of ordered alloy supercells predicted a negative value of b , and likely reflects that the presence of Sn-Sn pairs and disorder leads to larger local expansion of sections of the crystal lattice. Given that (i) real $\text{Ge}_{1-x}\text{Sn}_x$ alloy samples will inevitably contain varying degrees of atomic-scale disorder, and (ii) SQSs are generally found to accurately predict the evolution with composition of the structural and elastic properties of randomly disordered alloys, [173] we expect that $b = 0.083$

$\mathring{\text{A}}$ represents a realistic prediction of the lattice constant bowing in $\text{Ge}_{1-x}\text{Sn}_x$ alloys. We note that this bowing parameter is similar to literature values of $-0.17 \mathring{\text{A}}$ calculated by D'Costa et al. [174] and $-0.21 \mathring{\text{A}}$ calculated by Eckhardt et al. [124] for $\text{Ge}_{1-x}\text{Sn}_x$ alloys.

Turning our attention to the electronic structure evolution, Fig. 4.8(c) shows the calculated variation with x of the band gaps between the alloy VB edge and the five lowest energy CB states at the supercell zone centre. Here, we show the band gaps calculated for the five (Kramers degenerate) lowest energy CB states in each SQS: for $x = 0$ the four lowest energy states are the L_{6c} CB minimum states of Ge, while the fifth is the Γ_{7c} zone-centre CB edge state of Ge. As in Sec. 4.6, due to the loss of cubic symmetry and associated lifting of the degeneracy of the VB edge states, we calculate band gaps with respect to the average energy of the two highest energy sets of Kramers degenerate VBs. At first glance, Fig. 4.8(c) seems to suggest that the indirect- to direct-gap transition occurs for $x \approx 7\%$, around which composition we observe four (Kramers degenerate) CB states lying within ≈ 100 meV of one another, with one state lying ≈ 60 meV below these four higher energy states. In this figure we have weighted the colour of each of the data points in Fig. 4.8(c) according to the corresponding calculated pressure coefficient $\frac{dE_g}{dP}$: starting from yellow for $\frac{dE_g}{dP} = 3$ meV kbar $^{-1}$ (close to that of the Ge L_{6c} - Γ_{8v} fundamental band gap), and shifting towards red as $\frac{dE_g}{dP}$ (i.e. direct character of the band gap) increases. Considering then $\frac{dE_g}{dP}$ associated with each band gap, we find that the lowest conduction band state has taken on some Ge Γ_{7c} character while the second to fifth lowest energy CB states retain predominantly Ge L_{6c} character for $x \approx 7\%$. As such, the alloy band gap has become primarily direct in nature for $x \approx 7\%$.

Generally speaking the trends observed in Fig. 4.8(c) remain largely consistent with those observed earlier in the chapter for the ordered supercells of $\text{Ge}_{1-x}\text{Sn}_x$ investigated in Sec. 4.4, where we found that the CB states originating from the L_{6c} states of Ge split into (Kramers degenerate) triplet and singlet states, respectively possessing primarily p - and s -like orbital character at Sn lattice sites, with the singlet states lying above the triplet state in energy. Due to the loss of cubic symmetry in the disordered supercells considered here we observe a breakdown of the degeneracy of the p -like Ge L_{6c} -derived triplet states. These states otherwise remain closely spaced in energy with increasing Sn composition x . We note additionally that alloy CB states originating from the Γ_{7c} states of Ge decrease in energy more rapidly with increasing x than those originating from the Ge L_{6c} states. As x increases the calculated CB states originating from the Γ_{7c} states of Ge firstly pass through the s -like Ge L_{6c} -derived CB state, at around $x \approx 4.7\%$. As this occurs we note weak hybridisation between these two sets of states, evidenced by the abrupt rise and subsequent fall in the values of $\frac{dE_g}{dP}$ associated with the s -like singlet CB states. As x increases further, we note the emergence of a direct band gap for $x \approx 7.03\%$. This is evidenced by a notable increase in $\frac{dE_g}{dP}$ associated with the fundamental

band gap as the energy of the Ge Γ_{7c} -derived CB states approaches that of the s -like Ge L_{6c} -derived singlet states. This increase in $\frac{dE_g}{dP}$ describes the transition to the fundamental band gap having primarily, but not purely, direct (Ge Γ_{7c}) character.

Finally, Fig. 4.8(e) shows the calculated variation of Δ_{SO} with x . As for the calculation of E_g above, Δ_{SO} is calculated with respect to the average VB edge energy. Still, we note deviations from a smooth monotonic increase of Δ_{SO} with x , likely reflecting the non-monotonic variation with x of the VB edge splitting. Generally, we find that Δ_{SO} increases steadily with increasing x , and is in line with corresponding increase calculated in Sec. 4.3.2 for ordered alloy supercells. For example, the calculated value $\Delta_{SO} = 0.316$ eV for an ordered $\text{Ge}_{15}\text{Sn}_1$ ($x = 6.25\%$) supercell is only 7meV smaller than the value of 0.323 eV calculated for the SQS of the same Sn composition $\text{Ge}_{120}\text{Pb}_8$ ($x = 6.25\%$).

4.7 Conclusions

In summary, we have presented three atomistic models of the structural and electronic properties of $\text{Ge}_{1-x}\text{Sn}_x$ alloys. The first model uses HSEsol DFT to perform structural relaxation and to calculate the electronic structure. This provides a highly accurate description of (i) the constituent materials Ge, α -Sn and zb-GeSn, and (ii) the hybridised nature of the $\text{Ge}_{1-x}\text{Sn}_x$ CB edge states. The second model uses LDA structural relaxation combined with mBJ electronic structure calculations. The third, semi-empirical model uses VFF structural relaxation combined with sp^3s^* TB electronic structure calculations. Since the HSEsol DFT calculations are in good quantitative agreement with experimental measurements, the results of these calculations were taken as a reference to quantify the accuracy of the LDA + mBJ and VFF + TB models.

The trends in the $\text{Ge}_{1-x}\text{Sn}_x$ alloy lattice constant, relaxed atomic positions, band gap and VB spin-orbit splitting energy calculated using the LDA + mBJ and VFF + TB models were found to be in good qualitative and quantitative agreement with the results of full HSEsol calculations. Alloy supercell band structure calculations carried out using all three models highlight the importance of Sn-induced band mixing and alloy disorder in determining the hybridised nature of the $\text{Ge}_{1-x}\text{Sn}_x$ CB structure in the supercells considered. This supports the suggestion that the evolution of a direct band gap in $\text{Ge}_{1-x}\text{Sn}_x$ occurs continuously with increasing Sn composition. As it offers an experimentally measureable means by which to quantify this hybridisation, the alloy band gap pressure coefficient was also calculated using the three approaches. Again, the LDA + mBJ and VFF + TB calculations were found to capture both qualitatively and quantitatively the trends observed in full HSEsol calculations.

On the basis of these benchmark calculations we conclude that the LDA + mBJ model offers an accurate description of $\text{Ge}_{1-x}\text{Sn}_x$ alloys at reduced computational expense compared to HSEsol calculations, providing access to larger systems within a first principles framework.

Investigations of the impact of Sn-Sn separation on the alloy band structure indicate the important impact of disorder effects on the electronic band structure. We note that the impact of these effects is likely overestimated due to long range periodic ordering effects arising from the small size of the supercells investigated and so anticipate that as the size of the supercell increases the impact of disorder effects will be lessened.

The results of the 128 atoms SQS supercells with x varied between 0 and 15% indicate an uptake in Gamma character in the lowest conduction band state at compositions of $\approx 5.5\%$ Sn content. At this $\approx 5.5\%$ Sn content the pressure coefficient of the conduction band edge remains primarily composed of band character arising from the Ge L_{6c} states having strong s -like orbital character at the Sn lattice sites, but also contains an admixture of Ge Γ_{7c} character. The level of Gamma character in the conduction band edge pressure coefficient continues to increase monotonically with the conduction band edge, becoming primarily Gamma-like at $\approx 7.03\%$ Sn.

Overall, we conclude that electronic structure calculations for $\text{Ge}_{1-x}\text{Sn}_x$ alloys must explicitly include band mixing and disorder effects to allow for accurate analysis of the impact of Sn incorporation on key material parameters, including optical transition strengths, electron mobility and band-to-band tunneling rates. Given the potential importance of these effects in determining technologically relevant material properties, the development of appropriate theoretical models represents an important step to enable predictive theoretical analysis of proposed $\text{Ge}_{1-x}\text{Sn}_x$ -based photonic, electronic and photovoltaic devices. The theoretical models we have presented allow for the treatment of larger systems than those accessible to hybrid functional DFT with minimal loss of accuracy, providing a basis for direct atomistic calculations of the electronic, optical and transport properties of disordered $\text{Ge}_{1-x}\text{Sn}_x$ alloys and realistically-sized nanostructures.

Chapter 5

Electronic and optical properties of GePb alloys

5.1 Overview

Having investigated in previous chapters the optical and electrical properties of $\text{Ge}_{1-x}\text{Sn}_x$ alloys, we turn our attention in this chapter to another group-IV element lead (Pb) and its ability to bring about a direct band gap in germanium via alloying with low % compositions of lead. In this chapter, we present a theoretical analysis of electronic structure evolution in $\text{Ge}_{1-x}\text{Pb}_x$ alloys, using first principles DFT calculations. Our alloy supercell calculations firstly demonstrate that Pb incorporation strongly impacts the CB structure. Our analysis further reveals a strong Pb-induced reduction of the fundamental band gap and increase of the VB spin-orbit splitting energy, as well as a strong sensitivity of the alloy CB structure to the presence of atomic-scale alloy disorder (Pb clustering). From a theoretical perspective, the presence of such alloying effects indicates a breakdown of the virtual crystal approximation (VCA), upon which previous analysis [175] of the indirect- to direct-gap transition has been based.

We then discuss our results in comparison to the results of equivalent calculations for $\text{Ge}_{1-x}\text{Sn}_x$ alloys reported in chapter 4. We demonstrate that the electronic structure evolution in $\text{Ge}_{1-x}\text{Pb}_x$ admits important quantitative differences compared to that in $\text{Ge}_{1-x}\text{Sn}_x$. Confirming the strong impact of Pb incorporation on the band structure, we firstly calculate that Pb incorporation results in a strong reduction of the fundamental band gap, by ≈ 100 meV per % Pb replacing Ge. Secondly, the band gap becomes direct in character with increasing x , but the alloy CB edge eigenstates in our supercell calculations are in general neither purely indirect nor direct in character, but predominantly contain an admixture of indirect (Ge L_{6c}) and direct (Ge Γ_{7c}) character. The indirect- to direct-gap transition instead proceeds via the downward

shift in energy of CB states originating from the Ge Γ_{7c} states, which pass through – and in doing so hybridise weakly with – alloy CB states originating from the Ge L_{6c} states. We find in our 128-atom special quasi-random structure (SQS) calculations a relatively abrupt indirect-to-direct-gap transition, occurring in a narrow composition range centred about $x \approx 7\%$ in our calculations, close to the composition where we calculate that $\text{Ge}_{1-x}\text{Pb}_x$ becomes semimetallic. We note however that finite-size effects observed in our calculations may lead to an overestimate of this transition composition. Analysing these finite-size effects, we estimate the direct gap to shift below the inhomogeneously broadened indirect gap in $\text{Ge}_{1-x}\text{Pb}_x$ for $x \approx 3 - 4\%$.

The remainder of this chapter is organized as follows. We begin in Section 5.1.1 with a brief overview of existing literature on the experimental growth and theoretical investigation of the properties of $\text{Ge}_{1-x}\text{Pb}_x$ alloys and detail the potential applications for direct band gap $\text{Ge}_{1-x}\text{Pb}_x$ alloys in the photonics industry. Following this, in Section 5.2 we detail our first principles theoretical approach to calculating the structural and electronic properties of $\text{Ge}_{1-x}\text{Pb}_x$ alloy supercells, which is similar in methodology to the approach presented in Chapter 4 for $\text{Ge}_{1-x}\text{Sn}_x$ alloys and which consists of performing density functional theory calculations on large (up to $N = 128$ atom) $\text{Ge}_{1-x}\text{Pb}_x$ supercells in which the atomic positions in the supercell are, as described previously in Chapter 4, allowed to relax to their equilibrium positions (those at which the overall elastic energy in the supercell is minimised) and electronic structure and hydrostatic pressure calculations are then employed on the relaxed structure to investigate the electronic properties of the alloy at varying composition of lead. The generation of the special quasi random structures used in our analysis of disordered alloys, and the calculation of the alloy band structure as a function of hydrostatic pressure to determine the hybridised character of the CB edge states are also reiterated briefly here.

The results of our calculations are presented in Sec. 5.3, beginning in Sec. 5.3.1 with an analysis of the impact of Pb incorporation on the electronic structure of ordered $\text{Ge}_{1-x}\text{Pb}_x$ alloy supercells. In Sec. 5.3.2 we quantify the importance of the local environment around a substitutional Pb atom, via analysis of the impact of nearest-neighbour Pb-Pb pair formation on the electronic structure. Then, in Sec. 5.3.3 we analyse the evolution of the electronic structure with x in 128-atom disordered (SQS) alloy supercells. We present a theoretical analysis of electronic structure evolution and the indirect- to direct-gap transition in the group-IV alloy $\text{Ge}_{1-x}\text{Pb}_x$, based on density functional theory employing both Heyd-Scuseria-Ernzerhof (HSE) hybrid functional and modified Becke-Johnson (mBJ) exchange-correlation functionals. Due to similarities in the impact of Pb and Sn incorporation on the Ge band structure, we discuss in Sec. 5.3.4 our results in comparison to the results of equivalent calculations for $\text{Ge}_{1-x}\text{Sn}_x$ alloys described in Chapter 4. We demonstrate that the electronic structure evolution in $\text{Ge}_{1-x}\text{Pb}_x$ admits important quantitative differences compared to that in $\text{Ge}_{1-x}\text{Sn}_x$.

Finally, in Sec. 5.4 we summarise and conclude.

5.1.1 Review of existing literature for GePb alloys

While $\text{Ge}_{1-x}\text{Sn}_x$ alloys have attracted significant theoretical interest, there have been few reports to date regarding $\text{Ge}_{1-x}\text{Pb}_x$ alloys. Initial density functional theory (DFT) calculations by Huang et al. [175] predicted (i) a strong band gap reduction in response to Pb incorporation, (ii) that the indirect- to direct-gap transition occurs for Pb compositions as low as $x \approx 1\%$, and (iii) that the alloy band gap closes for $x \approx 2\%$. However, these calculations possess several shortcomings. Firstly, the conduction band (CB) minimum of Ge in Ref. [175] lies along the Δ direction in the Brillouin zone, rather than at the L point. Secondly, the use of a local density approximation (LDA) exchange-correlation (XC) functional leads to band gap underestimation. More recently, the same authors presented calculations based on a more accurate GGA + U XC functional, and revised the predicted Pb composition for the transition to a direct gap to $x \approx 3.5\%$. [45] However, little work has yet been undertaken to analyse the indirect- to direct-gap transition, and its implications for the alloy electronic structure and for device applications.

On the experimental side initial epitaxial growth of GePb films has been reported, involving decomposition by sputtering of Ge and Pb and annealing via laser induced epitaxy [176–178]. TEM images from these initial studies suggest that substitutional incorporation of up to 3% Pb content can be achieved by this method. Given the recent establishment of epitaxial growth of $\text{Ge}_{1-x}\text{Pb}_x$ alloys, and experimental evidence for the emergence of a direct band gap, [178] detailed theoretical insight into the alloy electronic structure is required to guide the development of suitable materials for potential device applications.

5.2 Theoretical models

Our analysis of the $\text{Ge}_{1-x}\text{Pb}_x$ electronic structure is based on DFT calculations employing two distinct exchange-correlation (XC) functionals: (i) the Heyd-Scuseria-Ernzerhof (HSE) hybrid XC functional [78, 79] modified for solids (HSEsol), [134] and (ii) the modified Becke-Johnson (mBJ) XC functional. [75] The semi-core d states of Ge are treated as core electron states, unfreezing these states has been demonstrated to have a negligible impact on the calculated electronic structure. [124] We adopt the same approximation for Pb. We therefore employ pseudopotentials in which the $(4s)^2(4p)^2$ orbitals of Ge and $(6s)^2(6p)^2$ orbitals of Pb are explicitly treated as valence states. Since relativistic effects in Pb are sufficiently large to impact the structural properties [179] – e.g. calculations neglecting spin-orbit coupling incorrectly predict that elemental Pb is diamond-structured rather than FCC-structured in equilibrium – spin-orbit coupling is explicitly included in the computation of the lattice free energy for all

structural relaxations. All DFT calculations were performed using the projector augmented-wave method, [85, 93] as implemented in the Vienna Ab-initio Simulation Package (VASP). [95, 96]

5.2.1 Density Functional Theory

Our DFT calculations are based closely on those we have established recently for $\text{Ge}_{1-x}\text{Sn}_x$ alloys, full details of which can be found in the theoretical methods section in Chapter 2 and Chapter 4 of this thesis. Since Pb incorporation is found to strongly impact the Ge band structure close in energy to the CB edge, and since we are interested in the transition from an indirect to direct band gap in $\text{Ge}_{1-x}\text{Pb}_x$ at low Pb compositions $x \lesssim 10\%$, we prioritise the accuracy of the description of the Ge band structure close in energy to the CB edge. As before for the HSEsol calculations we therefore treat the exact exchange mixing α as an adjustable parameter, the value of which is chosen to reproduce the measured separation in energy between the fundamental indirect L_{6c} - Γ_{8v} and direct Γ_{7c} - Γ_{8v} band gaps of Ge. Similarly for the mBJ calculations the relative weight c of the conventional Becke-Johnson exchange potential is treated as an adjustable parameter, the value of which is chosen again to reproduce the measured separation in energy between the fundamental indirect L_{6c} - Γ_{8v} and direct Γ_{7c} - Γ_{8v} band gaps of Ge. We find for the HSE and mBJ exchange correlation functionals that setting $\alpha = 0.3$ in the HSEsol and $c = 1.2$ in the mBJ XC functionals respectively optimally reproduce the measured 146 meV Γ_{7c} - L_{6c} energy difference. [155, 180] For the HSEsol calculations we again use a screening parameter $\mu = 0.2 \text{ \AA}^{-1}$.

For primitive unit cells we utilise a Γ -centred $6 \times 6 \times 6$ Monkhorst-Pack \mathbf{k} -point grid for Brillouin zone integration, which is downsampled appropriately for larger supercells in order to preserve the resolution of the Brillouin zone sampling. A plane wave cut-off energy of 400 eV is used for

TABLE 5.1: Lattice constant a , direct Γ_{7c} - Γ_{8v} band gap E_g and VB Γ_{8v} - Γ_{7v} spin-orbit splitting energy Δ_{SO} for Ge, diamond-structured Pb (d-Pb) and zinc blende GePb (zb-GeSn), calculated via DFT using the HSEsol (with $\alpha = 0.3$), and LDA (for a) or mBJ (with $c = 1.2$, for E_g and Δ_{SO}) XC functionals, and compared to low-temperature experimental measurements and previous first principles theoretical calculations. For Ge the fundamental (indirect) L_{6c} - Γ_{8v} band gap is listed in parentheses.

Material	a (\AA)			E_g (eV)			Δ_{SO} (eV)		
	HSEsol	LDA	Reference	HSEsol	mBJ	Reference	HSEsol	mBJ	Reference
Ge	5.653	5.649	5.657 ^a , 5.648 ^b	0.908 (0.765)	0.868 (0.724)	0.890 (0.744) ^c	0.322	0.274	0.296 ^c
d-Pb	6.907	6.852	6.673 ^d , 7.074 ^e	-5.329	-4.605	—	2.422	1.999	2.377 ^f
zb-GePb	6.317	6.297	6.154 ^d , 6.265 ^g	-2.695	-2.407	-2.250 ^g	1.123	1.029	0.930 ^g

^aMeas. (avg.), Ref. Landolt and Börnstein [32] ^bCalc. (avg.), Ref. Landolt and Börnstein [32]

^cCalc. (avg.), Ref. Landolt and Börnstein [155] ^dCalc., Ref. Wang and Ye [181]

^eCalc. (avg.), Ref. Hermann et al. [154] ^fCalc., Ref. Herman et al. [64] ^gCalc., Ref. Hammou et al. [182]

all calculations, chosen to be sufficiently high to minimise Pulay stress and allow for accurate structural relaxation. Structural relaxation is achieved via free energy minimisation, by allowing the lattice vectors and ionic positions to relax freely, subject to the additional criterion that the maximum force on any atom in the supercell does not exceed 0.01 eV \AA^{-1} . To generate relaxed atomic positions for HSEsol and mBJ electronic structure calculations, the HSEsol and LDA XC functionals respectively are used to perform structural relaxations. Since relativistic effects in Pb are sufficiently large to impact the structural properties [179] – e.g. calculations neglecting spin-orbit coupling incorrectly predict that elemental Pb is diamond-structured rather than FCC-structured in equilibrium – spin-orbit coupling is explicitly included in the computation of the lattice free energy for all structural relaxations.

Table 5.1 summarises the results of our DFT calculations for the three constituent crystalline materials relevant to $\text{Ge}_{1-x}\text{Pb}_x$ – diamond-structured semiconducting Ge ($x = 0$), diamond-structured semimetallic [154] Pb (d-Pb; $x = 1$), and the fictitious semimetallic zinc blende-structured IV-IV compound GePb (zb-GePb; $x = 0.5$). The table lists calculated lattice constants a , direct band gaps E_g , and valence band (VB) spin-orbit splitting energies Δ_{SO} , compared to (low temperature) experimental measurements and previous theoretical calculations. The band structures of Ge, d-Pb and zb-GePb, calculated using the HSEsol (solid lines) and mBJ (dashed lines) XC functionals, are shown respectively in Figs. 5.1(a), 5.1(b) and 5.1(c). We note that zb-GePb – equivalent to an ordered $\text{Ge}_{0.5}\text{Pb}_{0.5}$ alloy – is semimetallic, with a large negative direct band gap -2.695 eV (-2.407 eV) in the HSEsol (mBJ) calculation, suggesting that the band gap in $\text{Ge}_{1-x}\text{Pb}_x$ alloys can be expected to close for some Pb composition significantly below 50%.

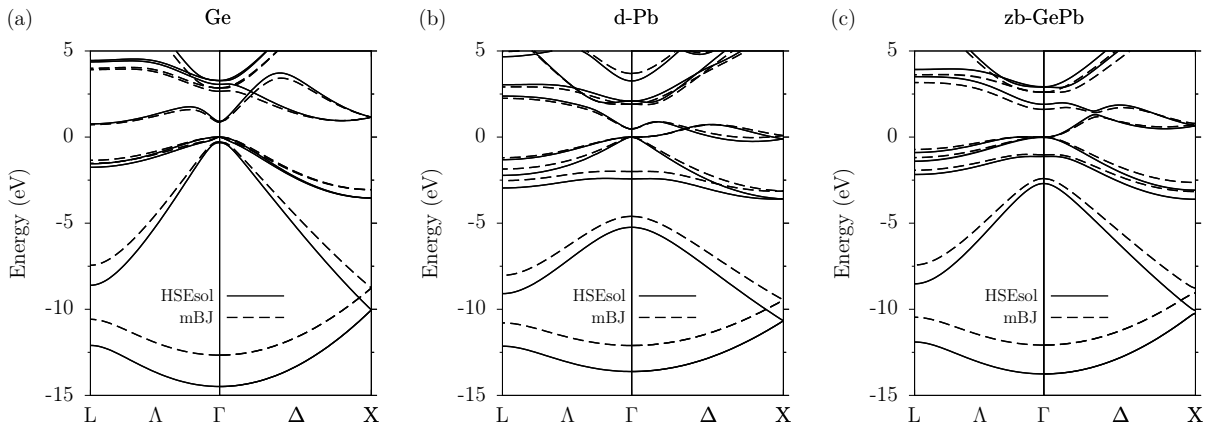


FIGURE 5.1: Band structure of (a) Ge, (b) diamond-structured Pb (d-Pb), and (c) zinc blende GePb (zb-GePb), calculated via DFT using the HSEsol (solid lines) and mBJ (dashed lines) XC functionals. For comparative purposes, the zero of energy has been chosen to lie at the energy of the Γ_{8v} VB edge in all cases.

5.2.2 Choice of supercells

States originating from different wave vectors \mathbf{k} in the Brillouin zone of the primitive unit cell of the underlying diamond lattice are folded back to the zone centre ($\mathbf{K} = 0$) in supercell calculations. It can therefore be difficult to identify the character of individual zone-centre states in the band structure of a $\text{Ge}_{1-x}\text{Pb}_x$ supercell, and hence to deduce the composition at which the alloy becomes a direct-gap semiconductor. To address this issue, we again investigate how the alloy CB structure changes as hydrostatic pressure is applied. Calculation of the pressure coefficient $\frac{dE_g}{dP}$ for the fundamental band gap in a given alloy supercell then allows to identify the character of the band gap, and hence to track the evolution of the character of the CB edge states and band gap with increasing Pb composition x . Because the $\text{Ge}_{1-x}\text{Pb}_x$ alloy CB edge states originate from the L_{6c} CB edge states of Ge, for small x , we follow Ref. [180] and restrict our attention to supercells in which mixing between L- and Γ -point eigenstates is permitted to occur. That is, we restrict our attention to $n \times n \times n$ face-centred cubic (FCC) or simple cubic (SC) supercells having even values of n . In such supercells the L points in the Brillouin zone of the underlying diamond primitive unit cell fold to the supercell zone centre $\mathbf{K} = 0$, with L-point eigenstates then being free to hybridise with those at Γ under the influence of the structural and chemical changes associated with Pb incorporation.

quasi-random structures

5.2.3 Special quasi random structures

As detailed previously in Section 4.2 we employ special quasi random structures to seed our disordered alloy supercells so as to best capture the electronic structure of the most probable configuration of germanium and lead atoms in these supercells with varying % lead content.

Similarly to the $\text{Ge}_{1-x}\text{Sn}_x$ SQSs investigated in the previous chapter, a series of 128-atom ($4 \times 4 \times 4$ FCC) SQSs are employed here for the investigation of $\text{Ge}_{1-x}\text{Pb}_x$ alloys up to 10 Pb atoms – i.e. Pb compositions up to $x = 7.81\%$. The SQSs are generated stochastically, using a Monte Carlo simulated annealing procedure – as implemented in the Alloy Theoretic Automated Toolkit (ATAT) [160–162] – to optimise the supercell lattice correlation functions up to third nearest-neighbour distance about each lattice site, with respect to the target lattice correlation functions for a randomly disordered, diamond-structured alloy having a specified Pb composition x [163, 164]. In practice, the SQS supercells used here have the same atomic distribution as were used for $\text{Ge}_{1-x}\text{Sn}_x$ calculations in the previous chapter.

5.3 Electronic properties of germanium-lead alloys

In this section we present the results of our theoretical analysis. We begin in Sec. 5.3.1 with the impact of Pb incorporation on the electronic structure of ordered alloy supercells, and demonstrate the transition to a direct band gap with increasing Pb composition x . We compare the results of calculations undertaken using both the HSEsol and mBJ XC functionals, establishing the accuracy of the latter for use in further analysis. In Sec. 5.3.2 we turn our attention to disordered supercells, and illustrate the importance of alloy disorder in $\text{Ge}_{1-x}\text{Pb}_x$ by tracking the evolution of the alloy CB edge as the separation between two Pb atoms reduces from their being fourth-nearest neighbours, to their forming a nearest-neighbour Pb-Pb pair. In Sec. 5.3.3 we use 128-atom SQSs to analyse the evolution of the electronic structure with Pb composition x and to quantify the nature of the indirect- to direct-gap transition in realistic, disordered supercells. Finally in Sec. 5.3.4 we compare these results for the $\text{Ge}_{1-x}\text{Pb}_x$ alloys to the results of equivalent calculations for $\text{Ge}_{1-x}\text{Sn}_x$ alloys described in Chapter 4. We detail the important quantitative differences in electronic structure evolution in $\text{Ge}_{1-x}\text{Pb}_x$ compared to that in $\text{Ge}_{1-x}\text{Sn}_x$.

5.3.1 Conduction band structure and Pb-induced band mixing in ordered germanium-lead supercells

We begin our analysis by considering the structural and electronic properties of ordered $\text{Ge}_{63}\text{Pb}_1$ ($x = 1.56\%$, $2 \times 2 \times 2$ SC) and $\text{Ge}_{15}\text{Pb}_1$ ($x = 6.25\%$, $2 \times 2 \times 2$ FCC) alloy supercells. Considering the data of Table 5.1, we note that the lattice constant of zb-GePb is lower than the average of those calculated for Ge and Pb, using both the LDA and HSEsol XC functionals. This suggests that the $\text{Ge}_{1-x}\text{Pb}_x$ alloy lattice constant deviates from that predicted based on Végard's law (linear interpolation), and possesses a positive bowing coefficient b , where $a(x) = (1-x)a(\text{Ge}) + xa(\text{d-Pb}) - bx(1-x)$ is the $\text{Ge}_{1-x}\text{Pb}_x$ alloy lattice constant. Examining the alloy lattice constants obtained via structural relaxation of the $\text{Ge}_{63}\text{Pb}_1$ supercell, we find that this is indeed the case.

Using the LDA and HSEsol XC functionals we calculate lattice constants $a = 5.666 \text{ \AA}$ and $a = 5.667 \text{ \AA}$ respectively, which are lower than the values of 5.668 \AA and 5.673 \AA obtained via linear interpolation between the calculated lattice constants of Ge and Pb for LDA and HSEsol respectively. On the basis of the LDA and HSEsol relaxed lattice constants we then compute a bowing parameters of $b = 0.13 \text{ \AA}$ and $b = 0.39 \text{ \AA}$. Similar trends are observed in the relaxed lattice constants for the $\text{Ge}_{15}\text{Pb}_1$ supercell. Overall, our calculations suggest bowing in the range $b \approx 0.1 - 0.4 \text{ \AA}$ for these ordered structures having low Pb compositions $x \leq 6.25\%$. We will see in Sec. 5.3.3 below that this result is modified in the presence of alloy disorder, producing a change in the sign of b .

TABLE 5.2: Fundamental band gap E_g , VB spin-orbit splitting energy Δ_{SO} , and band gap pressure coefficient $\frac{dE_g}{dP}$ for ordered $\text{Ge}_{63}\text{Pb}_1$ ($x = 1.56\%$) and $\text{Ge}_{15}\text{Pb}_1$ ($x = 6.25\%$) alloy supercells, calculated via DFT using the HSEsol and mBJ XC functionals. The corresponding calculated values of the direct $\Gamma_{7c}-\Gamma_{8v}$ and indirect (fundamental) $L_{6c}-\Gamma_{8v}$ band gaps of Ge are provided for reference, with the latter listed in parentheses. The results of equivalent calculations [180] for ordered $\text{Ge}_{1-x}\text{Sn}_x$ supercells are provided for comparative purposes.

Supercell	x (%)	E_g (eV)		Δ_{SO} (eV)		$\frac{dE_g}{dP}$ (meV kbar $^{-1}$)	
		HSEsol	mBJ	HSEsol	mBJ	HSEsol	mBJ
Ge	—	0.909 (0.766)	0.868 (0.724)	0.322	0.274	13.33 (4.66)	13.23 (4.07)
$\text{Ge}_{63}\text{Pb}_1$	1.56	0.616	0.596	0.381	0.334	6.24	5.68
$\text{Ge}_{63}\text{Sn}_1$	1.56	0.681 ^a	0.660 ^a	0.334 ^a	0.282 ^a	4.75 ^a	4.19 ^a
$\text{Ge}_{15}\text{Pb}_1$	6.25	0.020	-0.040	0.612	0.571	10.23	9.17
$\text{Ge}_{15}\text{Sn}_1$	6.25	0.388 ^a	0.356 ^a	0.379 ^a	0.316 ^a	10.00 ^a	9.50 ^a

^aRef. O'Halloran et al. [180]

Turning our attention now to the calculated electronic structure of these supercells, Table 5.2 shows the calculated fundamental band gaps E_g , VB spin-orbit splitting energies Δ_{SO} , and fundamental band gap pressure coefficients $\frac{dE_g}{dP}$. The results of equivalent calculations [180] for $\text{Ge}_{1-x}\text{Sn}_x$ supercells are provided for comparative purposes.

The HSEsol- (mBJ-) calculated band structures of the $\text{Ge}_{63}\text{Pb}_1$ and $\text{Ge}_{15}\text{Pb}_1$ supercells are shown using solid (dashed) lines in Figs. 5.2(b) and 5.2(e), respectively. For reference, the band structures of the corresponding Pb-free Ge_{64} and Ge_{16} supercells are shown in Figs. 5.2(a) and 5.2(d). Since the 64-atom supercells have SC lattice vectors, we note that the zone boundary along the (001) direction lies at supercell wave vector $K_z = \frac{\pi}{A}$, where $A = 2a$ is the supercell lattice constant for a 64-atom $2 \times 2 \times 2$ SC supercell. The corresponding zone boundary lies at $K_z = \frac{2\pi}{A}$ for a 16-atom $2 \times 2 \times 2$ FCC supercell.

For the $\text{Ge}_{63}\text{Pb}_1$ supercell the HSEsol- (mBJ-) calculated band gap $E_g = 0.616$ eV (0.596 eV) is reduced by 150 meV (128 meV) compared to the fundamental band gap of Ge. We also calculate a strong increase in Δ_{SO} of 59 meV (60 meV) due to Pb incorporation, with Δ_{SO} increasing from 0.322 eV (0.274 eV) in Ge, to 0.381 eV (0.334 eV) in $\text{Ge}_{63}\text{Pb}_1$. It is evident based on these results that incorporation of Pb leads to a very strong decrease in E_g , of $\approx 80 - 100$ meV per % Pb, and a strong increase in Δ_{SO} , of ≈ 40 meV per % Pb. Indeed, for the $\text{Ge}_{15}\text{Pb}_1$ supercell the HSEsol- (mBJ-) calculated band gap $E_g = 0.020$ eV (-0.040 eV) indicates a closing of the alloy band gap for Pb compositions as low as $x = 6.25\%$. The corresponding VB spin-orbit splitting energies $\Delta_{\text{SO}} = 0.612$ eV (0.571 eV) are far in excess of the band gap, suggesting a crossover to a band structure in which $\Delta_{\text{SO}} > E_g$ for low Pb compositions $x \lesssim 5\%$. We note that these values are significantly in excess of the changes in E_g and Δ_{SO} associated with Sn incorporation (cf. Table 5.2), reflecting the larger differences in size and chemical properties between Ge and Pb than between Ge and Sn.

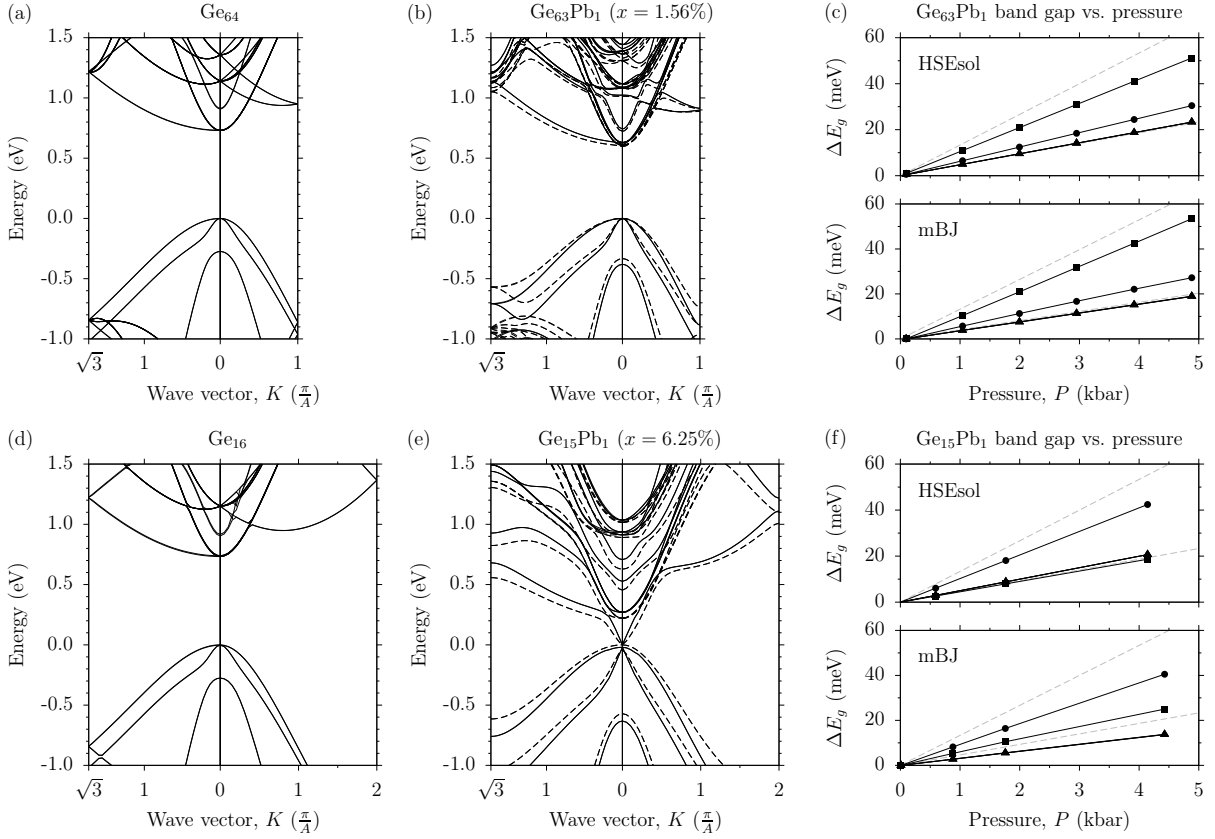


FIGURE 5.2: Band structure of (a) Ge_{64} ($2 \times 2 \times 2$ SC), (b) $\text{Ge}_{63}\text{Pb}_1$ ($x = 1.56\%$), (d) Ge_{16} ($2 \times 2 \times 2$ FCC), and (e) $\text{Ge}_{15}\text{Pb}_1$ ($x = 6.25\%$), calculated via DFT using the HSEsol (solid lines) and mBJ (dashed lines) XC functionals. (c) Calculated change in band gap ΔE_g with applied hydrostatic pressure P for the $\text{Ge}_{63}\text{Pb}_1$ supercell of (b), calculated using the HSEsol (upper panel) and mBJ (lower panel) XC functionals. Band gaps are calculated between the VB edge and the first (circles), second, third and fourth (triangles), and fifth (squares) lowest energy CB states. (f) As in (c), but for the $\text{Ge}_{15}\text{Pb}_1$ supercell of (e). The lower (upper) dashed grey line in (c) and (f) denotes the variation with pressure of the indirect $L_{6c}-\Gamma_{8v}$ (direct $\Gamma_{7c}-\Gamma_{8v}$) band gap of Ge.

While the mBJ XC functional tends to underestimate E_g and Δ_{SO} compared to the HSEsol XC functional, we note that the changes in E_g and Δ_{SO} in response to Pb incorporation calculated using both approaches are in good quantitative agreement.

Considering now the calculated supercell band dispersion in Figs. 5.2(b) and 5.2(e), we note that Pb incorporation has a significant impact on the CB structure, while the main impact close in energy to the VB edge is, as noted above, to increase the spin-orbit splitting energy Δ_{SO} . The evolution of the band structure close in energy to the VB edge can be described using a conventional alloy approach (e.g. the VCA, with appropriate bowing coefficients for the VB edge energy and Δ_{SO}).

In Ge_{64} the CB states at the supercell zone centre $\mathbf{K} = 0$ are, in order of increasing energy: (i) the eightfold (fourfold and Kramers) degenerate folded L_{6c} L-point CB minimum states,

(ii) the twofold (Kramers) degenerate Γ_{7c} zone-centre CB edge states, and (iii) the twelvefold (sixfold and Kramers) degenerate folded X_{5c} X-point CB edge states.

In $\text{Ge}_{63}\text{Pb}_1$ we note a downward shift in energy, and lifting of the degeneracy, of the alloy CB edge states originating from the folded L_{6c} states of the Ge host matrix. We also calculate a significant reduction in energy of the alloy CB states originating from the Ge Γ_{7c} host matrix states, which is larger in magnitude than that associated with the alloy CB states originating from the L_{6c} states of Ge. We find that the lowest energy CB states in $\text{Ge}_{63}\text{Pb}_1$ are twofold (Kramers) degenerate, and possess purely s -like orbital character (A_1 symmetry) at the Pb lattice site. The second lowest energy CB states in this supercell lie 14 meV (11 meV) higher in energy in the HSEsol (mBJ) calculation, are sixfold (threefold and Kramers) degenerate and possess purely p -like orbital character (T_2 symmetry) at the Pb lattice site. The substitutional incorporation of the Pb atom also allows mixing between different Ge host matrix states of the same symmetry, so that the lowest energy CB state in $\text{Ge}_{63}\text{Pb}_1$ can be described in terms of a linear combination of Ge host matrix states which lie close in energy to the CB edge and possess A_1 symmetry at the Pb lattice site. We note that the splitting of the alloy CB states originating from the L_{6c} states of Ge is qualitatively similar to that in a $\text{Ge}_{63}\text{Sn}_1$ supercell. [180, 183] However, the ordering of these A_1 - and T_2 -symmetric Ge L_{6c} -derived alloy CB edge states is reversed in $\text{Ge}_{63}\text{Pb}_1$ compared to $\text{Ge}_{63}\text{Sn}_1$.

In $\text{Ge}_{15}\text{Pb}_1$ we note the same behaviour in terms of alloy CB state ordering, degeneracy and symmetry of the CB edge states: the Kramers degenerate alloy CB edge again possesses purely s -like orbital character at the Pb site, while the second lowest energy CB states are sixfold (threefold and Kramers) degenerate and possess purely p -like orbital character at the Pb site. We note however a significant increase of the separation in energy – 269 meV (260 meV) in the HSEsol (mBJ) calculation – between these sets of A_1 - and T_2 -symmetric states.

Consideration of the alloy band structure therefore allows the presence of Pb-induced and composition-dependent band mixing in the $\text{Ge}_{1-x}\text{Pb}_x$ CB, which is qualitatively similar to that which we have previously observed in $\text{Ge}_{1-x}\text{Sn}_x$ alloys. [180] To further investigate this band mixing, we have calculated the pressure coefficients associated with the band gaps between the alloy VB edge and the five lowest energy alloy CB states (which originate predominantly from the L_{6c} and Γ_{7c} states of Ge). Since we are concerned with low Pb compositions $x < 10\%$, it is expected that an alloy having an indirect (direct) band gap will have a pressure coefficient close to that of the corresponding indirect L_{6c} - Γ_{8v} (direct Γ_{7c} - Γ_{8v}) band gap of Ge. In practice, the band gap pressure coefficient $\frac{dE_g}{dP}$ encapsulates quantitative information describing any hybridisation of the alloy CB edge, providing an experimentally measurable signature of band mixing effects. Before considering the calculated values of $\frac{dE_g}{dP}$ for the alloy supercells of Fig. 5.2, we note that our respective HSEsol- (mBJ-) calculated pressure coefficients $\frac{dE_g}{dP} = 4.66$ meV kbar⁻¹ (4.07 meV kbar⁻¹) and 13.33 meV kbar⁻¹ (13.23 meV kbar⁻¹) for the indirect and

direct band gaps of Ge (cf. Table 5.2) are in good quantitative agreement with the measured values of 4.3 and 12.9 meV kbar⁻¹.

To compute $\frac{dE_g}{dP}$ we apply hydrostatic pressure by compressing the lattice vectors of a given relaxed supercell, and then perform geometric (re-)optimisation by allowing only the internal atomic degrees of freedom to relax. The results of our calculations of $\frac{dE_g}{dP}$ are summarised in Figs. 5.2(c) and 5.2(f), for the Ge₆₃Pb₁ and Ge₁₅Pb₁ supercells respectively. In each case the upper (lower) panel shows the results obtained using the HSEsol (mBJ) XC functional. We see in both cases that the pressure coefficient associated with the band gap between the sixfold degenerate states having *p*-like orbital character at the Pb lattice site and the alloy CB edge is very close to that of the Ge L_{6c}-Γ_{8v} fundamental band gap, confirming the Ge L_{6c}-like character of these states. For Ge₆₃Pb₁ the HSEsol- (mBJ-) calculated fundamental supercell band gap pressure coefficient $\frac{dE_g}{dP} = 6.24$ meV kbar⁻¹ (5.68 meV kbar⁻¹) is increased by ≈ 1.6 meV kbar⁻¹ compared to that of the fundamental indirect band gap of Ge, suggesting the presence of Pb-induced band mixing in the supercell between the A₁-symmetric Ge L_{6c} singlet, and the Ge Γ_{7c} zone-centre CB edge state (which has *s*-like orbital character at all lattice sites). The presence of this Pb-induced hybridisation is confirmed by noting that $\frac{dE_g}{dP}$ associated with the band gap between the VB edge and the fifth highest energy CB state – which originates from the Ge Γ_{7c} states, denoted using circles in Figs. 5.2(c) and 5.2(f) – is reduced compared to that of the Ge direct band gap, suggesting the acquisition of an admixture of Ge L_{6c} (and possibly also a minor admixture of Ge X_{5c} character). This Γ_{7c}-L_{6c} mixing occurs in part due to the small ≈ 145 meV separation in energy between these states in Ge. Considering the Ge₁₅Pb₁ pressure coefficients in Fig. 5.2(f), we see that the pressure coefficients associated with the band gaps between the VB edge and the second to fourth lowest energy CB states are again very close to that associated with the Ge L_{6c}-Γ_{8v}, but that the largest pressure coefficient of 10.23 meV kbar⁻¹ (9.17 meV kbar⁻¹) is now associated with the CB edge state (circles), indicating the evolution to a band gap which is hybridised but primarily direct in nature (with some Ge Γ_{7c} character also associated with the fifth lowest energy CB states).

Overall, our analysis of idealised (ordered) alloy supercells demonstrates that the electronic structure evolution and indirect- to direct-gap transition in Ge_{1-x}Pb_x is qualitatively similar to that in Ge_{1-x}Sn_x [180], but with alloy band mixing effects being less pronounced in Ge_{1-x}Pb_x compared to Ge_{1-x}Sn_x. Indeed, as we will demonstrate in Sec. 5.3.3 below, when alloy disorder is taken into account the band mixing associated with Pb incorporation is significantly less pronounced than the corresponding effects in Ge_{1-x}Sn_x, and hence plays a less important role in determining the nature and evolution of the alloy electronic structure with increasing *x*. Finally, having established that the mBJ XC functional gives results in good quantitative agreement with the more computationally expensive HSEsol XC functional, we employ the mBJ XC functional for the remainder of our analysis.

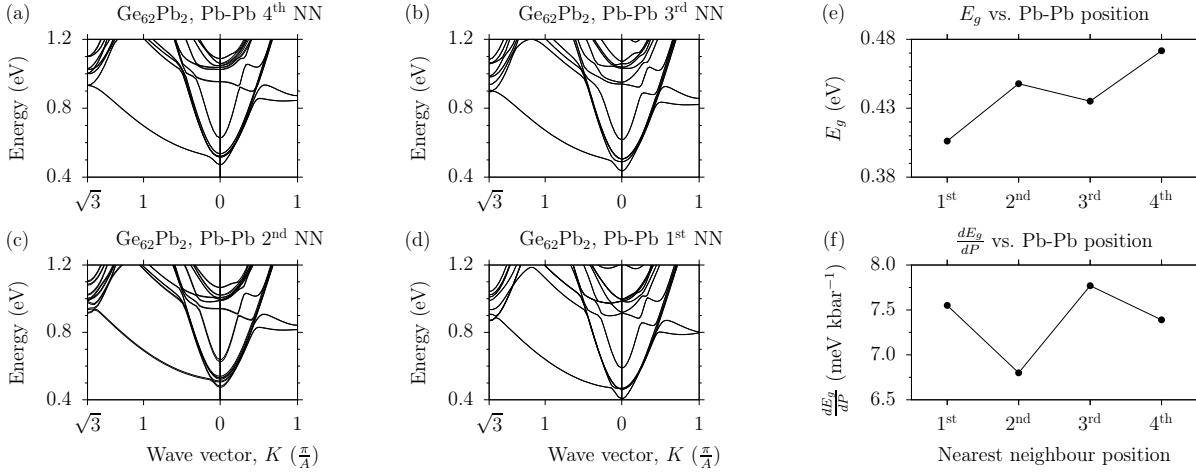


FIGURE 5.3: Calculated CB structure of disordered, 64-atom ($2 \times 2 \times 2$ SC) $\text{Ge}_{62}\text{Pb}_2$ ($x = 3.125\%$) supercells in which the two Pb atoms are (a) fourth, (b) third, (c) second, and (d) first nearest neighbours (NNs). (e) Calculated variation of the fundamental band gap E_g of the $\text{Ge}_{62}\text{Pb}_2$ supercells of (a) – (d) with respect to the relative position of the two Pb atoms. (f) as in (e), but for the pressure coefficient $\frac{dE_g}{dP}$ of the fundamental band gap E_g .

5.3.2 Impact of Pb local environment on germanium-lead alloy electronic structure

Having quantified the impact of Pb incorporation on the band structure of ordered $\text{Ge}_{1-x}\text{Pb}_x$ supercells, we turn our attention now to the impact of Pb atom separation on the electronic structure of disordered alloy supercells. We begin with a $\text{Ge}_{63}\text{Pb}_1$ supercell and substitute a second Pb atom to form four distinct $\text{Ge}_{62}\text{Pb}_2$ ($x = 3.125\%$) supercells in which the two Pb atoms are located at fourth-, third-, second- and first-nearest lattice sites. In this manner, we begin with a $\text{Ge}_{62}\text{Pb}_2$ supercell in which the Pb atoms are fourth-nearest neighbours, and form a nearest-neighbour Pb-Pb pair by bringing the two Pb atoms closer together. In each of these four cases we calculate the electronic structure and quantify the dependence of the fundamental band gap E_g , and its pressure coefficient $\frac{dE_g}{dP}$, on the relative position of the two Pb atoms in the supercell. As in chapter 4 for Sn, the incorporation of > 1 substitutional Pb atoms breaks the cubic symmetry of the underlying diamond lattice, which was preserved in the ordered supercell calculations of Sec. 5.3.1. As a result of this reduction in symmetry the fourfold (twofold and Kramers) degeneracy of the zone-centre VB edge states is lifted, giving rise to two distinct sets of Kramers degenerate states. The precise value of the VB edge splitting in a disordered supercell is in general a non-monotonic function of Pb composition x , but instead depends on the precise short-range disorder present in the given alloy supercell. In this section, as well as in Sec. 5.3.3 below, we therefore calculate band gaps in disordered supercells with respect to the average energy of the split VB edge states.

The results of our calculations – using the mBJ XC functional – for this set of disordered $\text{Ge}_{62}\text{Pb}_2$ supercells are summarised in Fig. 5.3, where Figs. 5.3(a), 5.3(b), 5.3(c) and 5.3(d)

respectively show the calculated CB structure in the case of having fourth-, third-, second- and first-nearest neighbour Pb atoms. Figures 5.3(e) and 5.3(f) respectively show the dependence of the calculated values of E_g and $\frac{dE_g}{dP}$ on the relative position of the two Pb atoms. The band structures shown in Figs. 5.3(a), 5.3(b), 5.3(c) and 5.3(d) display, overall, strong qualitative similarity. As in the ordered supercells described above, the (Kramers degenerate) lowest energy CB state in each supercell possesses primarily *s*-like orbital character at Pb lattice sites, while the next three (Kramers degenerate) CB states possess primarily *p*-like orbital character at Pb lattice sites. While in an ordered alloy supercell these *p*-like Ge L_{6c} -derived states form a degenerate triplet, their degeneracy is lifted in the disordered supercells considered here due to the loss of the underlying cubic symmetry of the lattice. However, as we describe below, despite qualitative similarities in the calculated band structures, Pb clustering produces significant quantitative differences in the calculated electronic properties in supercells having fixed Pb composition x .

Beginning with a $\text{Ge}_{62}\text{Pb}_2$ supercell in which the two Pb atoms are fourth-nearest neighbours we calculate a fundamental band gap $E_g = 0.472$ eV, which is reduced by 252 meV compared to the fundamental band gap of Ge, and by 124 meV compared to that of the ordered $\text{Ge}_{63}\text{Pb}_1$ supercell considered in section 5.3.1. Correspondingly, we calculate $\Delta_{\text{SO}} = 0.377$ eV for this $\text{Ge}_{62}\text{Pb}_2$ supercell, which is increased by 103 meV compared to that in Ge, and by 43 meV compared to that in $\text{Ge}_{63}\text{Pb}_1$. In line with the ordered supercell calculations of Sec. 5.3.1, these results confirm that Pb incorporation in Ge leads to a strong decrease in E_g and increase in Δ_{SO} with increasing x . For the case of third-nearest neighbour Pb atoms we calculate $E_g = 0.435$ eV ($\Delta_{\text{SO}} = 0.396$ eV), which is 37 meV lower (19 meV higher) than that calculated in the case of fourth-nearest neighbour Pb atoms. Ultimately, in the presence of a nearest-neighbour Pb-Pb pair we calculate $E_g = 0.406$ eV, which is reduced by 318 meV compared to the fundamental band gap of Ge, and by 66 meV compared to the case of fourth-nearest neighbour Pb atoms. Similarly, we calculate $\Delta_{\text{SO}} = 0.425$ eV for the supercell containing a Pb-Pb nearest-neighbour pair, which is increased by 151 meV compared to that in Ge, and by 48 meV compared to the case of fourth-nearest neighbour Pb atoms. We emphasise that the calculated decrease of E_g – shown in Fig. 5.3(e) – and increase of Δ_{SO} (not shown) as the two Pb atoms are brought closer together is not a monotonic function of the Pb-Pb interatomic distance, but depends on the specific relative position of the two Pb atoms. Since these four disordered supercells have equal Pb composition $x = 3.125\%$, this calculated ≈ 70 meV variation in E_g – representing $\approx 15\%$ of the total band gap – indicates the significant impact that Pb-Pb clustering may have on the electronic properties of $\text{Ge}_{1-x}\text{Pb}_x$ alloys.

Figure 5.3(f) shows the calculated pressure coefficients $\frac{dE_g}{dP}$, associated with the fundamental supercell band gap E_g , as a function of Pb-Pb separation for the same series of $\text{Ge}_{62}\text{Pb}_2$ supercells. In line with the ordered supercell calculations of Sec. 5.3.1, the calculated values of $\frac{dE_g}{dP}$ are intermediate between the values 4.07 and 13.23 meV kbar $^{-1}$ associated with the L_{6c} - Γ_{8v}

and Γ_{7c} - Γ_{8v} band gaps of Ge (cf. Table 5.2). Again, this reveals the hybridised nature of the alloy CB edge states in these supercells, which are primarily derived from a linear combination of Ge L_{6c} states having strong s -like orbital character at the Pb lattice sites, but which contain an admixture of Ge Γ_{7c} character. In all four cases – having fourth-, third-, second- and first-nearest neighbour Pb atoms – the calculated value of $\frac{dE_g}{dP}$ remains closer to that associated with the Ge fundamental (indirect) band gap, suggesting that the supercell band gap remains primarily indirect in nature, but with some direct character, at $x = 3.125\%$. This observation is in contrast to previous theoretical analysis of $\text{Ge}_{1-x}\text{Pb}_x$ alloys, which have alternatively predicted a band gap having purely indirect [175] or direct [45] character at this composition. We also note that the precise value of $\frac{dE_g}{dP}$ varies non-monotonically with Pb-Pb separation, revealing that the details of the Pb-induced band mixing are impacted by the specific short-range disorder present in a given alloy supercell. This demonstrates more generally that the character of the CB edge states, and hence the nature of the band gap, in real (disordered) $\text{Ge}_{1-x}\text{Pb}_x$ alloys, is sensitive to the presence of short-range alloy disorder and Pb clustering.

Overall, these results demonstrate that the calculated values of E_g and $\frac{dE_g}{dP}$ – the latter reflecting the hybridised character of the alloy CB edge states – in $\text{Ge}_{1-x}\text{Pb}_x$ at fixed Pb composition x display significant dependence on the precise short-range alloy disorder present in a given alloy supercell. We note however that due to the small number of atoms ($N = 64$) in these supercells, the importance of such short-range disorder effects may be overstated here in comparison to the effects that would likely be noted in larger scale alloy supercell calculations. This issue is discussed in more detail in Sec. 5.3.3 below. While our analysis in Sec. 5.3.1 identified the presence of Pb-induced band mixing in $\text{Ge}_{1-x}\text{Pb}_x$, our calculations here indicate the sensitivity of the $\text{Ge}_{1-x}\text{Pb}_x$ electronic structure to the presence of short-range alloy disorder (particularly in the form of clustering of substitutional Pb atoms). From a theoretical perspective, our results therefore emphasise the breakdown of the VCA in $\text{Ge}_{1-x}\text{Pb}_x$ alloys, which neglects effects related to band mixing and alloy disorder. We therefore conclude that atomistic calculations which explicitly account for the differences in size and chemical properties between Ge and Pb are required to provide quantitative insight into the properties of real $\text{Ge}_{1-x}\text{Pb}_x$ alloys.

5.3.3 Disordered alloys: electronic structure evolution in germanium-lead special quasi-random structures

Having established the importance of short-range Pb-related structural disorder in determining the details of the alloy electronic structure, we turn our attention now to the evolution of the electronic structure with x in realistic, disordered $\text{Ge}_{1-x}\text{Pb}_x$ SQSs. The special quasi random structures generated here are the same in terms of atomic positioning as those already detailed for the 128 atom SQS electronic structure calculations detailed in chapter 4. As such the

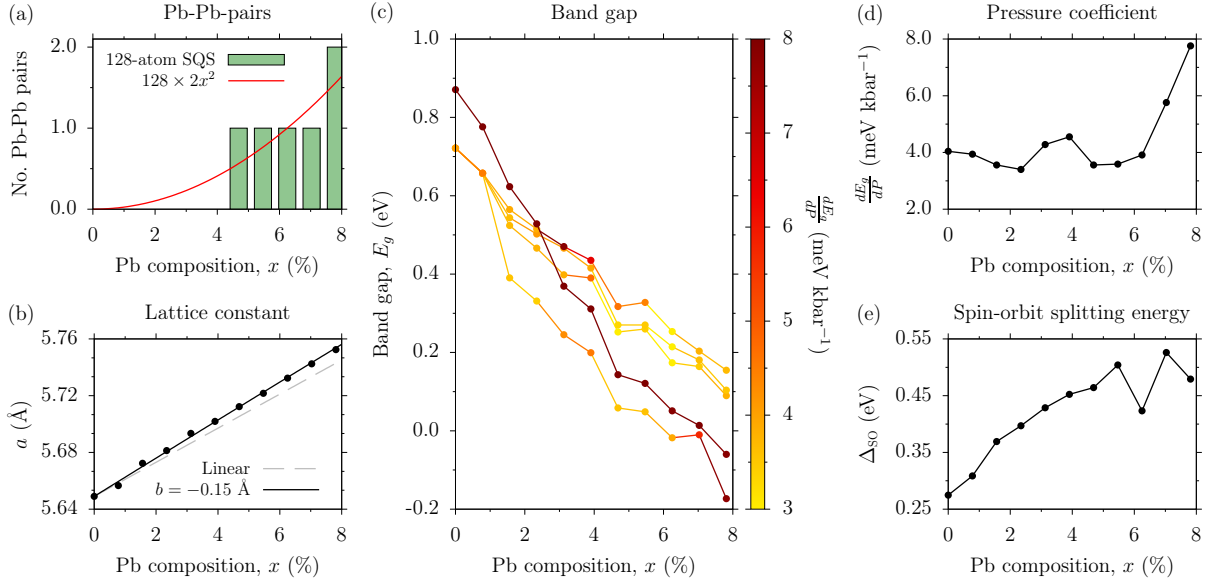


FIGURE 5.4: (a) Expected (solid red line) and actual (solid green bars) occurrence of nearest-neighbour Pb-Pb pairs in the 128-atom ($4 \times 4 \times 4$ FCC) SQSs used to analyse the electronic structure evolution in disordered $\text{Ge}_{1-x}\text{Pb}_x$ alloys. (b) Variation of the relaxed lattice constant a with Pb composition x (closed circles) for the SQSs of (a). The dashed grey line shows a calculated by interpolating linearly between the lattice constants of Ge and diamond-structured Pb (cf. Table 5.1). The solid black line shows the best fit to the calculated lattice constants, having bowing parameter $b = -0.15 \text{ \AA}$. (c) Variation with x of the band gaps E_g , calculated between the VB edge and the five lowest energy CB states (closed circles). The colour of the data points are weighted according to the pressure coefficient $\frac{dE_g}{dP}$ associated with the corresponding band gap E_g . (d) Variation of $\frac{dE_g}{dP}$ with x for the fundamental band gap of (c). (e) Variation of the VB spin-orbit splitting energy Δ_{SO} with x .

expected (solid red line) and actual (solid green bars) number of occurrence of clusters of Pb–Pb for each % Pb composition, shown in Figure 5.4(a), are in all cases equal, rounding to the nearest whole number. Again we note that the probability of occurrence of a larger cluster containing three neighbouring Pb atoms is $\propto x^3$, which remains $\lesssim 10^{-3}$ in the composition range considered. Hence we expect, and find, that no Pb clusters containing more than two neighbouring Pb atoms occur in the SQSs employed in our analysis here. On this basis, we conclude that the 128-atom SQSs considered here have appropriate distributions of Pb atoms to analyse the evolution of the alloy properties with x .

The closed circles in Fig. 5.4(b) show the variation of the relaxed lattice constant a with x for the series of SQSs investigated. Comparing the calculated values of a to the increase expected based on Végard’s law (dashed grey line), we observe that the lattice constants calculated for SQSs containing > 1 Pb atom exceed those expected based on a linear interpolation of the Ge and d-Pb lattice constants. This suggests a negative bowing coefficient b for the lattice constant of disordered $\text{Ge}_{1-x}\text{Pb}_x$. Fitting to the calculated lattice constants – depicted by the solid black line in Fig. 5.4(b) – yields a best-fit bowing coefficient $b = -0.15 \text{ \AA}$. We note that this is in contrast to the results of our calculations in Sec. 5.3.1, where relaxation of ordered alloy supercells predicted a positive value of b in the range $0.1 - 0.4 \text{ \AA}$, and likely reflects

that the presence of Pb-Pb pairs and disorder leads to larger local expansion of the crystal lattice. Given that (i) real $\text{Ge}_{1-x}\text{Pb}_x$ alloy samples will inevitably contain varying degrees of atomic-scale disorder, and (ii) SQSs are generally found to accurately predict the evolution with composition of the structural and elastic properties of randomly disordered alloys, [173] we expect that $b = -0.15 \text{ \AA}$ represents a realistic prediction of the lattice constant bowing in $\text{Ge}_{1-x}\text{Pb}_x$ alloys.

Turning our attention to the electronic structure evolution, Fig. 5.4(c) shows the calculated variation with x of the band gaps between the alloy VB edge and the five lowest energy CB states. Here, we show the band gaps calculated for the five (Kramers degenerate) lowest energy CB states in each SQS: for $x = 0$ the four lowest energy states are the L_{6c} CB minimum states of Ge, while the fifth is the Γ_{7c} zone-centre CB edge state of Ge. As in Sec. 5.3.3, due to the loss of cubic symmetry and associated lifting of the degeneracy of the VB edge states, we calculate band gaps with respect to the average energy of the two highest energy sets of Kramers degenerate VBs. At first glance, Fig. 5.4(c) seems to suggest that the indirect-to-direct-gap transition occurs for $x \approx 2\%$, around which composition we observe four (Kramers degenerate) CB states lying within $\approx 100 \text{ meV}$ of one another, with one state lying $\approx 150 \text{ meV}$ below these four higher energy states. However, we have weighted the colour of each of the data points in Fig. 5.4(c) according to the corresponding calculated pressure coefficient $\frac{dE_g}{dP}$: starting from yellow for $\frac{dE_g}{dP} = 3 \text{ meV kbar}^{-1}$ (close to that of the Ge L_{6c} - Γ_{8v} fundamental band gap), and shifting towards red as $\frac{dE_g}{dP}$ (i.e. direct character of the band gap) increases. Considering then $\frac{dE_g}{dP}$ associated with each band gap, we find that the four lowest energy CB states retain predominantly Ge L_{6c} character for $x \approx 2\%$, at which composition the fifth CB state has the greatest Ge Γ_{7c} character. As such, the alloy band gap remains primarily indirect in nature for $x \approx 2\%$.

The general trends observed in Fig. 5.4(c) are largely consistent with those observed for ordered supercells in Sec. 5.3.1, where we found that the CB states originating from the L_{6c} states of Ge split into (Kramers degenerate) singlet and triplet states, respectively possessing primarily s - and p -like orbital character at Pb lattice sites, with the singlet states lying lower in energy. Due to the loss of cubic symmetry in the disordered supercells considered here we observe lifting of the degeneracy of the p -like Ge L_{6c} -derived triplet states, which otherwise remain closely spaced in energy with increasing Pb composition x . Additionally, we observe that the alloy CB states originating from the Γ_{7c} states of Ge decrease in energy more rapidly with increasing x than those originating from the Ge L_{6c} states. As x increases the calculated CB states originating from the Γ_{7c} states of Ge firstly pass through the p -like Ge L_{6c} -derived CB states, for $x \approx 2.5\%$. As this occurs we note weak hybridisation between these two sets of states, evidenced by the abrupt rise and subsequent fall in the values of $\frac{dE_g}{dP}$ associated with the p -like triplet CB states. As x increases further, we note the emergence of a direct band gap for $x \approx 7\%$. This is evidenced by a sharp increase in $\frac{dE_g}{dP}$ associated with the fundamental band

gap as the energy of the Ge Γ_{7c} -derived CB states approaches that of the s -like Ge L_{6c} -derived singlet states. This sharp increase in $\frac{dE_g}{dP}$ describes the transition to the fundamental band gap having primarily, but not purely, direct (Ge Γ_{7c}) character. We emphasise that this transfer of Ge Γ_{7c} character to the Ge L_{6c} -derived states again occurs only when the two sets of states become close in energy, suggesting relatively weak Pb-induced hybridisation of Ge L_{6c} and Γ_{7c} host matrix states.

The alloy band gap becomes primarily direct in character by $x = 7.81\%$ in the current calculations – i.e. for the $\text{Ge}_{118}\text{Pb}_{10}$ SQS – at which composition the band gap simultaneously closes, describing a semiconducting to semimetallic transition that coincides with the indirect- to direct-gap transition. The character of the indirect- to direct-gap transition in $\text{Ge}_{1-x}\text{Pb}_x$ is emphasised in Fig. 5.4(d), which shows the variation with x of $\frac{dE_g}{dP}$ associated with the fundamental band gap of Fig. 5.4(c). Here, as x increases $\frac{dE_g}{dP}$ initially remains close to that associated with the fundamental (indirect) L_{6c} - Γ_{8v} band gap of Ge (cf. Table 5.2). However, as x increases further we calculate an abrupt increase in $\frac{dE_g}{dP}$, towards that of the direct Γ_{7c} - Γ_{8v} band gap of Ge (cf. Table 5.2), reflecting the onset of an alloy band gap having primarily direct character over a narrow range of Pb compositions centred about $x \approx 7\%$.

While the calculated values of $\frac{dE_g}{dP}$ in Fig. 5.4(d) illustrate the indirect- to direct-gap transition in $\text{Ge}_{1-x}\text{Pb}_x$, we note that these values are not suitable for direct comparison to experimental measurements, and likewise that Fig. 5.4(c) may overestimate the Pb composition at which the indirect- to direct-gap transition may occur. In a real alloy, all states that can (by symmetry) mix will mix: this behaviour is not captured quantitatively in DFT supercell calculations due to their limitation to structures containing $\lesssim 10^2$ atoms. In such small supercells only a limited number of Ge host matrix states fold to $\mathbf{K} = 0$ close in energy to the CB edge. Since only states which fold to the same supercell wave vector \mathbf{K} can hybridise in supercell calculations, supercell size then limits the number of states that can undergo mixing in a given alloy supercell. In practice, this limits the growth of $\frac{dE_g}{dP}$ with increasing x . Additionally, calculations for SQSs containing $\lesssim 10^2$ atoms suffer from finite-size effects, insofar as the SQSs possess a higher degree of ordering than in a real disordered alloy. This stems from the use of Born-von Karman boundary conditions, which creates artificial long-range ordering on a length scale defined by the supercell lattice constant A (with $A \sim 1$ nm in the $4 \times 4 \times 4$ FCC SQSs considered here). In our calculations this artificial long-range ordering allows the formation of Ge L_{6c} -derived alloy CB states having predominantly s -like orbital character on each of the Pb lattice sites, hence enabling the large splitting of ≈ 150 meV observed between the s -like singlet and p -like triplet Ge L_{6c} -derived states in Fig. 5.4(c). Such a large splitting would not be expected to occur in a real $\text{Ge}_{1-x}\text{Pb}_x$ alloy. Rather, the Ge L_{6c} -related band edge will be inhomogeneously broadened in energy due to the loss of both short- and long-range order. If we assume that the Ge L_{6c} -derived CB states in Fig. 5.4(c) are inhomogeneously broadened about their average energy, then the Ge Γ_{7c} -derived CB states would cross this average energy

associated with the Ge L_{6c} -derived CB states for $x \approx 3 - 4\%$. This then places an estimated lower limit from our calculations on the Pb composition x at which $\text{Ge}_{1-x}\text{Pb}_x$ transitions from indirect- to direct-gap. This uncertainty in transition composition could be reduced by using larger alloy supercells containing $\gtrsim 10^3$ atoms, as we have demonstrated for $\text{Ge}_{1-x}\text{Sn}_x$ alloys via the use of a highly scalable semi-empirical tight-binding model. However, the trend predicted by Fig. 5.4(d) – that the composition range in which the indirect- to direct-gap transition occurs in $\text{Ge}_{1-x}\text{Pb}_x$ can be identified via an accompanying sharp increase in $\frac{dE_g}{dP}$ – can be expected to emerge in real alloys, and hence in experimental measurements.

Finally, Fig. 5.4(e) shows the calculated variation of Δ_{SO} with x . As for the calculation of E_g above, Δ_{SO} is calculated with respect to the average VB edge energy. Still, we note deviations from a smooth monotonic increase of Δ_{SO} with x , likely reflecting the non-monotonic variation with x of the VB edge splitting. Generally, we find that Δ_{SO} increases strongly with increasing x , although slightly less strongly than the corresponding increase calculated in Sec. 5.3.1 for ordered alloy supercells. For example, the calculated value $\Delta_{\text{SO}} = 0.571$ eV for an ordered $\text{Ge}_{15}\text{Pb}_1$ ($x = 6.25\%$) supercell is larger by 45 meV than the value of 0.526 eV calculated for the $\text{Ge}_{119}\text{Pb}_9$ ($x = 7.03\%$) SQS, which is the largest value calculated for the series of SQSs considered here.

Nonetheless, the overall increase of Δ_{SO} with x is sufficiently strong that we find $\Delta_{\text{SO}} > E_g$ for Pb compositions as low as $x \approx 2.3\%$. We note that this behaviour is qualitatively similar to that in the III-V dilute bismide alloy $(\text{In})\text{GaAs}_{1-x}\text{Bi}_x$, where Bi incorporation results in a simultaneous strong decrease of E_g and increase of Δ_{SO} with increasing x , leading to a band structure in which $\Delta_{\text{SO}} > E_g$. This unusual band structure condition is appealing from a practical perspective since it offers the potential to suppress (i) hot-hole producing non-radiative Auger recombination processes, and (ii) inter-valence band absorption involving the spin-split-off band, both of which play a strong role in limiting the efficiency of long-wavelength semiconductor lasers and light-emitting diodes [184].

5.3.4 Comparison to electronic structure evolution in GeSn

Equivalent analysis to that of Figs. 5.4(a)–(e), is detailed in chapter 4 for $\text{Ge}_{1-x}\text{Sn}_x$ alloys. Comparing the results of these two alloys over equivalent series of 128-atom SQSs, reveals quantitative differences in the evolution of the alloy band structures from indirect- to direct-gap.

As can be seen in Figure 5.5 (a) incorporation of Pb into the $\text{Ge}_{1-x}\text{Pb}_x$ alloy causes a strong reduction of the alloy fundamental band gap (≈ 100 meV per % Pb added), notably larger than that of equivalent addition of Sn to $\text{Ge}_{1-x}\text{Sn}_x$, (≈ 35 meV per % Sn added). Pb incorporation is also seen to have a notable impact on spin-orbit splitting energy as seen in Figure 5.5 (c)

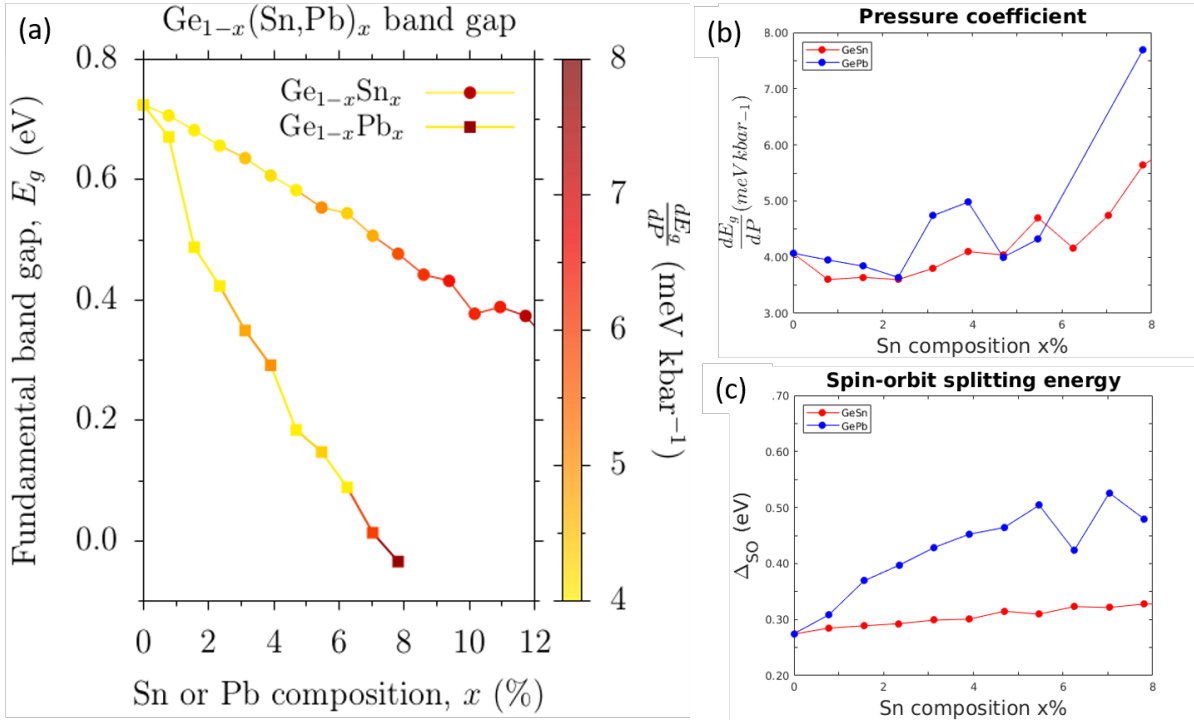


FIGURE 5.5: (a) Variation with x of the band gaps E_g of $\text{Ge}_{1-x}(\text{Sn,Pb})_x$ alloys, calculated between the VB edge and the lowest energy CB state. The coloured circles (squares) denote the band gap with varying x in $\text{Ge}_{1-x}\text{Sn}_x$ ($\text{Ge}_{1-x}\text{Pb}_x$) alloys. The colour of the data points are weighted according to the pressure coefficient $\frac{dE_g}{dP}$ associated with the band gap E_g at the corresponding composition x . (b) Variation of $\frac{dE_g}{dP}$ with x for the fundamental band gap of $\text{Ge}_{1-x}(\text{Sn,Pb})_x$ alloys from (a). (c) Variation of the VB spin-orbit splitting energy Δ_{SO} with x .

where the spin orbit splitting energy in $\text{Ge}_{1-x}\text{Pb}_x$ is seen to increase more rapidly than in equivalent $\text{Ge}_{1-x}\text{Sn}_x$ alloys.

Figure 5.5 (b) shows the evolution of the pressure coefficient of the conduction band edge of $\text{Ge}_{1-x}(\text{Sn/Pb})_x$ with increased % Sn/Pb. The calculated band mixing in $\text{Ge}_{1-x}\text{Pb}_x$ alloys is weaker than in $\text{Ge}_{1-x}\text{Sn}_x$ evidenced by the more dramatic increase in pressure coefficient noted in $\text{Ge}_{1-x}\text{Pb}_x$ alloys at $\approx 4\%$ Pb content. For $\text{Ge}_{1-x}\text{Sn}_x$ we calculate that $\frac{dE_g}{dP}$ increases gradually with increasing x . This reflects the stronger role played by band mixing in the $\text{Ge}_{1-x}\text{Sn}_x$ supercells: a hybridised alloy band gap having primarily direct character evolves continuously over a comparatively wide composition range, driven by Sn-induced band mixing which transfers Ge Γ_{7c} character to the alloy CB edge.

5.4 Chapter Summary

In summary, we have presented a theoretical analysis of electronic structure evolution and the indirect- to direct-gap transition in the group-IV alloy $\text{Ge}_{1-x}\text{Pb}_x$. We established DFT calculations of the structural and electronic properties of the constituent materials (i) diamond-structured semiconducting Ge, (ii) diamond-structured metallic Pb, and (iii) the fictitious semimetallic IV-IV compound zb-GePb, using both the HSEsol and mBJ XC functionals. Comparison of the calculated electronic structure of ordered alloy supercells (i) elucidated the mechanism driving the indirect- to direct-gap transition with increasing Pb composition x , and (ii) established the suitability of the mBJ XC functional to analyse $\text{Ge}_{1-x}\text{Pb}_x$ alloys. The mBJ XC functional was therefore used to analyse the electronic structure evolution in disordered alloy supercells using a SQS approach.

A $\text{Ge}_{63}\text{Pb}_1$ ($x = 1.56\%$) or $\text{Ge}_{15}\text{Pb}_1$ ($x = 6.25\%$) supercell partially lifts the degeneracy of the Ge L_{6c} CB edge states, giving rise to (i) a singlet possessing s -like symmetry at the Pb lattice site, and (ii) a triplet possessing p -like symmetry at the Pb lattice site. The emergence of an s -like singlet state at the CB edge could be interpreted as evidence of a direct band gap for Pb compositions as low as $x \approx 1\%$. However, the calculated pressure coefficient associated with the $\text{Ge}_{63}\text{Pb}_1$ supercell band gap demonstrated that the CB edge singlet state possesses only a small admixture of direct (Ge Γ_{7c}) character and retains primarily indirect (Ge L_{6c}) character at $x = 1.56\%$. For a $\text{Ge}_{15}\text{Pb}_1$ ($x = 6.25\%$) supercell, the band gap pressure coefficient was calculated to be close to that of the Ge direct Γ_{7c} - Γ_{8v} band gap, indicating the emergence of a direct band gap in the alloy with increasing Pb composition x , characterised by the transfer of Ge Γ_{7c} character to the alloy CB edge. This supported the requirement for further detailed analysis of the electronic structure evolution in disordered alloy supercells, to quantify the nature of the indirect- to direct-gap transition and therefore identify the Pb composition x at which $\text{Ge}_{1-x}\text{Pb}_x$ becomes a direct-gap semiconductor.

To quantify the impact of Pb-related alloy disorder we tracked the evolution of the alloy CB edge in a $\text{Ge}_{62}\text{Pb}_2$ supercell as the separation between the Pb atoms was reduced from fourth- to first-nearest neighbours. Substituting two Pb atoms at successively closer lattice sites, we found strong dependence of the alloy band gap on the distance between the two Pb atoms. Having established the importance of the alloy microstructure in determining the details of the electronic properties, we then analysed the emergence of a direct band gap with increasing x for the realistic case of a randomly disordered alloy.

The calculated electronic structure evolution for disordered 128-atom $\text{Ge}_{128-M}\text{Pb}_M$ SQSs again showed a (Kramers degenerate) singlet state at the CB edge, even for the lowest Pb composition considered ($x = 0.78\%$). However, the calculated pressure coefficients associated with the band gaps between the VB edge and the five lowest energy (Kramers degenerate) CB states

showed that the CB edge retained primarily Ge L_{6c} character until $x \approx 6 - 7\%$, at which composition the lowest energy CB state acquired predominantly direct (Ge Γ_{7c}) character. The SQS calculations therefore indicate an indirect- to direct-gap transition in $\text{Ge}_{1-x}\text{Pb}_x$ alloys for $x \approx 6 - 7\%$, near which composition the CB edge also passes through the VB edge, to give a zero-gap semimetallic alloy. We note however that finite-size effects in the SQSs considered may lead to an overestimate of the composition at which $\text{Ge}_{1-x}\text{Pb}_x$ becomes direct-gap. Our SQS calculations show large splitting of the four Ge L_{6c} -derived states, with the singlet state having primarily s -like orbital character at Pb atoms lying ≈ 150 meV below three states having primarily p -like orbital character at Pb atoms. We expect that such a large splitting would not be observed in calculations for larger supercells, or in real alloys, and arises in our calculations due to the absence of long-range alloy disorder in the relatively small supercells to which DFT calculations are limited. Rather, we anticipate that the Ge L_{6c} character associated with alloy CB states will experience inhomogeneous broadening about their mean energy in real alloys. The CB state having greatest Ge Γ_{7c} character passes through the weighted average energy of the four L_{6c} -derived states in our SQS calculations for $x \approx 3 - 4\%$. This weighted average may then provide a more realistic estimate of the composition range in which $\text{Ge}_{1-x}\text{Pb}_x$ starts to become a direct-gap semiconductor, at which composition the calculated alloy band gap is in the range 0.3 – 0.4 eV.

Overall, we predict the emergence of a direct band gap in response to substitutional Pb incorporation in Ge, suggesting that binary $\text{Ge}_{1-x}\text{Pb}_x$ alloys are potentially of interest for applications in CMOS-compatible active photonic devices operating at mid-infrared wavelengths. However, the potential for applications of $\text{Ge}_{1-x}\text{Pb}_x$ alloys in such devices may in practice be limited by the presence of a low fundamental band gap. Further investigations are now required to confirm the emergence of a direct band gap in response to Pb incorporation, as well as to quantify the implications of the band mixing and short-range alloy disorder effects identified by our analysis for technologically relevant material properties including optical generation and recombination rates, carrier mobilities, and band-to-band tunneling currents.

Chapter 6

Final Summation, conclusions, and outlook

The work presented in this thesis aims from a theoretical perspective, and with experimental support, to investigate the material, optical and electronic properties of germanium-based group-IV alloys and the implications they hold for the future of CMOS compatible group-IV optoelectronic devices. We focus in particular on two Ge-based group-IV alloys which have potential applications in future Si-compatible CMOS devices, GeSn alloys (which are the subject of chapter 3 and chapter 4) and GePb alloys (the properties of which are investigated in chapter 5). This final chapter summarises the key findings and main conclusions of the investigations into each of these materials and provides guidance for future work in each area.

6.1 Group-IV Optoelectronics

The realization of the full potential of CMOS technologies requires active components which are built from Si compatible materials, so as to be easily integratable with existing chipsets. Active photonic components, like LEDs, are intrinsically difficult to fashion from Si due to the fundamentally indirect band gap of the material rendering it an inefficient emitter or absorber of light. Aside from silicon, on which the vast majority of existing CMOS device technology is based, germanium and other group-IV elements are also already in wide usage within existing CMOS device workflows. Ge in particular is of note as it has been predicted to offer the benefit of significantly higher hole mobility than Si, and because the direct band gap in Ge lies only 136meV above the indirect conduction band minima at L. As a result it is possible to engineer the band gap of Ge so as to bring about a direct gap in a material that is compatible with existing CMOS technologies.

The work in this thesis focuses on the alloying of Ge with Sn or Pb to bring about a direct bandgap $\text{Ge}_{1-x}(\text{Sn/Pb})_x$ alloy. Incorporation of Sn or Pb into the Ge lattice reduces the conduction band edge at the direct Γ point at a faster rate than it reduces the indirect conduction band edges at other critical points like L and X. With sufficient Sn or Pb content the conduction band edge at Γ is shifted below L to bring about a direct band gap in the alloy. To date however there remain discrepancies in the theoretical and experimental literature values for the composition of Sn required to bring about a direct band gap in GeSn alloys, while the band structure and properties of GePb alloys have remained largely unexplored in literature.

6.2 Optoelectronic properties of GeSn alloys

Chapter 3 detailed a combined theoretical and experimental investigation of the evolution of the band gap in GeSn alloys carried out in collaboration with the University of Surrey. This investigation primarily focused on the transition from an indirect to a direct band gap material as the % Sn composition of the $\text{Ge}_{1-x}\text{Sn}_x$ alloy was increased from 0-10%. The experimental side of this investigation consisted of a series of photovoltage measurements carried out on hydrostatically strained $\text{Ge}_{1-x}\text{Sn}_x$ photodiodes of 6, 8 and 10% Sn content respectively. From these measurements the hydrostatic pressure coefficient of the conduction band edge of each sample was determined. In contrast to existing literature the results of these measurements, particularly for the photodiode with $\approx 6\%$ Sn indicated that the band edge pressure coefficient was neither purely L-like (indirect) or Γ -like (direct) in nature but rather an admixture of band gap character from these states. The theoretical investigation of the band structure detailed in this chapter, which comprised of a series of DFT electronic structure and hydrostatic pressure calculations on supercells of $\text{Ge}_{1-x}\text{Sn}_x$ with varying Sn composition, supported this experimental finding with the 16 and 64 atom supercells of 6% Sn both showing a band gap with band character which was intermediate between Γ and L.

Overall the results in this chapter indicate that there is a continuous evolution from indirect to direct band gap in GeSn alloys which is driven by the band mixing effects which cause a monotonic increase in Γ character in the conduction band gap edge, as the band gap narrows as a function of Sn concentration. These band mixing effects could have important implications for any future optoelectronic devices arising from GeSn alloys including potentially improving optical properties at lower Sn concentrations than would otherwise be expected.

Chapter 4 of this thesis expands on the scope of the theoretical investigation of GeSn alloys from chapter 3. In this chapter an extensive theoretical study of GeSn alloys and their material, optical and electronic properties was performed using DFT methods in the VASP framework. This study was primarily undertaken using Heyd-Scuseria-Ernzerhof hybrid functional and modified Becke-Johnson DFT methods but also included the introduction of a valence force

field (VFF) and tight-binding (TB), parameterised by collaborators. This model can be used to expand the investigation to a series of larger supercells than would be possible with the more accurate but computationally expensive DFT. Using HSE and mBJ DFT a series of ordered and disordered supercells which ranged in size from 16 to 128 atoms were investigated, and the evolution of the supercell band structure with increasing % Sn content was probed.

As HSEsol DFT calculations are found to be in good quantitative agreement with experimental measurements, the results of these calculations were taken as a reference to quantify the accuracy of the LDA + mBJ and VFF + TB models. The trends in the $\text{Ge}_{1-x}\text{Sn}_x$ alloy lattice constant, relaxed atomic positions, band gap and valence band spin-orbit splitting energy calculated using the LDA + mBJ and VFF + TB models were all found to be in good qualitative and quantitative agreement with the results of full HSEsol calculations. Alloy supercell band structure calculations carried out using all three models showed strong Sn-induced band mixing and alloy disorder effects in the $\text{Ge}_{1-x}\text{Sn}_x$ CB structure. These results emphasise and reinforce the suggestion from Chapter 3 that the evolution of a direct band gap in $\text{Ge}_{1-x}\text{Sn}_x$ occurs continuously with increasing Sn composition. The alloy band gap pressure coefficient was calculated using each of the three approaches as it offers an experimentally measurable means by which to quantify hybridisation of the conduction band edge. Again, the LDA + mBJ and VFF + TB calculations were found to capture both qualitatively and quantitatively the trends observed in full HSEsol calculations. The results of the benchmark calculations lead to the following general conclusion. The LDA + mBJ model offers an accurate description of $\text{Ge}_{1-x}\text{Sn}_x$ alloys at reduced computational expense compared to HSEsol calculations, providing access to larger systems within a first principles framework.

With the suitability of the mBJ XC functional established for the investigation of GeSn alloys, the impact of Sn-related alloy disorder in disordered alloy supercells was then investigated by tracking the evolution of the alloy CB edge in $\text{Ge}_{14}\text{Sn}_2$ (12.5% Sn content) and $\text{Ge}_{62}\text{Sn}_2$ (3.125% Sn content) supercells as the separation between the Sn atoms was reduced from fourth- to first-nearest neighbours. The alloy band gap was found to have a strong dependence on the distance between the two Sn atoms indicating that atomic-scale alloy disorder strongly impacts quantitative analysis of the alloy electronic structure.

The evolution of the band gap from indirect to direct was then analysed for a randomly disordered alloy using 128-atom $\text{Ge}_{128-x}\text{Sn}_x$ SQSs. Calculation of the pressure coefficients associated with the band gaps between the VB edge and the five lowest energy CB states show that the CB edge of GeSn retains primarily Ge L_{6c} character until $x \approx 7\%$, at which composition the lowest energy CB state acquired predominantly direct (Ge Γ_{7c}) character. At this composition of $\approx 7\%$ Sn content the band gap has a value of 0.499eV, suitable for applications in semiconductor devices.

Overall the results of this chapter indicate the emergence of a direct band gap in response to substitutional incorporation of $x \approx 7\%$ Sn in $\text{Ge}_{1-x}\text{Sn}_x$ alloys, and that band mixing and disorder effects in GeSn alloys strongly impact the evolution of the conduction band. As a result electronic structure calculations for $\text{Ge}_{1-x}\text{Sn}_x$ alloys must explicitly consider band mixing and disorder effects to allow for accurate analysis of the impact of Sn incorporation on key material parameters, including optical transition strengths, electron mobility and band-to-band tunneling rates. Given the expected importance of these effects in determining technologically relevant material properties, the development of appropriate theoretical models represents an important step to enable predictive theoretical analysis of proposed $\text{Ge}_{1-x}\text{Sn}_x$ -based photonic, electronic and photovoltaic devices. The theoretical models we have presented allow for the treatment of larger systems than those accessible to hybrid functional DFT with minimal loss of accuracy, providing a basis for direct atomistic calculations of the electronic, optical and transport properties of disordered $\text{Ge}_{1-x}\text{Sn}_x$ alloys and realistically-sized nanostructures.

6.3 Outlook, ongoing work and future work

Progress towards the realisation of efficient active photonic components from GeSn alloys has already begun with recent effort culminating in the demonstration of lasing in group-IV GeSn structures. [46, 185–189] Further development and improvement of such active group-IV photonic components will require continued study to better understand the impact of band mixing and disorder effects will have on GeSn alloys, at a device scale level. Using the valence force field and tight binding models parameterised and benchmarked in chapter 4 from HSE-DFT calculations will allow for the investigation of supercells of the order of $10^5 - 10^6$ atoms. At this scale it should be possible to research the impacts of band mixing and disorder on a cell at a scale where long range ordering of the supercell will not affect the calculation, allowing for better simulation of a real alloy case.

Another obvious avenue for further research arising from the work presented in this thesis is the extension of the mBJ-DFT approach used in chapters 3 and 4 to investigate the band structure of ternary SiGeSn alloys. Understanding the mechanism by which the band structure of $\text{Si}_y\text{Ge}_{1-x-y}\text{Sn}_x$ evolves with x and y is an important step towards the integration of active GeSn photonic devices onto existing Si based CMOS technologies. DFT and tight binding calculations should be capable of elucidating how the band structure evolves with varying Si and Sn composition for application e.g. in photovoltaics. In this manner DFT calculations could provide useful guideline for the fabrication of devices and their integration with existing Si and photovoltaic technologies.

6.4 Optoelectronic properties of GePb alloys

While $\text{Ge}_{1-x}\text{Sn}_x$ alloys have attracted significant theoretical interest, there have been few reports to date regarding $\text{Ge}_{1-x}\text{Pb}_x$ alloys. In chapter 5 of this thesis a theoretical DFT-based analysis of the alloy's material, optical and electrical properties has been carried out. As is the case for GeSn alloys, optoelectronic devices made from GePb alloys should be compatible with CMOS technologies and easily integrable on to existing Si chip sets. The transition from an indirect to a direct band gap in GePb alloys is predicted to occur at a lower composition of Pb, than in equivalent GeSn alloys. The theoretical analysis of GePb alloys detailed in chapter 5 provide a detailed DFT-based inspection of the structural and electronic properties of the constituent materials; diamond-structured semiconducting Ge and diamond-structured metallic Pb, and (iii) the fictitious semi-metallic IV-IV compound zb-GePb, using both the HSEsol and mBJ XC functionals. Good agreement is found between the material properties, including lattice constants and indirect and direct material band gaps, calculated using HSE and mBJ DFT methods and the limited experimental data available, validating the suitability of these methods in the investigation of GePb alloys.

Examination of the calculated electronic structure of ordered GePb alloy supercells indicates that for both the $\text{Ge}_{63}\text{Pb}_1$ and $\text{Ge}_{127}\text{Pb}_1$ supercells analysed Pb incorporation splits the degeneracy of the Ge L_{6c} CB edge states into a (Kramers degenerate) singlet state, and lying slightly higher in energy, a (Kramers degenerate) triplet state which have purely s - and p -like orbital character at the Pb lattice site respectively. Hydrostatic pressure calculations carried out on these supercells indicate that the emergence of this s -like singlet state at the CB edge is not evidence of a direct band gap for Pb compositions as low as $x = 1.56\%$ as in both cases the calculated pressure coefficient of this singlet state at the conduction band edge possessed only a small admixture of direct (Ge Γ_{7c}) character and retained primarily indirect (Ge L_{6c}) character. Additionally these calculations establish the suitability of the mBJ XC functional in the analysis of $\text{Ge}_{1-x}\text{Pb}_x$ alloys. Using the mBJ XC functional the impact of Pb-related alloy disorder was then investigated by tracking the evolution of the alloy CB edge in $\text{Ge}_{62}\text{Pb}_2$ supercells as the separation between the Pb atoms was reduced from fourth- to first-nearest neighbours. Like in GeSn alloys, the alloy band gap here was found to have a strong dependence on the distance between the two Pb atoms indicating that atomic-scale alloy disorder strongly impacts quantitative analysis of the alloy electronic structure.

Finally the emergence of a direct band gap with increasing % Pb content for a randomly disordered alloy was analysed using $\text{Ge}_{128-x}\text{Pb}_x$ SQSs where x was varied from 0 – 12%. The calculated electronic structure evolution for these disordered 128-atom SQSs, in agreement with earlier ordered supercell calculations, showed that a (Kramers degenerate) singlet state emerges at the CB edge for even the lowest Pb composition considered ($x = 0.78\%$). Calculated pressure coefficients associated with the band gaps between the VB edge and the five lowest

energy (Kramers degenerate) CB states showed however that the CB edge retained primarily Ge L_{6c} character until $x \approx 6 - 7\%$, at which composition the lowest energy CB state acquired predominantly direct (Ge Γ_{7c}) character. As such, SQS calculations indicated an indirect- to direct-gap transition in $\text{Ge}_{1-x}\text{Pb}_x$ alloys for $x \approx 6 - 7\%$, near which composition the CB edge also passes through the VB edge, to give a zero-gap semi-metallic alloy. However finite-size effects in the SQSs, which arise from the absence of long-range alloy disorder in the relatively small supercells to which DFT calculations are limited are evidenced by the notably large splitting of the four Ge L_{6c} -derived states (the singlet state lying ≈ 150 meV below triplet states). We propose that these effects may lead to an overestimate of the composition at which $\text{Ge}_{1-x}\text{Pb}_x$ becomes direct-gap. Rather than finding such a splitting, we anticipate that the Ge L_{6c} character associated with alloy CB states will experience inhomogeneous broadening about their mean energy in real alloys. Plotting instead the weighted average of the four Ge L_{6c} -derived CB states we note the CB state which has the greatest Ge Γ_{7c} character passes through this weighted average energy for $x \approx 3 - 4\%$. This weighted average may then provide a more realistic estimate of the composition range in which $\text{Ge}_{1-x}\text{Pb}_x$ starts to become a direct-gap material, at which composition the calculated alloy band gap is in the range $0.3 - 0.4$ eV.

Overall the results of the analysis of GePb alloys indicate the emergence of a direct band gap in response to substitutional Pb incorporation in $\text{Ge}_{1-x}\text{Pb}_x$ alloys, and that band mixing effects in GePb alloys have a notably weaker impact on the evolution of the conduction band than in comparable GeSn alloys, suggesting the potential of these alloys for application as CMOS-compatible active photonic devices operating at mid-infrared wavelengths. We note however that the device applications of $\text{Ge}_{1-x}\text{Pb}_x$ alloys may in practice be limited by the presence of a low fundamental band gap and that further theoretical and experimental investigation of GePb alloys is still required for devices to be realised from this alloy.

6.4.1 Outlook, ongoing work and future work

The realisation of GePb alloys as a pathway to all group-IV CMOS devices will require a great deal of further research activity both on the theoretical and experimental sides. There remain a number of key issues for GePb alloys which must be overcome to create functional optoelectronic devices. Experimentally, difficulties remain in the growth of GePb alloys due to the large lattice mismatch between Ge and Pb and the tendency of Pb to energetically favour clustering together rather than distributing evenly throughout the alloy. The low band gap of direct gap GePb alloys predicted to lie in the range of $0.3 - 0.4$ eV may also present a barrier to the development of efficient active photonic components. This small band gap issue may potentially be overcome by the introduction of silicon to the alloy to form the ternary alloy $\text{Si}_y\text{Ge}_{1-x-y}\text{Pb}_x$, though there is to date little to no existing literature that investigates

this ternary alloy. DFT mBJ and tight binding methods like those detailed in chapter 4 of this thesis appear to offer the ideal means to investigate the $\text{Si}_y\text{Ge}_{1-x-y}\text{Pb}_x$ ternary alloy and identify the ideal y and x composition at which prospective devices might be made.

Bibliography

- [1] A. Capozzoli and G. Primiceri, “Global data center energy use: Distribution, composition, and near-term outlook,” E. R. Masanet et al. **Evanston, IL** (2018).
- [2] A. Capozzoli and G. Primiceri, “Cooling systems in data centers: state of art and emerging technologies,” Proceedings of the 7th International Conference on Sustainability in Energy and Buildings **83**, 484 (2015).
- [3] A. Liu, R. Jones, L. Liao, D. Samara-Rubio, D. Rubin, O. Cohen, R. Nicolaescu, and M. Paniccia, “A high-speed silicon optical modulator based on a metal–oxide–semiconductor capacitor,” Nature **427**, 615–618 (2004).
- [4] L. Alloatti, R. Palmer, S. Diebold, K. P. Pahl, B. Chen, R. Dinu, M. Fournier, J. Fedeli, T. Zwick, W. Freude, et al., “100 GHz silicon–organic hybrid modulator,” Light Science and Applications **3**, e173 (2014).
- [5] R. Palmer, S. Koeber, D. L. Elder, L. Woessner, W. Heni, D. Korn, M. Lauermann, W. Bogaerts, L. Dalton, W. Freude, et al., “High-Speed, Low Drive-Voltage Silicon–Organic Hybrid Modulator Based on a Binary-Chromophore Electro-Optic Material,” Journal of Lightwave Technology pp. 2726 – 2734 (2014).
- [6] D. Patel, A. Samani, V. Veerasubramanian, S. Ghosh, and D. V. Plant, “Silicon Photonic Segmented Modulator-Based Electro-Optic DAC for 100 Gb/s PAM-4 Generation,” IEEE Photonics technology Letters **27**, 2433 (2015).
- [7] J. Liu, D. D. Cannon, K. Wada, Y. Ishikawa, S. Jongthammanurak, D. T. Danielson, J. Michel, and L. C. Kimerling, “Tensile strained Ge p-i-n photodetectors on Si platform for C and L band telecommunications,” Applied Physics Letters **87**, 579–582 (2005).
- [8] G. T. Reed, W. R. Headley, and C. E. Png, “Silicon photonics: the early years,” Proceedings of SPIE Optoelectronic Integration on Silicon II **5730**, 1 (2005).
- [9] R. A. Soref and J. P. Lorenzo, “Single-crystal silicon: a new material for 1.3 and 1.6 μm integrated-optical components,” Electronics Letters **21**, 953 (1985).

- [10] A. Rickman, “The commercialization of silicon photonics,” *Nature Photonics* **8**, 579–582 (2014).
- [11] H. Lin, Z. Lou, T. Guo, L. C. Kimerling, K. Wada, and A. A. and J. Hu, “Mid-infrared integrated photonics on silicon: A perspective,” *Nanophotonics* **7**, 393 (2017).
- [12] M. Cardona and F. H. Pollak, “Energy-Band Structure of Germanium and Silicon: The $k \cdot p$ Method,” *Phys. Rev.* **142**, 530 (1966).
- [13] N. M. Park, T. S. Kim, and S. J. Park, “Band gap engineering of amorphous silicon quantum dots for light-emitting diodes,” *Appl. Phys. Lett.* **78**, 2575 (2001).
- [14] A. Shakoor, R. L. Savio, P. Cardile, S. L. Portalupi, D. Gerace, K. Welna, S. Boninelli, G. Franzò, F. Priolo, T. F. Krauss, et al., “Room temperature all-silicon photonic crystal nanocavity light emitting diode at sub-bandgap wavelengths,” *Laser and Photonics Reviews* **7**, 114 (2012).
- [15] W. L. Ng, M. A. Lourenco, R. M. Gwilliams, S. Ledain, G. Shao, and K. P. Homewood, “An efficient room-temperature silicon-based light-emitting diode,” *Nature* **410**, 192 (2001).
- [16] M. A. Lourenco, M. S. A. Siddiqui, G. M. Gwilliams, G. Shao, and K. P. Homewood, “Efficient silicon light emitting diodes made by dislocation engineering,” *Physica E: Low-dimensional Systems and Nanostructures* **16**, 376 (2003).
- [17] V. G. and P. Basmaji, “Optical absorption in porous silicon of high porosity,” *Thin Solid Films* **235**, 234 (1993).
- [18] O. Bisi, S. Ossicini, and L. Pavesi, “Porous silicon: a quantum sponge structure for silicon based optoelectronics,” *Surf. Sci. Rep* **38**, 1 (2000).
- [19] S. G. Cloutier, P. A. Kosyrev, and J. Xu, “Optical gain and stimulated emission in periodic nanopatterned crystalline silicon,” *Nat. Mat.* **4**, 887 (2005).
- [20] L. Pavesi, L. D. Negro, C. M. G. Franzò, and F. Priolo, “Optical gain in silicon nanocrystals,” *Nature* **408**, 440 (2000).
- [21] L. Pavesi, Z. Gaburro, L. D. Negro, P. Bettotti, G. V. Prakash, M. Cazzanelli, and C. J. Oton, “Nanostructured silicon as a photonic material,” *Opt. Lasers Eng.* **39**, 345–368, (2003).
- [22] W. L. Wilson, P. F. Szajowski, and L. E. Brus, “Quantum confinement in size-selected surface-oxidized silicon nanocrystals,” *Science* **262**, 1242–1244 (1993).
- [23] Z. H. Lu, D. J. Lockwood, and J. M. Baribeau, “Quantum confinement and light emission in SiO_2/Si superlattices,” *Nature* **378**, 258–260 (1995).

- [24] M. V. Fischetti and S. E. Laux, "Band structure, deformation potentials, and carrier mobility in strained Si, Ge, and SiGe alloys," *J. Appl. Phys.* **80**, 2234 (1996).
- [25] J. Liu, X. Sun, D. Pan, X. Wang, L. Kimerling, T. Koch, and J. Michel, "Tensile-strained, n-type Ge as a gain medium for monolithic laser integration on Si.," *Opt. Express* **15**, 11272–11277 (2007).
- [26] P. H. Lim, S. Park, Y. Ishikawa, and K. Wada, "Enhanced direct bandgap emission in germanium by micromechanical strain engineering," *Optical Express* **17**, 16358 (2009).
- [27] M. E. Kurdi, G. Fishman, S. Sauvage, and P. Boucaud, "Band structure and optical gain of tensile-strained germanium based on a 30 band $k \cdot p$ formalism," *J. Appl. Phys.* **107**, 013710 (2010).
- [28] G. Pizzi, M. Virgilio, and G. Grosso, "Tight-binding calculation of optical gain in tensile strained [001]-Ge/SiGe quantum wells," *Nanotechnology* **21**, 055202 (2009).
- [29] J. Liu, R. Camacho-Aguilera, J. Bessette, X. Sun, X. Wang, Y. Cai, L. C. Kimerling, and J. Michel, "Ge-on-Si optoelectronics.," *Thin Solid Films* **520**, 3354–3360 (2012).
- [30] M. J. Süess, R. Geiger, R. A. Minamisawa, G. Schiefler, J. Frigerio, D. Christina, G. Isella, R. Spolenak, J. Faist, and H. Sigg, "Analysis of enhanced light emission from highly strained germanium microbridges," *Nat. Photon.* **7**, 466–472 (2013).
- [31] J. R. Jain, A. Hryciw, T. M. Baer, D. A. B. Miller, and M. L. Brongersma, "A micromachining-based technology for enhancing germanium light emission via tensile strain," *Nat. Photon.* **6**, 398 (2012).
- [32] H. Landolt and R. Börnstein, "Landolt-Börnstein: Condensed Matter," **III/41A1a** (1982).
- [33] T. Brudevoll, D. S. Citrin, N. E. Christensen, and M. Cardona, "Calculated band structure of zinc-blende-type SnGe," *Phys. Rev. B* **48**, 17128 (1993).
- [34] G. He and H. Atwater, "Interband Transitions in $\text{Sn}_x\text{Ge}_{1-x}$ Alloys.," *Phys. Rev. Lett.* **79**, 1937 (1997).
- [35] R. Soref, "Mid-infrared photonics in silicon and germanium.," *Nat. Photonics* **4**, 495 (2010).
- [36] B. Dutt, H. Lin, D. S. Sukhdeo, B. Vulovic, S. Gupta, D. Nam, K. Saraswat, and J. Harris, "Theoretical analysis of GeSn alloys as a gain medium for a Si-compatible laser," *IEEE J. Sel. Top. Quantum Electron* **19**, 1502706 (2013).

- [37] S. Wirths, Z. Ikonc, A. Tiedemann, B. H. T. Stoica, G. Mussler, U. Breuer, J. M. Hartmann, A. Benedetti, S. Chiussi, D. Grützmacher, et al., “Tensely strained GeSn alloys as optical gain media.,” *Appl. Phys. Lett.* **103**, 192110 (2013).
- [38] D. A. B. Miller, “Device requirements for optical interconnects to silicon chips,” *Proceedings of IEEE* **97**, 1166–1185 (2009).
- [39] J. Liu, H. Deng, W. Zhang, and J. Yao, “On-Chip Sensor for Simultaneous Temperature and Refractive Index Measurements Based on a Dual-Passband Microwave Photonic Filter,” *IEEE Journal of Lightwave Technology* **36**, 4099 (2018).
- [40] V. M. Lavchiev and B. Jakoby, “Photonics in the Mid-Infrared: Challenges in Single-Chip Integration and Absorption Sensing,” *IEEE J. Sel. Top. Quantum Electron.* **23**, 452 (2017).
- [41] S. Gupta, B. Magyari-Kope, Y. Nishi, and K. Saraswat, “Achieving direct band gap in germanium through integration of Sn alloying and external strain.,” *J. Appl. Phys.* **113**, 073707 (2013).
- [42] P. Moontragoon, Z. Ikonc, and P. Harrison, “Band structure calculations of si-ge-sn alloys: achieving direct band gap materials.,” *Semiconductor Science and Technology* **22**, 742 (2007).
- [43] W. Yin, X. Gong, and H. Wei, “Origin of the unusually large band-gap bowing and the breakdown of the band-edge distribution rule in the $\text{Sn}_x\text{Ge}_{1-x}$ alloys.,” *Phys. Rev. B* **78**, 1 (2008).
- [44] Y. Chibane and M. Ferhat, “Electronic structure of $\text{Sn}_x\text{Ge}_{1-x}$ alloys for small Sn compositions: Unusual structural and electronic properties.,” *J. Appl. Phys.* **107**, 053512 (2010).
- [45] W. Huang, B. Cheng, C. Xue, and H. Yang, “The band structure and optical gain of a new IV-group alloy GePb: a first principles calculation,” *J. Alloy Compd.* **701**, 816 (2017).
- [46] S. Wirths, R. Geiger, N. von den Driesch, G. Mussler, T. Stoica, S. Mantl, Z. Ikonc, M. Luysberg, S. Chiussi, J. Hartmann, et al., “Lasing in direct-bandgap GeSn alloy grown on si,” *Nature Photonics* **9**, 88 (2015).
- [47] D. Rainko, Z. Ikonc, A. Elbaz, N. von den Driesch, D. Stange, E. Herth, P. Boucaud, M. E. Kurdi, D. Grützmacher, and D. Buca, “Impact of tensile strain on low Sn content GeSn lasing,” *Scientific Reports* **9**, 259 (2019).
- [48] K. P. Homewood and M. A. Lourenco, “Optoelectronics: The rise of the GeSn laser.,” *Nature Photonics* **9**, 78 (2015).

- [49] C. Hu, "Green transistor as a solution to the IC power crisis," International Conference on Solid-State and Integrated Circuits Technology Proceedings pp. 16–19 (2008).
- [50] S. Sant and A. Schenk, "Pseudopotential calculations of strained-GeSn / SiGeSn heterostructures.," Appl. Phys. Lett. **105**, 1 (2014).
- [51] B. R. Conley, H. Naseem, G. Sun, P. Sharps, and S. Q. Yu, "High efficiency MJ solar cells and TPV using SiGeSn materials," Proceedings of 38th IEEE Photovoltaic Specialists Conference (2012).
- [52] R. Geigerand, T. Zabel, and H. Sigg, "Group iv direct band gap photonics: methods, challenges, and opportunities," Frontiers in Materials **2**, 52 (2015).
- [53] F. Bloch, "Über die quantenmechanik der elektronen in kristallgittern," Zeitschrift für Physik **52**, 555 (1929).
- [54] N. W. Ashcroft and N. D. Mermin, "Solid state Physics," Holt Rinehart and Winston (1976).
- [55] P. Yu and M. Cardona, "Fundamentals of Semiconductors," Springer (2010).
- [56] R. M. Martin, "Elastic properties of zns structure semiconductors," Phys. Rev. B **1**, 4005 (1970).
- [57] M. Born and R. Oppenheimer, "Zur quantentheorie der molekeln.," Annalen der Physik pp. 389–457 (1927).
- [58] L. H. Thomas, "The calculation of atomic fields.," Math. Proc. Cambridge **23**, 542 (1927).
- [59] E. Fermi, "Un metodo statistico per la determinazione di alcune priorietà dell'atome," Rend. Accad. Naz. Lincei **6**, 32 (1927).
- [60] W. Kohn and L. J. Sham, "Self-consistent equations including exchange and correlation effects.," Phys. Rev. **140**, A1133 (1965).
- [61] P. Hohenberg and W. Kohn, "Inhomogeneous electron gas.," Phys. Rev. **136**, B864 (1964).
- [62] J. P. Perdew and A. Zunger, "Self-interaction correction to density-functional approximations for many-electron systems," Phys. Rev. B. **23**, 5048 (1981).
- [63] D. M. Ceperley and B. J. Alder, "Ground State of the Electron Gas by a Stochastic Method," Phys. Rev. Lett. **45**, 566 (1980).
- [64] F. Herman, C. D. Kuglin, K. F. Cuff, and R. L. Kortum, "Relativistic corrections to the band structure of tetrahedrally bonded semiconductors," Phys. Rev. Lett. **11**, 541 (1963).

- [65] P. S. Svendsen and U. von Barth, "Gradient expansion of the exchange energy from second-order density response theory," *Phys. Rev. B.* **54**, 17402 (1996).
- [66] J. P. Perdew, K. Burke, and M. Ernzerhof, "Generalized Gradient Approximation Made Simple," *Phys. Rev. Lett* **77**, 3865 (1996).
- [67] A. D. Becke, "Density-functional exchange-energy approximation with correct asymptotic behavior," *Phys. Rev. A* **38**, 3098 (1988).
- [68] J. P. Perdew and Y. Wang, "Accurate and simple analytic representation of the electron-gas correlation energy," *Phys. Rev. B* **45**, 13244 (1992).
- [69] R. M. Martin, "Electronic structure.," Cambridge University Press (2004).
- [70] M. Ernzerhof, J. P. Perdew, and K. Burke, "Coupling-Constant Dependence of Atomization Energies," *Int. J. Quant. Chem.* **64**, 285 (1996).
- [71] D. R. Hamann, "Generalized Gradient Theory for Silica Phase Transitions," *Phys. Rev. Lett.* **76**, 660 (1995).
- [72] A. Zoroddu, F. Bernardini, P. Ruggerone, and V. Fiorentini, "First-principles prediction of structure, energetics, formation enthalpy, elastic constants, polarization, and piezoelectric constants of AlN, GaN, and InN: Comparison of local and gradient-corrected density-functional theory.," *Phys. Rev. B.* **64**, 045208 (2001).
- [73] J. P. Perdew and M. Levy, "Physical content of the exact Kohn-Sham orbital energies: Band gaps and derivative discontinuities.," *Phys. Rev. Lett.* **51**, 1884 (1983).
- [74] A. D. Becke and E. R. Johnson, "A simple effective potential for exchange," *J. Chem. Phys.* **124**, 221101 (2006).
- [75] F. Tran and P. Blaha, "Accurate band gaps of semiconductors and insulators with a semilocal exchange-correlation potential," *Phys. Rev. Lett.* **226401**, 102 (2009).
- [76] A. D. Becke and M. R. Roussel, "Exchange holes in inhomogeneous systems: A coordinate-space model," *Phys. Rev. A* **39**, 3761 (1989).
- [77] F. Tran, P. Blaha, and K. Schwarz, "Band gap calculations with Becke–Johnson exchange potential," *J. Phys. Condens. Matter.* **19**, 196208 (2006).
- [78] J. Heyd, G. E. Scuseria, and M. Ernzerhof, "Hybrid functionals based on a screened Coulomb potential," *J. Chem. Phys.* **118**, 8207 (2003).
- [79] J. Heyd and G. E. Scuseria, "Hybrid functionals based on a screened Coulomb potential: Assessment of the Heyd-Scuseria-Ernzerhof screened Coulomb hybrid functional," *J. Chem. Phys.* **121**, 1187 (2004).

- [80] J. P. Perdew and M. Ernzerhof, "Rationale for mixing exact exchange with density functional approximations," *J. Chem. Phys.* **105**, 9982 (1996).
- [81] M. Ernzerhof and G. E. Scuseria, "Assessment of the Perdew–Burke–Ernzerhof exchange–correlation functional," *J. Chem. Phys.* **110**, 5029 (1999).
- [82] C. Adamo, "Toward reliable density functional methods without adjustable parameters: The PBE0 model," *J. Chem. Phys.* **110**, 6158 (1999).
- [83] T. M. H. J. Paier and G. E. Scuseria, "Accurate treatment of solids with the HSE screened hybrid," *Phys. Stat. Sol. B* **248**, 767 (2011).
- [84] J. Paier, M. Marsman, K. Hummer, G. Kresse, I. C. Gerber, and J. G. Angyan., "Screened hybrid density functionals applied to solids," *J. Chem. Phys.* **124**, 154709 (2006).
- [85] P. E. Blöchl, "Projector augmented-wave method," *Phys. Rev. B* **50**, 17953 (1994).
- [86] J. C. Phillips, "Energy-band interpolation scheme based on a pseudopotential," *Phys. Rev.* **112**, 685 (1958).
- [87] J. C. Phillips and L. Kleinman, "New method for calculating wave functions in crystals and molecules," *Phys. Rev.* **116**, 287 (1959).
- [88] V. Heine, "The pseudopotential concept," *Solid State Physics* **24**, 1 (1970).
- [89] M. Rohlfing, P. Krüger, and J. Pollmann, "Role of semicore d electrons in quasiparticle band-structure calculations," *Phys. Rev. B* **57**, 6485 (1998).
- [90] V. Fiorentini, M. Methfessel, and M. Scheffler, "Electronic and structural properties of GaN by the full-potential linear muffin-tin orbitals method: The role of the d electrons," *Phys. Rev. B* **47**, 13353 (1993).
- [91] D. R. Hamann, M. Schülter, and C. Chiang, "Norm-conserving pseudopotentials," *Phys. Rev. Lett.* **43**, 1494 (1979).
- [92] D. Vanderbilt, "Soft self-consistent pseudopotentials in a generalized eigenvalue formalism," *Phys. Rev. B* **41**, 7892(R) (1990).
- [93] G. Kresse and D. Joubert, "From ultrasoft pseudopotentials to the projector augmented-wave method," *Phys. Rev. B* **59**, 1758 (1999).
- [94] G. Kresse and J. Hafner, "Ab initio molecular dynamics for liquid metals," *Phys. Rev. B* **47**, 558R (1993).
- [95] G. Kresse and J. Furthmüller, "Efficiency of ab-initio total energy calculations for metals and semiconductors using a plane-wave basis set," *Comput. Mater. Sci.* **6**, 15 (1996).

- [96] G. Kresse and J. Furthmüller, “Efficient iterative schemes for ab initio total-energy calculations using a plane-wave basis set,” *Phys. Rev. B* **54**, 11169 (1996).
- [97] P. Medeiros, S. Strafström, and J. Björk, “Effects of extrinsic and intrinsic perturbations on the electronic structure of graphene: Retaining an effective primitive cell band structure by band unfolding,” *Phys. Rev. B* **89**, 041407 (2014).
- [98] P. Medeiros, S. S. T. S. Strafström, and J. Björk, “Unfolding spinor wave functions and expectation values of general operators: Introducing the unfolding-density operator,” *Phys. Rev. B* **91**, 041116(R) (2015).
- [99] V. Popescu and A. Zunger, “Extracting E versus k effective band structure from supercell calculations on alloys and impurities,” *Phys. Rev. B* **85**, 085201 (2012).
- [100] L.-W. Wang, L. Bellaiche, S. H. Wei, and A. Zunger, “Majority Representation” of Alloy Electronic States,” *Phys. Rev. Lett.* **80**, 4725 (1998).
- [101] E. Kasper, M. Kittler, M. Oehme, and T. Arguirov, “Germanium tin: silicon photonics toward the mid-infrared,” *Photonics Res.* **1**, 69 (2013).
- [102] D. Liang and J. Bowers, “Recent progress in lasers on silicon,” *Nat. Photonics* **4**, 511 (2010).
- [103] S. Chen, W. Li, J. Wu, Q. Jiang, M. Tang, S. Shutts, S. Elliott, A. Sobiesierski, A. Seeds, I. Ross, et al., “Electrically pumped continuous-wave III–V quantum dot lasers on silicon. *Nat. Photonics*,” *Nat. Photonics* **10**, 307 (2016).
- [104] J. Justice, C. Bower, M. Meitl, M. Mooney, M. Gubbins, and B. Corbett, “Wafer-scale integration of group III-V lasers on silicon using transfer printing of epitaxial layers,” *Nat. Photonics* **6**, 610 (2012).
- [105] H. Yang, D. Zhao, S. Chuwongin, J. Seo, W. Yang, Y. Shuai, J. Berggren, M. Hammar, and Z. M. . W. Zhou, “Transfer-printed stacked nanomembrane lasers on silicon,” *Nat. Photonics* **6**, 617 (2012).
- [106] Z. Wang, B. Tian, M. Pantouvak, W. Guo, P. Absil, J. V. Campenhout, C. Merckling, and D. V. Thourhout, “Room Temperature InP DFB Laser Array Directly Grown on (001) Silicon,” *Nat. Photonics* **9**, 837 (2015).
- [107] G. Read, I. Marko, N. Hossain, and S. Sweeney, “Physical properties and characteristics of III-V lasers on silicon,” *IEEE J. Sel* **21**, 1502208 (2015).
- [108] L. Liu, R. Liang, J. Wang, L. Xiao, and J. Xu, “Simulation of GeSn/Ge tunneling field-effect transistors for complementary logic applications,” *J.Appl.Phys.Express* **9**, 091301 (2016).

- [109] K. Kumar, Y.-F. Hsieh, J.-H. Liao, K.-H. Kao, and Y.-H. Wang, “Significance of Multivalley and Nonparabolic Band Structure for GeSn TFET Simulation,” *IEEE Trans. Electron Devices* **65**, 4709–4715 (2018).
- [110] M. van Loon, N. Stavrias, N. Le, K. Litvinenko, P. Greenland, C. Pidgeon, K. Saeedi, B. Redlich, G. Aeppli, and B. Murdin, “Giant multiphoton absorption for THz resonances in silicon hydrogenic donors,” *Nat. Photonics* **12**, 179–184 (2018).
- [111] F. D. Leonardis, B. Troia, R. Soref, and V. Passaro, “Dispersion of nonresonant third-order non-linearities in GeSiSn ternary alloys,” *Sci. Rep.* **6**, 32622 (2017).
- [112] L. Jin, D. Zhang, H. Zhang, J. Fang, Y. Liao, T. Zhou, C. Liu, Z. Zhong, and V. Harris, “Large area Germanium Tin nanometer optical film coatings on highly flexible aluminum substrates,” *Sci. Rep.* **6**, 34030 (2016).
- [113] S. Biswas, J. Doherty, D. Saladukha, Q. Ramasse, D. Majumdar, M. Upmanyu, A. Singha, T. Ochalski, M. Morris, and J. Holmes, “Non-equilibrium induction of tin in germanium towards direct GeSn nanowires,” *Nat. Commun.* **7**, 1 (2015).
- [114] D. Stange, S. Wirths, R. Geiger, C. Schulte-Braucks, B. Marzban, N. von den Driesch, G. Mussler, T. Zabel, T. Stoica, J.-M. Hartmann, et al., “Optically Pumped GeSn Microdisk Lasers on Si,” *ACS Photonics* **3**, 1279–1285 (2016).
- [115] J. Margetis, S. Al-Kabi, W. Du, W. Dou, Y. Zhou, T. Pham, P. Grant, S. Ghetmiri, A. Mosleh, B. Li, et al., “Si-Based GeSn Lasers with Wavelength Coverage of 2–3 μm and Operating Temperatures up to 180 K,” *ACS Photonics* **5**, 827 (2018).
- [116] D. Stange, N. von den Driesch, T. Z. F. Armand-Pilon, D. Rainko, B. Marzban, P. Zaumseil, J.-M. Hartmann, Z. Ikonik, G. Capellini, S. Mantl, et al., “GeSn/SiGeSn Heterostructure and Multi Quantum Well Lasers,” *ACS Photonics* **5**, 4628 (2018).
- [117] H. S. Maczko, R. Kudrawiec, and M. Gladysiewicz, “Material gain engineering in GeSn/Ge quantum wells integrated with an Si platform,” *Sci. Rep.* **6**, 34082 (2016).
- [118] G. Sun, R. Soref, and H. Cheng, “Design of a Si-based lattice-matched room-temperature GeSn / GeSiSn multi-quantum-well mid-infrared laser diode,” *Opt. Express* **18**, 19957–19965 (2010).
- [119] P. Moontragoon, R. Soref, and Z. Ikonik, “The direct and indirect bandgaps of unstrained $\text{Si}_x\text{Ge}_{1-x-y}\text{Sn}_y$ and their photonic device applications,” *J. Appl. Phys.* **112**, 073106 (2012).
- [120] S. Tomić and E. O’Reilly, “Gain characteristics of ideal dilute nitride quantum well lasers,” *Phys. E Low-Dimensional Syst. Nanostructures* **13**, 1102 (2002).

- [121] A. Pan and C. Chui, “Modeling direct interband tunneling. I. Bulk semiconductors,” *J. Appl. Phys.* **116**, 054508 (2014).
- [122] A. Lindsay and E. P. O’Reilly, “Theory of enhanced bandgap non-parabolicity in $\text{GaN}_x\text{As}_{1-x}$ and related alloys,” *Solid State Commun.* **112**, 443 (1999).
- [123] S. Wei and A. Zunger, “Predicted band-gap pressure coefficients of all diamond and zinc-blende semiconductors: Chemical trends,” *Phys. Rev. B* **60**, 5404–5411 (1999).
- [124] C. Eckhardt, K. Hummer, and G. Kresse, “Indirect-to-direct gap transition in strained $\text{Sn}_x\text{Ge}_{1-x}$ alloys,” *Phys. Rev. B* **89**, 65201 (2014).
- [125] D. Jenkins and J. Dow, “Electronic properties of metastable $\text{Ge}_x\text{Sn}_{1-x}$ alloys,” *Phys. Rev. B* **36**, 7994 (1987).
- [126] F. Dybala, K. Zelazna, H. Maczko, M. Gladysiewicz, J. Misiewicz, R. Kudrawiec, H. Lin, R. Chen, C. Shang, Y. Huo, et al., “Electromodulation spectroscopy of direct optical transitions in $\text{Ge}_{1-x}\text{Sn}_x$ layers under hydrostatic pressure and built-in strain,” *J. Appl. Phys.* **119**, 215703 (2016).
- [127] H. Lin, R. Chen, W. Lu, Y. Huo, T. Kamins, and J.S.Harris, “Investigation of the direct band gaps in $\text{Ge}_{1-x}\text{Sn}_x$ alloys with strain control by photoreflectance spectroscopy,” *Appl. Phys. Lett.* **100**, 102109 (2012).
- [128] K. Zelazna, M. Polak, P. Scharoch, J. Serafinczuk, M. Gladysiewicz, J. Misiewicz, J. Dekoster, and R. Kudrawiec, “Electronic band structure of compressively strained $\text{Ge}_{1-x}\text{Sn}_x$ with $x < 0.11$ studied by contactless electroreflectance,” *Appl. Phys. Lett.* **106**, 142102 (2015).
- [129] A. Lindsay and E. O’Reilly, “Unification of the band anticrossing and cluster-state models of dilute nitride semiconductor alloys,” *Phys. Rev. Lett.* **93**, 3 (2004).
- [130] W. Shan, W. Walukiewicz, J. Ager, E. Haller, J. Geisz, D. Friedman, J. Olson, and S. Kurtz, “Band Anticrossing in GaInNAs Alloys,” *Phys. Rev. Lett.* **82**, 1221–1224 (1999).
- [131] T. D. Eales, I. P. Marko, S. A. Ghetmiri, W. Du, Y. Zhou, S. Q. g Yu, J. Margetis, J. Tolle, S. Schulz, E. J. O’Halloran, et al., “New experimental evidence for nature of the band gap of gesn alloys,” *Silicon Photonics XII Conference* **10108**, 101080F (2017).
- [132] L. Kronik and Y. Shapira, “Surface photovoltage phenomena: theory, experiment, and applications,” *Surface Science Reports* **37**, 1 (1999).
- [133] M. Oehme, K. KostECKI, M. Schmid, M. Kaschel, M. Gollhofer, K. Ye, D. Widmann, R. Koerner, S. Bechler, E. Kasper, et al., “Franz-Keldysh effect in GeSn pin photodetectors,” *Appl. Phys. Lett.* **104**, 161115 (2014).

- [134] L. Schimka, J. Harl, and G. Kresse, “Improved hybrid functional for solids: The HSEsol functional,” *J. Chem. Phys.* **134**, 1 (2011).
- [135] M. Polak, P. Scharoch, and R. Kudrawiec, “The electronic band structure of $\text{Ge}_{1-x}\text{Sn}_x$ in the full composition range: indirect, direct, and inverted gaps regimes, band offsets, and the burstein–moss effect.,” *Journal of Physics D: Applied Physics* **50**, 195103 (2017).
- [136] S. Kűfner, J. Furthműller, L. Matthes, M. Fitzner, and F. Bechstedt, “Structural and electronic properties of α -tin nanocrystals from first principles.,” *Phys. Rev. B.* **87**, 235307 (2013).
- [137] S. H. Groves, C. R. Pidgeon, and R. J. Wagner, “Interband magnetoreflexion of α -Sn,” *J. Phys. Chem. Solids* **31**, 2031 (1970).
- [138] M. Cardona and W. Paul, “Pressure dependence of the direct energy gap in germanium.,” *J. Phys. Chem. Solids* **17**, 128 (1960).
- [139] B. Welber, M. Cardona, Y.-F. Tsay, and B. Bendow, “Effect of hydrostatic pressure on the direct absorption edge of germanium.,” *Phys. Rev. B* **15**, 875–879 (1977).
- [140] A. Goni, K. Syassen, K. Strossner, and M. Cardona, “Pressure dependence of the direct optical gap and refractive index of Ge and GaAs.,” *Semicond. Sci. Technol.* **4**, 246 (1989).
- [141] Y. Zhou, W. Dou, W. Du, T. Pham, S. Ghetmiri, S. Al-Kabi, A. Mosleh, M. Alher, J. Margetis, J. Tolle, et al., “Systematic study of GeSn heterostructure-based light-emitting diodes towards mid-infrared applications.,” *J. Appl. Phys.* **120**, 023102 (2016).
- [142] J. Pankove, “Fundamental Absorption in Optical processes in semiconductors,” Dover Publication pp. 34–52 (1975).
- [143] A. Goni, K. Strössner, K. Syassen, and M. Cardona, “Pressure dependence of direct and indirect optical absorption in GaAs.,” *Phys. Rev. B* **36**, 1581–1587 (1987).
- [144] U. Venkateswaran, M. Chandrasekhar, H. Chandrasekhar, B. Vojak, F. Chambers, and J. Meese, “High pressure study of $\text{GaAsAl}_x\text{Ga}_{1-x}\text{As}$ quantum wells at low temperatures.,” *Superlattices Microstruct.* **3**, 217–223 (1987).
- [145] R. Warburton, R. Nicholas, N. Mason, P. Walker, A. Prins, and D. Dunstan, “High-pressure investigation of GaSb and $\text{Ga}_{1-x}\text{In}_x\text{Sb}/\text{GaSb}$ quantum wells.,” *Phys. Rev. B* **43**, 4994–5000 (1991).
- [146] H. P. Zhou and M. Sotomayor-Torres, “Luminescence properties of $\text{Al}_{0.48}\text{In}_{0.52}\text{As}$ under hydrostatic pressure.,” *Proceedings of SPIE: Spectroscopic Characterization Techniques for Semiconductor Technology IV* **1678**, 96 (1992).

- [147] L. Jiang, C. Xu, J. Gallagher, R. Favaro, T. Aoki, J. Menéndez, and J. Kouvetakis, “Development of light emitting group IV ternary alloys on Si platforms for long wavelength optoelectronic applications,” *Chem. Mater.* **26**, 2522–2531 (2014).
- [148] D. Stange, S. Wirths, N. von den Driesch, G. Mussler, T. Stoika, Z. Ikonc, J.-M. Hartmann, S. Mantl, D. Grutzmacher, and D. Buca, “Optical Transitions in Direct-Bandgap $\text{Ge}_1 - x\text{Sn}_x$ Alloys,” *ACS Photonics* **2**, 1539–1545 (2015).
- [149] T. Brudevoll, D. S. Citrin, M. Cardona, and N. E. Christensen, “Electronic structure of α -Sn and its dependence on hydrostatic strain,” *Phys. Rev. B* **48**, 8629 (1993).
- [150] M. J. P. Musgrave and J. A. Pople, “A general valence force field for diamond,” *Proc. R. Soc. Lond. A* **268**, 474 (1962).
- [151] D. S. P. Tanner, M. A. Caro, S. Schulz, and E. P. O’Reilly, “Fully analytic valence force field model for the elastic and inner elastic properties of diamond and zincblende crystals,” *Phys. Rev. B* **100**, 094112 (2019).
- [152] D. S. P. Tanner, C. A. Broderick, A. C. Kirwan, S. Schulz, and E. P. O’Reilly, “Elastic properties of elemental and compound group-iv materials: hybrid density functional theory and valence force field parametrisation,” in preparation (2018).
- [153] P. Vogl, H. P. Hjalmarson, and J. D. Dow, “A semi-empirical tight-binding theory of the electronic structure of semiconductors,” *J. Phys. Chem. Solids* **44**, 365 (1983).
- [154] A. Hermann, J. Furthmüller, H. W. Gäggeler, and P. Schwerdtfeger, “Spin-orbit effects in structural and electronic properties for the solid state of the group-14 elements from carbon to superheavy element 114,” *Phys. Rev. B* **82**, 155116 (2010).
- [155] H. Landolt and R. Börnstein, “Landolt-Börnstein: Condensed Matter,” **III/41A1b** (1982).
- [156] H. Rücker and M. Methfessel, “Anharmonic Keating model for group-IV semiconductors with applications to lattice dynamics in alloys of Si, Ge and C,” *Phys. Rev. B* **52**, 11509 (1995).
- [157] R. Pandey, M. Rérat, and M. Causà, “First-principles study of stability, band structure, and optical properties of the ordered $\text{Ge}_{0.50}\text{Sn}_{0.50}$ alloy,” *Appl. Phys. Lett.* **75**, 4127 (1999).
- [158] R. Khenata, H. Baltache, M. Sahnoun, M. Driz, M. Rérat, and B. Abbar, “Full potential linearized augmented plane wave calculations of structural and electronic properties of GeC, SnC and GeSn,” *Physica B* **336**, 321 (2003).

- [159] T. D. Eales, I. P. Marko, S. S. Schulz, E. J. O'Halloran, S. Ghetmiri, W. Du, Y. Zhou, S. Q. Yu, J. Margetis, J. Tolle, et al., "Ge_{1-x}Sn_x alloys: Consequences of band mixing effects for the evolution of the band gap γ -character with Sn concentration," *Scientific Reports* **9**, 14077 (2019).
- [160] A. van de Walle, M. Asta, and G. Ceder, "The Alloy Theoretic Automated Toolkit: A User Guide," *J. Calphad* **26**, 539 (2002).
- [161] A. van de Walle, "Multicomponent multisublattice alloys, nonconfigurational entropy and other additions to the Alloy Theoretic Automated Toolkit," *J. Calphad* **33**, 266 (2009).
- [162] A. van de Walle, P. Tiwarya, M. de Jong, L. Olmsted, A. Dick, D. Shin, Y. Wang, L.-Q. Chen, and Z.-K. Liu, "Efficient stochastic generation of special quasirandom structures," *J. Calphad* **42**, 13 (2013).
- [163] A. Zunger, S.-H. Wei, L. G. Ferreira, and J. E. Bernard, "Special quasirandom structures," *Phys. Rev. Lett.* **65**, 353 (1990).
- [164] S.-H. Wei, L. G. Ferreira, J. E. Bernard, and A. Zunger, "Electronic properties of random alloys: special quasirandom structures," *Phys. Rev. B* **42**, 9622 (1990).
- [165] D. J. Chadi, "Spin-orbit splitting in crystalline and compositionally disordered semiconductors," *Phys. Rev. B* **16**, 790 (1977).
- [166] T. B. Boykin, G. Klimeck, R. C. Bowen, and R. Lake, "Effective-mass reproducibility of the nearest-neighbor sp^3s^* models: analytic results," *Phys. Rev. B* **56**, 4102 (1997).
- [167] D. J. Chadi and M. L. Cohen, "Tight-binding calculations of the valence bands of diamond and zincblende crystals," *Phys. Stat. Solidi B* **68**, 405 (1975).
- [168] E. P. O'Reilly, A. Lindsay, S. Tomić, and M. Kamal-Saadi, "Tight-binding and $\mathbf{k}\cdot\mathbf{p}$ models for the electronic structure of Ga(In)NAs and related alloys," *Semicond. Sci. Technol.* **17**, 870 (2002).
- [169] M. Usman, C. A. Broderick, A. Lindsay, and E. P. O'Reilly, "Tight-binding analysis of the electronic structure of dilute bismide alloys of GaP and GaAs," *Phys. Rev. B* **84**, 245202 (2011).
- [170] M. Usman, C. A. Broderick, and E. P. O'Reilly, "Impact of disorder on the optoelectronic properties of GaN_yAs_{1-x-y}Bi_x alloys and heterostructures," *Phys. Rev. Applied* **10**, 044024 (2018).
- [171] S. Schulz, M. A. Caro, L.-T. Tan, P. J. Parbrook, R. W. Martin, and E. P. O'Reilly, "Composition-dependent band gap and band-edge bowing in AlInN: a combined theoretical and experimental study," *Appl. Phys. Express.* **6**, 121001 (2013).

- [172] M. A. Caro, S. Schulz, and E. P. O'Reilly, "Theory of local electric polarization and its relation to internal strain: impact on polarization potential and electronic properties of group-III nitrides," *Phys. Rev. B* **88**, 214103 (2013).
- [173] J. von Pezold, A. Dick, M. Friàk, and J. Neugebauer, "Generation and performance of special quasirandom structures for studying the elastic properties of random alloys: application to Al-Ti," *Phys. Rev. B* **81**, 094203 (2010).
- [174] Y. R. D'Costa, C. S. Cook, A. G. Birdwell, C. L. Littler, M. Canonico, S. Zollner, J. Kouvetakis, and J. Menéndez, "Optical critical points of thin-film $\text{Ge}_{1-y}\text{Sn}_y$ alloys: A comparative $\text{Ge}_{1-y}\text{Sn}_y / \text{Ge}_{1-x}\text{Si}_x$ study," *Phys Rev. B* **73**, 125207 (2006).
- [175] W. Huang, B. Cheng, C. Xue, and C. Li, "Comparative studies of clustering effect, electronic and optical properties of GePb and GeSn alloys with low Pb and Sn concentration," *Physica B* **443**, 43 (2014).
- [176] X. Liu, J. Zheng, L. Zhou, Z. Liu, Y. Zuo, C. Xueab, and B. Cheng, "Growth of single crystalline GePb film on Ge substrate by magnetron sputtering epitaxy," *J. Alloy Compd.* **785**, 228 (2019).
- [177] Q. Zhou, T. K. Chan, S. L. Lim, C. Zhan, T. Osipowicz, X. Gong, E. S. Tok, and Y. C. Yeo, "Single Crystalline Germanium-Lead Alloy on Germanium Substrate Formed by Pulsed Laser Epitaxy," *ECS Solid State Letters* **3**, 91 (2014).
- [178] H. Alahmad, A. Mosleh, M. Alher, S. Fahimeh, Banihashemian, S. A. Ghetmiri, S. Al-Kabi, W. Du, B. Li, S.-Q. Yu, et al., "GePb alloy growth using layer inversion method," *J. Electron. Mater.* **47**, 3733 (2018).
- [179] N. E. Christensen, S. Satpathy, and Z. Pawlowska, "First-principles theory of tetrahedral bonding and crystal structure of lead," *Phys. Rev. B* **34**, 5977 (1986).
- [180] E. J. O'Halloran, C. A. Broderick, D. S. P. Tanner, S. Schulz, and E. P. O'Reilly, "Comparison of first principles and semi-empirical models of the structural and electronic properties of $\text{Ge}_{1-x}\text{Sn}_x$ alloys," *Optical and Quantum Electronics* **51**, 314 (2019).
- [181] S. Q. Wang and H. Q. Ye, "Plane-wave pseudopotential study on mechanical and electronic properties for IV and III-V crystalline phases with zinc-blende structure," *Phys. Rev. B* **66**, 235111 (2002).
- [182] N. Hammou, A. Zaoui, and M. Ferhat, "Revisiting stabilities of cubic zincblende IV-IV materials from density functional theory," *Phys. Status Solidi C* **14**, 1700226 (2017).
- [183] C. A. Broderick and E. P. O'Reilly, "Tin-induced band mixing in $\text{Ge}_{1-x}\text{Sn}_x$ alloys: quantifying the continuous nature of the indirect- to direct-gap transition," in preparation (2019).

- [184] C. A. Broderick, M. Usman, S. J. Sweeney, and E. P. O'Reilly, "Band engineering in dilute nitride and bismide semiconductor lasers," *Semiconductor Science and Technology* **27**, 094011 (2019).
- [185] S. Al-Kabi, S. A. Ghetmiri, J. Margetis, T. Pham, Y. Zhou, W. Dou, B. Collier, R. Quinde, W. Du, A. Mosleh, et al., "An optically pumped $2.5\mu\text{m}$ GeSn laser on Si operating at 110K," *Appl. Phys. Lett.* **109**, 171105 (2016).
- [186] V. Reboud, A. Gassenq, N. Pauc, J. Aubin, L. Milord, Q. M. Thai, M. Bertrand, K. Guillo, D. Rouchon, J. Rothman, et al., "Optically pumped GeSn micro-disks with 16% Sn lasing at $3.1\mu\text{m}$ up to 180 K," *Appl. Phys. Lett.* **111**, 092101 (2017).
- [187] J. Margetis, S. Al-Kabi, W. Du, Y. Zhou, T. Pham, P. Grant, S. Ghetmin, B. Li, J. Liu, G. Sun, et al., "Si-based GeSn lasers with wavelength coverage of $2 - 3\mu\text{m}$ and operating temperatures up to 180 K," *ACS Photonics* **5**, 827 (2017).
- [188] J. Margetis, Y. Zhou, W. Dou, P. C. Grant, B. Alharthi, et al., "All group-IV SiGeSn/GeSn/SiGeSn QW laser on Si operating up to 90 K," *Appl. Phys. Lett.* **113**, 221104 (2018).
- [189] Y. Zhou, W. Dou, S. Ojo, H. Tran, S. A. Ghetmiri, J. Liu, G. Sun, R. Soref, J. Margetis, J. Tolle, et al., "Optically pumped GeSn lasers operating at 270 K with broad waveguide structures on Si," *ACS Photonics* **6**, 1434 (2019).